Synthetic aperture imaging of B-X-O mode conversion

Simon Freethy

PhD Thesis

York Plasma Institute

The University of York

March 2012

Abstract

The conversion of thermally-born electrostatic waves in tokamak plasmas has the potential to be a powerful diagnostic for tokamak edge physics. Analytic theory and full wave modelling both conclude that analysis of emission in the microwave region carries with it information on the magnetic field in spatially localised areas which depend on density and frequency. Knowing these quantities and the 3D (2D + frequency) microwave emission pattern, it is in theory possible to calculate the current density which is vital to the understanding of the plasma pedestal. Motivated by a pilot experiment carried out on the Mega Ampere Spherical Tokamak (MAST), a novel microwave imaging device has been developed to obtain the first images of mode conversion in a Tokamak and to prove the principle of the synthetic aperture imaging technique on Tokamak devices. Here the design and calibration of the Synthetic Aperture Microwave Imaging (SAMI) radiometer is described, as well as the presentation and comparison of some of the first images of mode conversion with full wave simulations.

Contents

Acknowledgements

First and foremost I would like to thank my two excellent supervisors, Dr. Vladimir Shevchenko and Dr. Roddy Vann. Their endless advice, expertise and support have been of great value. I have been extremely lucky to have them as my mentors and I have thoroughly enjoyed every part of working with them.

I would also like to thank the MAST team for their help and support in making this project a success, and the Culham student community for offering many insightful conversations. In particular I would like to thank Dr. Oliver Ford for many stimulating conversations about this work, and Suzannah Wake for her patient proof reading and inquisitive questioning.

This thesis was funded in part by the Engineering and Physical Sciences Research Council (EPSRC) and the Culham Centre for Fusion Energy (CCFE).

The diagnostic development was funded under EPSRC grant EP/H016732/1

Author's declaration

Some of the original work presented in this thesis has been published in the following journal articles:

Optimisation of wide field interferometric arrays via simulated annealing of a beam efficiency function, S Freethy, V F Shevchenko, R G L Vann, *IEEE transactions on antennas and propagation*, (SUBMITTED)

Two Dimensional Studies of Electron Bernstein Wave emission in MAST, V F Shevchenko, S Freethy, R G L Vann, *Fusion Science and Technology*, **59**, 4, 2011

Bottling a star using ARMs AXIBus in an FPGA, *Xcellence in scientific applications*, **76**, 2011

2D EBW emission studies on MAST, V F Shevchenko et al, *proceedings of 16th EC joint workshop*

Recent progress with the MAST synthetic aperture imaging radiometer, S Freethy V F Shevchenko, R G L Vann, *proceedings of 38th European Physical Society Conference on Plasma Physics*

L-H transition studies on MAST, H Myer et al, *Nuclear Fusion*, **51**, 2011

Overview of physics results from MAST, B Lloyd et al, *Nuclear Fusion*, **51**, 094013, 2011

All work presented in this thesis as original is so to the best knowledge of the author. References and acknowledgements to other researchers have been given as appropriate.

Chapter 1

Introduction

1.1 Magnetic confinement fusion

The process of fusing nuclei of deuterium and tritium has long been described as a potential future energy source due to its high abundance of fuel, short lived radioactivity and zero carbon emissions. There are many approaches to achieving the controlled burn of this fusion fuel which may, in future, provide the basis for a commercially viable power plant. The front runners can be broadly defined in two categories, inertial confinement and magnetic confinement. The magnetic confinement category has, over the past few decades, narrowed to a handful of potential candidate machines, of which the tokamak holds the records for the most amount of controlled fusion power produced and the most amount of power out compared to heating power in. The European tokamak, JET (Joint European Torus), produced 16 MW of fusion power and 0.7 times as much power out than heating power in.

The next step in tokamak research is the ITER project. ITER is currently under construction in Caderache, France and is a multi-national venture. Roughly twice the linear dimensions of JET, the present largest tokamak, it will need to cope with a hugely increased heat-load on its plasma facing components, with the divertor region reaching nearly 10 MWm^{-2} and transient events such as edge localised modes (ELMs) pushing this figure over 20 MWm^{-2} [1]. There is significant uncertainty on the lifetime of these plasma fac-

ing components as these heat-loads are capable of producing erosion and melting of the materials.

A broad approach to this problem is necessary if fusion is to succeed. Improvements in the materials used as plasma facing components [2, 3], new designs for plasma wall interaction control [4, 5] and active control of transient events [6, 7] are just some of the approaches to this problem. This thesis focusses on a complimentary approach in trying to understand the driving factors of the transient ELM events. Here I present the development of a diagnostic which holds potential for diagnosing important quantities in the plasma edge which are thought to drive the ELM instability. Anisotropic emission in the microwave range is strongly related to the relevant quantities, localised to the edge region. I and the small team I worked with developed a microwave imaging diagnostic for the MAST tokamak to obtain the first ever images of this anisotropic emission and opened a new path for understanding the ELM.

1.2 The Mega Ampère Spherical Tokamak (MAST)

The Mega Ampere Spherical Tokamak (MAST) (Figure 1.1) differs from conventional tokamaks in one important way. The aspect ratio, i.e. the ratio of the major radius to the minor radius is much lower than would be normal for a conventional tokamak, giving the plasma a distinctly spherical appearance. The reason for this shape is rooted in the machine's ability to operate at a higher ratio of plasma pressure to magnetic field pressure or β. The plasma β is a good indicator for the cost efficiency of a future power plant beacuase it encompasses how much plasma pressure one can acheive for a given applied magnetic field. The β limit, derived by Wesson and Sykes [8] has long been known to depend on the tokamak's aspect ratio with a lower ratio giveing a higher β limit. Other important machine parameters for MAST are given in table 1.1.

The plasma β also affects the subject of this thesis more directly. In a conventional tokamak, electromagnetic waves of a given frequency in the 10 - 100 GHz region are born by the thermal motion of electrons about the magnetic field. The frequency of this emission

parameter	value
magnetic field on axis	0.5 T
core temperature	1.5 keV
core density	$5 \cdot 10^{19}\mathrm{m}^{-3}$
plasma current	1.3 kA
pulse length	0.5 s
aspect ratio	1.3

Table 1.1: Typical MAST machine parameters

depends on the strength of the magnetic field and since the magnetic field varies with radial position, this frequency is a proxy for radius. Normally the absorption and re-emission of this radiation near the place of its birth is so high that the radiation comes into thermal equilibrium with its surroundings and can be used as a temperature diagnostic. For a given frequency, however, there exists a critical density of electrons above which these electromagnetic waves cannot propagate. The high β nature of a spherical tokamak means that the first few harmonics of this cyclotron emission is underneath the critical cut-off frequency and thus these waves cannot propagate.

However, there are also thermally born electrostatic waves known as Electron Bernstein Waves (EBWs), which in this case are able to convert to electromagnetic waves at the critical cut-off frequency and escape the plasma. This conversion from one wave mode to another combined with the strong refraction of the EBWs in the bulk plasma make Bernstein waves difficult to use as a temperature diagnostic on a tokamak. However, the mode conversion mechanism is primarily sensitive to the magnetic field in the mode conversion region, which is a key parameter of interest to those studying the Edge Localised Mode described in section 1.3.

1.3 H-mode and ELMs

The high confinement or H-mode of operation is broadly defined by the presence of a strong barrier to particle and energy transport at the edge of a tokamak plasma. The presence of this edge transport barrier enables a tokamak to operate with a much increased

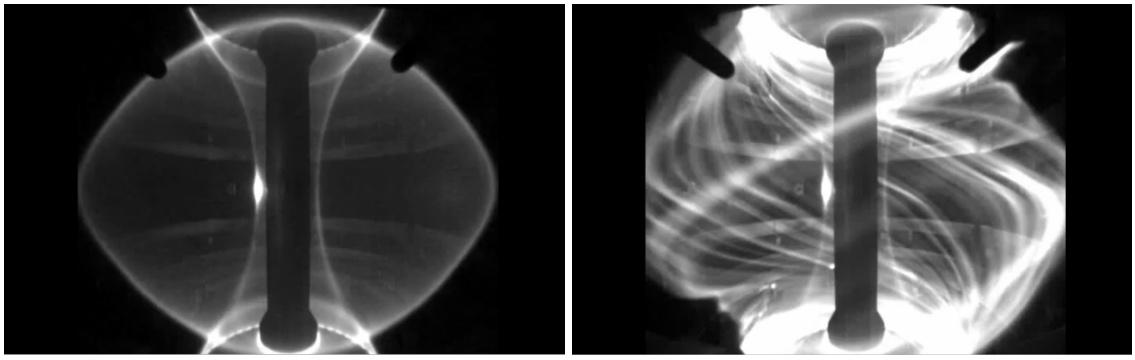

Figure 1.1: **Left**: An optical D_α image of a typical MAST H-mode. **Right**: An optical image during a type 1 ELM event.

central pressure for a given magnetic field, which is an advantage when one wishes to design a smaller cheaper fusion device [9].

This mode of operation usually brings with it an instability which is localised to the edge, typically the last 2-3 cm, of a tokamak plasma. The ELMs come in three types, but of these, the first type is the most damaging and therefore most important. Type 1 giant ELMs can cause the sudden loss of up to 10-15% of the plasma stored energy and brings with it a sharply increased heat load to the plasma facing components inside the vessel [10, 11] and is widely considered an unacceptable risk to the ITER divertor region. Type 3 ELMs are observed near the H-mode power threshold and produce small energy dumps (1-3% of the stored energy) [12]. Type 2 ELMs are rarely seen as they require highly shaped plasmas and access to a particular region of stability. A type 1 ELM can be seen on the right hand side of Figure 1.1. Understanding these instabilities is important for predicting their size in future fusion machines and may highlight ways of minimising their damaging effects.

The presently accepted model for the type 1 ELM relies on the coupling between two distinct instabilities. The first is driven by a pressure gradient and the second is driven by a current density. These two instabilities are able to couple together via a pressure gradient driven current density known as the bootstrap current. This model is known as the coupled peeling-ballooning mode.

The measurement of the edge current density is difficult due mostly to its small radial extent, rapid evolution in time and extreme thermal and electrical conditions of the plasma which supports it. There is some limited experimental knowledge of the edge current density from Lithium ion beam experiments [13], which shows the current density largely in agreement with the predicted bootstrap current. However evidence gathered from a technique which utilises the anisotropic nature of Bernstein wave mode conversion seems to show a strong disagreement with the bootstrap current, instead proposing a double current layer, where two current sheets exist in opposite directions [14]. We will explain the latter technique in more detail in section 1.4 because of its direct relevance to the work of this thesis.

1.4 The spinning mirror experiment

The idea behind the spinning mirror experiment relies on the fact that the conversion of energy from thermally born electrostatic waves, known as electron Bernstein (B) waves, to electomagnetic waves polarised parallel to the field, Ordinary (O) mode waves, is a strongly anisotropic process. This anisotropy, as described in detail in section 2.3, is strongly related to the local magnetic field, magnetic shear and density gradient at a location uniquely defined by the plasma density profile. It is possible, from measurement of this anisotropic emission, to measure the magnetic field vector, magnetic shear and density gradient. Then using a diagnostic which measures the density profile, such as laser scattering, we can localise the measurements in space. When all this is combined it is possible, among other things, to measure current density by taking the curl of the measured magnetic field vector via Ampère's law.

The spinning mirror experiment described here was, to a large extent, the motivation for the work presented in this thesis. It was proposed that the anisotropic properties of the mode conversion of electrostatic EBWs may be a candidate for high radial resolution measurements of the edge current profile [15]. As a result, the idea of an oscillating mirror arrangement was conceived to mechanically scan the beam of an antenna over the plasma

surface. This would sample a mode conversion window as a function of angle at multiple frequencies and one would then be able to relate these traces to the local magnetic field as a function of radius, via the strong dependence of the emission anisotropy on the local magnetic field. Figure 1.2 shows the expected path of the centre of the antenna beam and the expected power trace as a function of time.

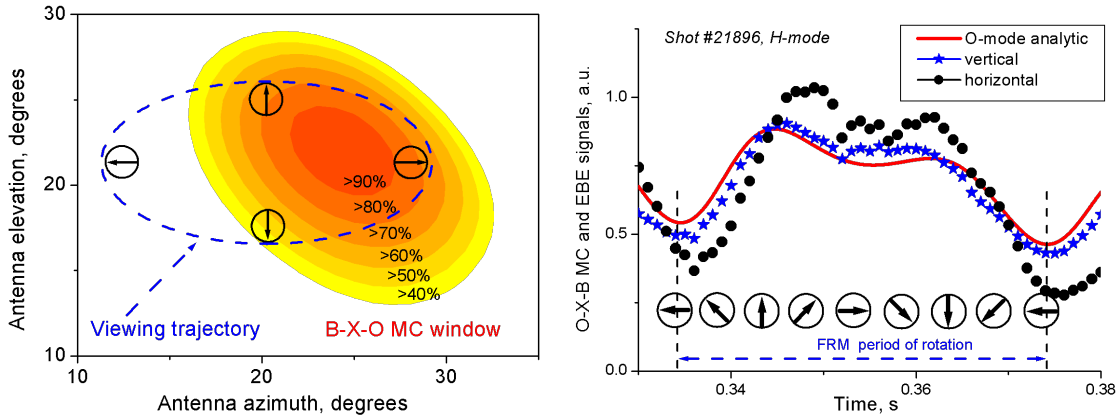

Figure 1.2: **Left**: This trace shows an example of a mode conversion window in angular coordinates relative to an external observer. The elliptical trajectory signifies the centre of the antenna beam as the mirror rotates. **Right**: The expected and measured traces from the spinning mirror experiment. The double peaked structure indicates that the mirror trajectory encloses the maximum of the ellipse.

The measurements confirmed that there is strongly anisotropic emission of an approximately elliptical shape, the maximum of which was enclosed in the antenna beam trajectory. The results also showed that the centre of this mode conversion ellipse moved as a function of frequency and therefore the magnetic field varied as a function of radius. Further the spinning mirror measurements revealed unexpected behaviour in the field line pitch as shown in the right hand side of Figure 1.3. The pitch was calculated to have a peaked structure implying that there exists two current sheets carrying opposite currents.

There are, however, limitations in the diagnostic's temporal resolution, which are due to the fact that the mirror has a stringent upper limit on its rotation speed. This limit means that diagnosing the evolution of current between ELMs (typically approximately 6 - 12 milliseconds on MAST) is not feasible.

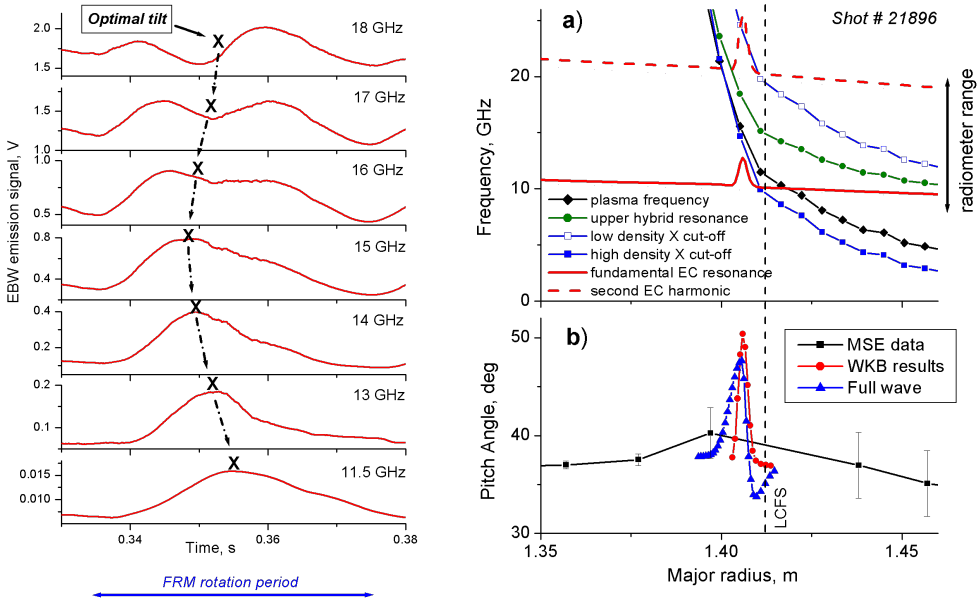

Figure 1.3: **Left**: The radiometer traces during one period of a mirror scan for different frequencies. It appears as though the centre of the mode conversion window changes position as a function of radius. **Right**: The best fit of magnetic field pitch angle for the traces on the left. The field pitch has a peaked structure implying a double current layer. The fitted data is consistent with the Motional Stark Effect (MSE) diagnostic.

Building an array of antennas which could electronically scan a synthesised beam across the plasma surface would enhance the temporal resolution and potentially provide more information about the dynamics of the mode conversion ellipse. It would be able to produce two dimensional images of the mode conversion process, something which has not been achieved in tokamak plasmas before.

1.5 Outline and scope of the thesis

This thesis concerns the development, construction, commissioning, calibration and first data of a Synthetic Aperture Microwave Imaging (SAMI) radiometer which is designed to obtain the first ever images of slow eXtraordinary - Ordinary (X-O) mode conversion in tokamak plasmas. These images are explored and compared to both analytic and full wave

calculations of the process.

The thesis begins with a description of basic high frequency wave physics in cold plasmas and a description of the warm plasma Bernstein mode. It then describes the conversion of Bernstein waves to slow extraordinary waves to ordinary waves (B - sX - O) waves and Bernstein waves to extraordinary waves (B - X) and highlights the important characteristics of these mode conversion processes.

This is followed by a description of phased array type antenna arrays and their extension to the aperture synthesis technique, including the effect of polarisation on the observations.

A full diagnostic description is then presented including the antenna design, electronic layout and components, and the Field Programmable Gate Array (FPGA) controlled data acquisition system. As well as the antenna design and a description of the optimisation of the antenna array.

Next, the details of the commissioning stage and data verification and calibration are presented together with the first data from the pilot experiment. Then the first images of these mode conversion processes is presented and a comparison between the observations and a numerical full wave simulation. Finally, there is an analysis and discussion of possible sources of error.

The work presented here is the result of a small team of four and is largely a joint project with most stages of design and verification being heavily influenced by all parties involved. I played a particularly strong role in the array configuration design, the calibration and validation experiments, the signal processing and analysis and the comparison of the data with the numerical simulations.

Chapter 2

Emission, propagation and mode conversion of Electron Bernstein Waves

2.1 Electromagnetic waves in plasmas

The topic of waves in plasmas is vast. There are many classifications of waves depending on frequency range, length scale, magnetic field and plasma temperature [16]. We will only be interested in the electromagnetic modes found in the cold plasma theory and the electrostatic Bernstein mode found from plasma kinetic theory. First I present a brief overview of two special cases of electromagnetic wave propagation in a cold plasma, leading to what are generally referred to as the right and left handed modes for parallel propagation and the Ordinary and Extraordinary modes for perpendicular propagation. We then describe the more general case of oblique propagation in this regime. For a more complete derivation of the modes described below, we refer the reader to one of the excellent textbooks on the subject [16, 17, 18, 19]

Consider a quasi-neutral ionised gas, where the thermal motions of the particles are assumed to be negligible. Further, let us consider the case where the frequency of the waves of interest is much faster than the temporal variation of the bulk plasma parameters, and that the wavelengths are much shorter than their spatial variation. In this approximation we may consider solutions to Maxwell's wave equation (2.1) of the form $\exp[i(\boldsymbol{k}\cdot\boldsymbol{r}-\omega t)]$

[16].

$$\nabla \times \boldsymbol{B} = \frac{4\pi \boldsymbol{j}}{c} + \frac{1}{c}\frac{\partial \boldsymbol{E}}{\partial t} = \frac{1}{c}\frac{\partial \boldsymbol{D}}{\partial t} \tag{2.1}$$

We may then adopt a model where all the particles in the plasma follow the same motion locally; thus the collective motion locally is described by the motion of a single particle at that location, a so called single particle description, to derive the dielectric tensor, $\boldsymbol{D}$. From the condition on (2.1) to have non trivial solutions we will derive the cold plasma dispersion relation. First, it is useful to define the dimensionless electron cyclotron and plasma frequencies as follows:

$$X = \frac{\omega_p^2}{\omega^2}, \qquad Y = \frac{\omega_c}{\omega} \tag{2.2}$$

where ω_c is the electron cyclotron frequency defined as $\omega_c = eB/m$, ω_p is the plasma frequency defined as $\omega_p^2 = n_{\mathrm{e}} e^2/m_e \epsilon_0$ and ω is the frequency of the wave of interest.

We begin by writing Ohm's law:

$$\boldsymbol{j} = -e n_{\mathrm{e}} \boldsymbol{v} = \boldsymbol{\sigma} \cdot \boldsymbol{E} \tag{2.3}$$

where $\boldsymbol{j}$ current density, n_{e} is the electron number density, $\boldsymbol{v}$ is the the electron velocity, $\boldsymbol{E}$ the electric field and $\boldsymbol{\sigma}$ is the conductivity tensor. We may then use the Lorentz force law for the electrons (2.4) to obtain $\boldsymbol{v}$.

$$m\frac{d\boldsymbol{v}}{dt} = e\left(\boldsymbol{v} + \boldsymbol{E} \times \boldsymbol{B}\right) \tag{2.4}$$

Assuming that $\boldsymbol{E}$, $\boldsymbol{B}$ and $\boldsymbol{v}$ can be made up of a uniform static background plus a small perturbation, keeping only terms up to second order in these perturbations, and considering a static uniform magnetic field along the z axis, i.e. $\boldsymbol{B} = B\hat{\boldsymbol{z}}$, we obtain:

$$\boldsymbol{\sigma} = \frac{-ine^2}{\omega m_e}\frac{1}{1-Y^2}\begin{pmatrix} 1 & iY & 0 \\ iY & 1 & 0 \\ 0 & 0 & 1-Y \end{pmatrix} \tag{2.5}$$

From (2.1), considering small harmonic perturbations in all quantities and retaining only terms linear in those perturbations. It is useful at this stage to define the dimensionless wavevector as $\boldsymbol{N} = c\boldsymbol{k}/\omega$. The modulus of this quantity is the refractive index and describes the ratio of phase speed of light in the vaccum c, to the phase speed at the location of interest. It is also useful to define the projections of this vector with respect to the magnetic field, $N_\parallel = N\cos\theta$ and $N_\perp = N\sin\theta$. The wave equation then reduces to:

$$\boldsymbol{N} \times (\boldsymbol{N} \times \boldsymbol{E}) + \boldsymbol{\epsilon} \cdot \boldsymbol{E} = 0 \tag{2.6}$$

where $\boldsymbol{\epsilon} = (\boldsymbol{I} + \boldsymbol{\sigma}\frac{i}{\omega\epsilon_0})$ and $\boldsymbol{I}$ is the identity matrix.

Explicitly

$$\boldsymbol{\epsilon} = \begin{pmatrix} \epsilon_\perp & -i\epsilon_{xy} & 0 \\ i\epsilon_{xy} & \epsilon_\perp & 0 \\ 0 & 0 & \epsilon_\parallel \end{pmatrix} \tag{2.7}$$

where: $\epsilon_\parallel = 1 - X, \qquad \epsilon_\perp = 1 - \frac{X}{1-Y^2}, \qquad \epsilon_{xy} = \frac{XY}{1-Y^2}$

If we use θ to denote the angle between the magnetic field and the wavevector[1], $\boldsymbol{k}$ and assume, without loss of generality, that $\boldsymbol{k}$ lies in the (x, z) plane, equation (2.6) becomes

$$\boldsymbol{\Lambda} \cdot \boldsymbol{E} \equiv \begin{bmatrix} \epsilon_\perp - N^2\cos\theta & -i\epsilon_{xy} & N^2\cos\theta\sin\theta \\ i\epsilon_{xy} & \epsilon_\perp - N^2 & 0 \\ N^2\cos\theta\sin\theta & 0 & \epsilon_\parallel - N^2\sin^2\theta \end{bmatrix} \begin{pmatrix} E_x \\ E_y \\ E_z \end{pmatrix} = 0 \tag{2.8}$$

Equation (2.8) has non-trivial solutions if and only if:

$$\det[\boldsymbol{\Lambda}] = 0 \tag{2.9}$$

[1] and therefore the dimensionless wavevector $\boldsymbol{N}$

Solving (2.9) for N^2, we obtain a bi-quadratic equation of the form $AN^4 - BN^2 + C = 0$, where

$$\begin{aligned} A &= \epsilon_\perp \sin^2\theta + \epsilon_\parallel \cos^2\theta \\ B &= (\epsilon_\perp^2 + \epsilon_{xy}^2)\sin^2\theta + \epsilon_\perp\epsilon_\parallel(1+\cos^2\theta) \\ C &= \epsilon_\parallel(\epsilon_\perp^2 + \epsilon_{xy}^2) \end{aligned} \tag{2.10}$$

with solutions for the square of the refractive index N:

$$N^2 = \frac{B \pm D}{2A} \tag{2.11}$$

where: $D^2 = (\epsilon_\perp^2 + \epsilon_{xy}^2 - \epsilon_\parallel\epsilon_\perp)^2 \sin^4\theta + 4\epsilon_\parallel^2\epsilon_{xy}^2\cos^2\theta$

Note that there are, in general, two solutions for N^2, which correspond to two modes of propagation with differing refractive indices and therefore phase speeds. These two solutions are often referred to as the fast and the slow mode for this reason. These modes change polarisation with angle, and when propagating directly parallel to $\boldsymbol{B}$ are the traditional Left circularly polarised (L) mode and Right circularly polarised (R) mode, and when propagating directly perpendicular to $\boldsymbol{B}$ are the eXtraordinary (X) mode and Ordinary (O) mode. It is worth noting that obliquely propagating modes are also sometimes referred to as X mode and O mode.

2.1.1 Propagation parallel to the magnetic field

The two modes which propagate parallel to $\boldsymbol{B}$ have different phase velocities due to their interaction with the gyrorotation of the electrons. Setting $\theta = 0$ in (2.11) we see that:

$$N_\parallel^2 = 1 - \frac{X}{1 \pm Y} \tag{2.12}$$

Since $\boldsymbol{N} = c\boldsymbol{k}/\omega$, when $\boldsymbol{N}^2 \to \infty$ this implies that $\lambda \to 0$. This corresponds to system resonance where both the phase velocity and wavelength approach zero. At this point

the wave energy becomes absorbed by the plasma. Alternatively, when $\boldsymbol{N^2} \rightarrow 0$ then $\lambda \rightarrow \infty$. This corresponds to a wave cut-off and the wave energy is reflected at this point. Interestingly, if $N^2 < 0$, then 2.1 has solutions with real exponents corresponding to damped solutions. These regions will not support electromagnetic wave propagation, but will allow tunnelling between regions which are not evanescent, provided the conditions are favourable.

We see from (2.12) that waves propagating parallel to $\boldsymbol{B}$ have cut-offs when $\omega = \omega_{1,2} = [(\omega_c/2)^2 + \omega_p^2]^{1/2} \pm \omega_c/2$, but only one of the modes has a resonance at $\omega = \omega_c$. This is because electrons are accelerated by a co-rotating wavefield, but there is no net effect of the wave on electrons if the wavefield is counter-rotating [17].

If we turn off the magnetic field by letting $Y \rightarrow 0$, we can see that the resonances disappear and we are left with one cut-off at the plasma frequency ω_p. This is known as the plasma density cut-off.

2.1.2 Propagation perpendicular to the magnetic field

Setting $\theta = \pi/2$ in equation (2.11) and using the definition for $\boldsymbol{N}$ we may write the two perpendicular dispersion relations in the following useful forms:

$$N_\perp^2 = 1 - X \tag{2.13}$$

$$c^2 k_\perp^2 = \frac{(\omega^2 - \omega_1^2)(\omega^2 - \omega_2^2)}{\omega^2 - \omega_{\mathrm{UH}}^2} \tag{2.14}$$

$$\text{where} \quad \omega_{\mathrm{UH}} = (\omega_c^2 + \omega_p^2)^{1/2}$$

The relation in (2.13) is exactly the same dispersion relation which we derived by turning off the magnetic field in Section 2.1.1. This is known as the O mode for exactly this reason, it behaves as if there were no magnetic field at all. The O mode is linearly polarised with the electric field vector, $\boldsymbol{E}$ aligned parallel to $\boldsymbol{B}$. In this arrangement $\boldsymbol{B}$, to first order, has no effect on the motions of the electrons, and thus its dispersion relation is identical to that of an electromagnetic wave propagating in a plasma with no $\boldsymbol{B}$ field at all.

The dispersion relation in (2.14) is that of the X mode. The X mode however is not linearly polarised. As pointed out in [17], this mode is elliptically polarised with a component of $\boldsymbol{E}$ perpendicular to $\boldsymbol{B}$ and a component parallel to $\boldsymbol{k}$, thus making this mode partly longitudinal and partly transverse. The X mode has two cut-off frequencies which occur at the previously derived $\omega_{1,2}$ cut-offs. The upper hybrid frequency ω_{UH}, where the X mode has its resonance, corresponds to a natural plasma oscillation in which the electrons have elliptical orbits which are part plasma oscillation and part cyclotron oscillation.

2.1.3 Propagation at arbitrary angle

The general dispersion relation for waves propagating at some arbitrary angle to the magnetic field is known as the Appleton - Hartree relation [16]. We may derive the relation by first writing the solution to (2.9) as

$$N^2 = 1 - \frac{2\left(A - B + C\right)}{2A - B \pm \left(B^2 - 4AC\right)^{1/2}} \tag{2.15}$$

Substituting A, B and C from (2.11), we may write the refractive index as:

$$\begin{gathered} N^2 = N_\perp^2 + N_\parallel^2 = 1 - \frac{2X(1-X)}{2(1-X) - Y^2\sin^2\theta \pm \gamma} \\ \text{where} \quad \gamma = [Y^4\sin^4\theta + 4(1-X)^2Y^2\cos^2\theta]^{1/2} \end{gathered} \tag{2.16}$$

In order to evaluate the polarisation of an obliquely propagating mode we evaluate the quantity E_y/E_x which using expression (2.8) can be shown to be [19]:

$$\frac{E_y}{E_x} = -i\frac{2Y\left(1-X\right)\cos\theta}{Y^2\sin^2\theta \pm \gamma} \tag{2.17}$$

2.2 The Bernstein modes

A spherical tokamak's high beta nature means that typically the first few cyclotron resonances are covered by the plasma density cut-off for the O mode and the low density cut-off for the X mode. This means that electromagnetic waves in the bulk plasma are evanescent and cannot propagate. There are, however, thermally born electrostatic waves which exist inside the plasma in this frequency range with no density limit and are known as electron Bernstein waves after Ira Bernstein's seminal paper in 1958 [**?**].

To describe the Bernstein waves, first we must relax the assumption made in the previous chapters of zero plasma temperature and allow the electrons to posses a finite Larmor radius $\rho = mv_{\mathrm{th}}/(eB)$. The key fact about assuming a finite Larmor radius is that it allows us to consider charge separation perpendicular to the magnetic field. This ability for the creation of charge separation allows the electrons to participate in any electric field disturbance perpendicular to $\boldsymbol{B}$.

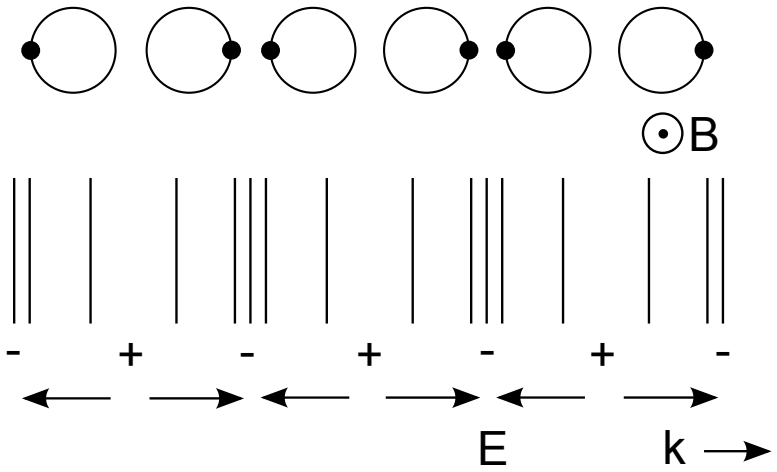

Figure 2.1: The electons orbiting around the magnetic field may perform coherent oscillations driven by the cross field charge separation allowed when considering a finite orbit radius. An electrostatic longitudinal wave can be set up which is sustained by the electron motion.

Let's assume that we have an electric field perturbation at the frequency of the local cyclotron frequency. The electrons would collectively feel a force on resonance with their

natural oscillation frequency. Further, they may also influence neighbouring electrons as they repel the electrons nearby through the field generated by the accumulation of charge from being moved in a particular direction. In this way we may set up a longitudinal electrostatic wave supported by the gyrorotation of the electrons.

Another way to think of the Bernstein waves, as pointed out by Volpe [20], is to think of Langmuir waves in an unmagnetised plasma. As we then slowly increase the strength of the magnetic field in this plasma, the orbits of the electrons become more elliptical, until finally as the magnetic field dominates, the orbits of the electrons are circular.

2.3 Mode conversion

The electron Bernstein waves described in the previous chapter are electrostatic and thus require the motion of the electrons for them to continue to propagate. They may, however, convert to electromagnetic modes at the upper hybrid resonance, where the phase speed and wavelength of the X mode become comparable to that of the B mode. The process of mode conversion of Bernstein waves allows them to be detected outside the plasma. The mode conversion process itself contains a great deal of information about plasma parameters near the location of the conversion and observations of the emission pattern may be used as a diagnostic for these parameters.

This mode conversion process is more easily understood by first considering the reciprocal process of an electromagnetic wave approaching from outside the tokamak and propagating inwards and then invoking the reciprocity theorem [21] to see that the emission process is the same in reverse order.

Considering the dispersion relation in 2.17 as we increase in density, keeping the magnetic field approximately constant, we have several cut-offs and resonances, the order of which are important to the problem we are about to consider. First there is the low density cut-off for the X mode ω_1, next the upper hybrid resonance ω_{UHR} for the X mode, followed by the density cut-off for the O mode ω_{p} and finally the high density cut-off for the X mode ω_2.

These points can be seen in Figure 2.2 (b). For clarity here we will refer to the X mode at densities lower than the low density cut-off as the fast X (fX) mode and those which exist between the upper hybrid resonance and the high density cut-off as the slow X (sX) mode. In general terms there are two types of mode conversion process which may occur: the conversion of the fX mode into the Bernstein mode and the conversion of the O mode into the Bernstein mode via the sX mode.

The first of these processes occurs when the upper hybrid resonance is sufficiently close to the low density cut-off that the X mode may tunnel to the resonance layer, where it is converted into a B mode. The second occurs when the O mode is injected in such a way, that after refraction it arrives at the plasma density cut-off with the same phase speed and polarisation as the X mode. It can then propagate to the high density cut-off and then back to the upper hybrid resonance where again it can convert into a B mode wave. A pleasing visualisation of the second process can be found in Kohn at al [22, 23]. We will now look at each of these processes in more detail.

2.3.1 O - sX conversion

If we examine again the Appleton - Hartree relation (2.17), we can see that the two branches of the dispersion relation are identical if $\gamma = 0$. This happens if, at the same time both $\theta = 0$ and $X = 1$, which corresponds to $\boldsymbol{k}$ being directly parallel to $\boldsymbol{B}$ at the plasma cut-off layer. This allows both branches of the dispersion relation to form one continuous O-X curve: see Figure 2.2 (a). At angles slightly greater than zero at $X = 1$, the branches do not connect as in Figure 2.2 (b).

If we consider a plane stratified medium in which the density gradient is in the x direction and the magnetic field is in the z direction, as in Figure 2.3, there is an optimal launch angle which will cause the ray to refract in such a way that $\boldsymbol{k}$ is parallel to $\boldsymbol{B}$ at $X = 1$. Further, in this setup we may use Snell's law to see that the parallel component of $\boldsymbol{N}$ remains constant for an individual ray since the only variation in $\boldsymbol{N}$ is perpendicular to $\boldsymbol{B}$. If we also note that $\theta = \arctan(N_\perp/N_\parallel)$, (2.17) may be rearranged to give us $N_\perp$ in terms

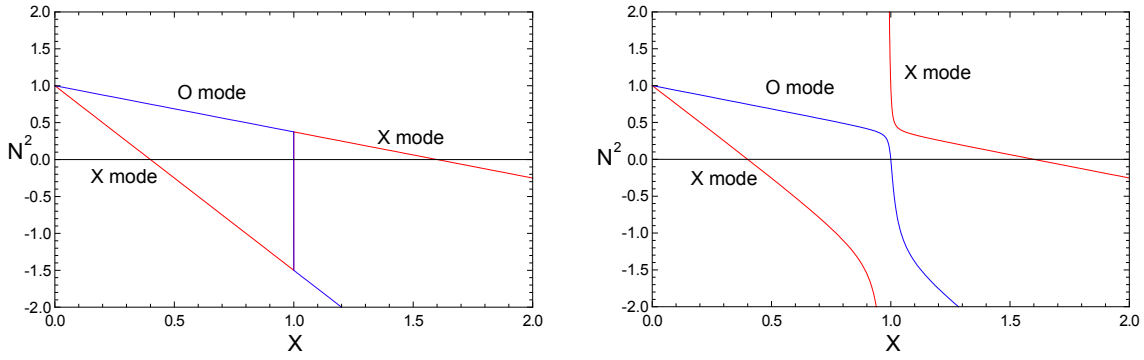

(a) (b)

Figure 2.2: The dispersion relation for a cold plasma wave vs. normalised electron density. The X mode contains two cut-offs at $\omega_{1,2}$ and a resonance at ω_{UH}. The O mode has one cut-off at the plasma frequency. When $\theta = 0$ at the $X = 1$ layer the O and X mode branches of the dispersion relation form one O-X curve. This can be seen by examining the Appleton Hartree relation at (a) $\theta = 0$ and (b) $\theta > 0$

of $N_{\|}$, X (dimensionless density) and Y (dimensionless magnetic field), this expression is lengthy and so is not given explicitly here. Snell's law states:

$$\cos\alpha = N_{\|} = const. \tag{2.18}$$

where α is the angle of incidence, i.e. the angle between $\boldsymbol{k}$ and $\boldsymbol{B}$ when the ray first enters the plasma. We may now calculate the optimal $N_{\|}$ since it will be the same at $X = 1$ and $X = 0$ (no plasma). Evaluating expression (2.17) with $\theta = 0$ and $X = 1$ gives us [24, 25]:

$$N_{\|,opt} = \cos\alpha_c = \sqrt{\frac{Y}{1+Y}}\Bigg|_{X=1} \tag{2.19}$$

The square of the perpendicular refractive index for different values of $N_{\|}$ are plotted in Figure 2.4 along with the polarisation fraction for the same ray paths. For the optimal launch angle we see that the O mode turning point is coincident with the plasma density cut-off as expected and we can also see that the polarisation at the cut-off is exactly circular, matching the mode polarisation for parallel propagation. The dotted and dashed lines show slightly non optimal values for the initial launch angle. These two rays encounter a

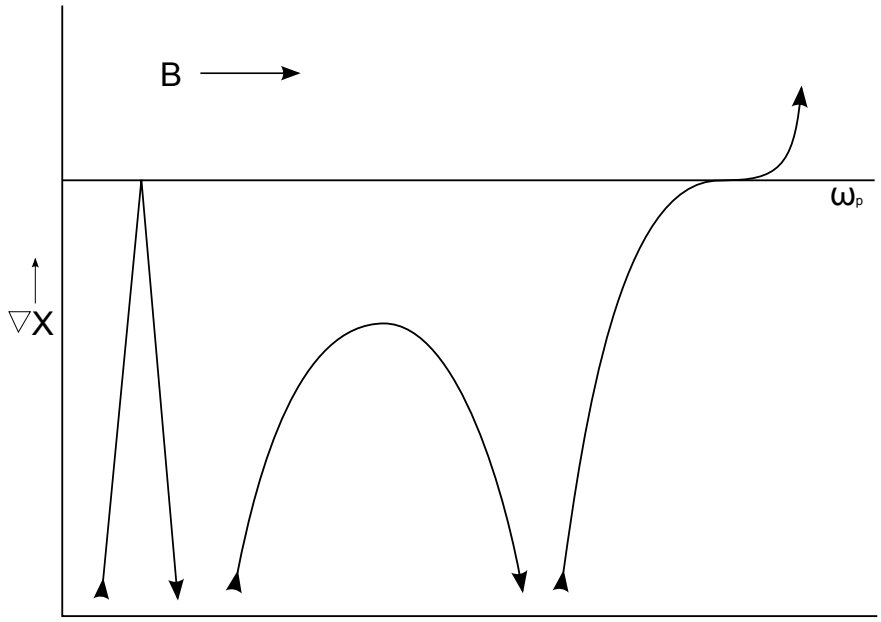

Figure 2.3: The plane stratified geometry under consideration for the O-X-B mode conversion, increasing density up the page. From left to right: A ray with $N_{\|} < N_{\|,opt}$, A ray with $N_{\|} > N_{\|,opt}$ and a ray with $N_{\|} = N_{\|,opt}$. A ray with the correct angle of incidence $\cos\alpha = N_{\|,opt}$ may get completely mode converted to an X mode propagating past the density cutoff.

region of evanescence before continuing along the X mode branch, implying that non optimal rays may also mode convert at some reduced efficiency, which gets lower and lower the further the launch angle is from the optimal value.

If we consider solutions to (2.6) of the form $E\ e^{i\int \boldsymbol{k}\cdot d\boldsymbol{x}}$ and use Snell's law to determine that the x component of the refractive index is the only one which can go imaginary, we can define a transmissivity $\mathfrak{T}$ as:

$$\mathfrak{T} = \exp\left\{-2\frac{\omega}{c}\mathfrak{Im}\left|\int_{z_1}^{z_2} N_x\, dx\right|\right\} \tag{2.20}$$

An analytic form for this integral has been studied by different authors who, by virtue of the fact that they follow different methods, arrive at slightly different answers [24, 25, 26]. The formula derived by Mjølhus [25] agrees best with full wave numerical calculation

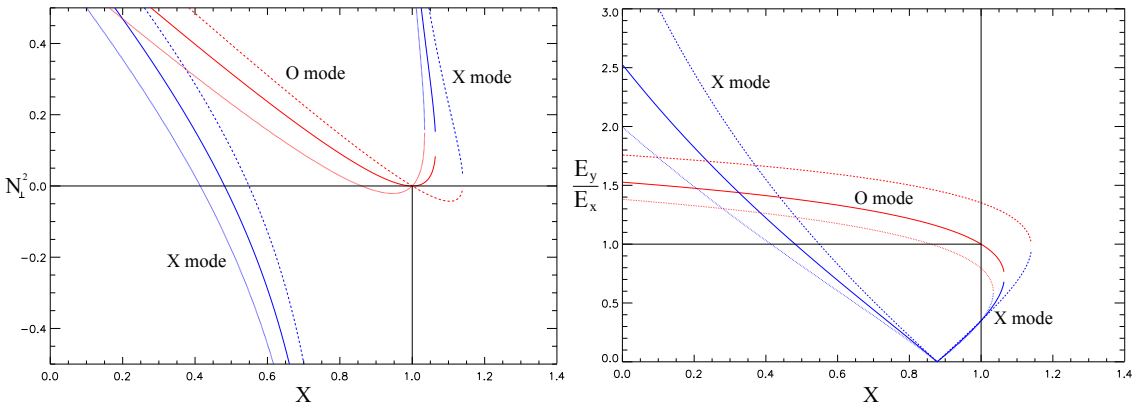

Figure 2.4: **Left**: The square of the perpendicular refractive index, $N_\perp^2$ for different values of incident angle. $N_\parallel = N_{\parallel,opt}$ solid lines, $N_\parallel = 0.8N_{\parallel,\mathrm{opt}}$ dotted lines, $N_\parallel = 1.2N_{\parallel,opt}$ dashed lines, here $Y = 0.35$ for clarity. We can see that for non optimal values of $N_\parallel$ a region of evanescence is accessed before continuation along the X branch of the dispersion relation. **Right**: The amplitude ratio $|E_y|/|E_x|$ for the same vales of $N_\parallel$. We can see that for the optimal value, the polarisation of the mode at $X = 1$ is circular.

carried out by Hansen et al [27].

$$\mathfrak{T} = \exp\left\{-\pi k_0 L_n \sqrt{Y/2}[2(1+Y)(N_{\parallel,opt} - N_\parallel)^2 + N_y^2]\right\} \tag{2.21}$$

where k_0 is the vacuum wavenumber and $L_n = n/(\partial n/\partial x)$ is the density scale length. Equation (2.21) gives a Gaussian bell in terms of $N_\parallel$ and ${N_y}^2$ and therefore gives rise to elliptical brightness contours in terms of viewing angles. This elliptical mode conversion window has its maximum at the critical angle given by (2.19) and is aligned along the magnetic field line: see Figure 2.5

This geometry may be extended to include other second order effects on the mode conversion efficiency. Cairns and Lashmore-Davis considered the effect of a magnetic shear either parallel or anti-parallel to the density gradient [28]. By following a similar procedure to Mjølhus, including a change of variables to account for the shear and defining the shear scale length as $L_\theta = \theta/(\partial\theta/\partial x)$ and the ratio of the scale lengths as $r = L_n/L_\theta$,

[2]Now N_y, not $N_\perp$ due to the fact that the x coordinate now contains the density gradient, breaking cylindrical symmetry

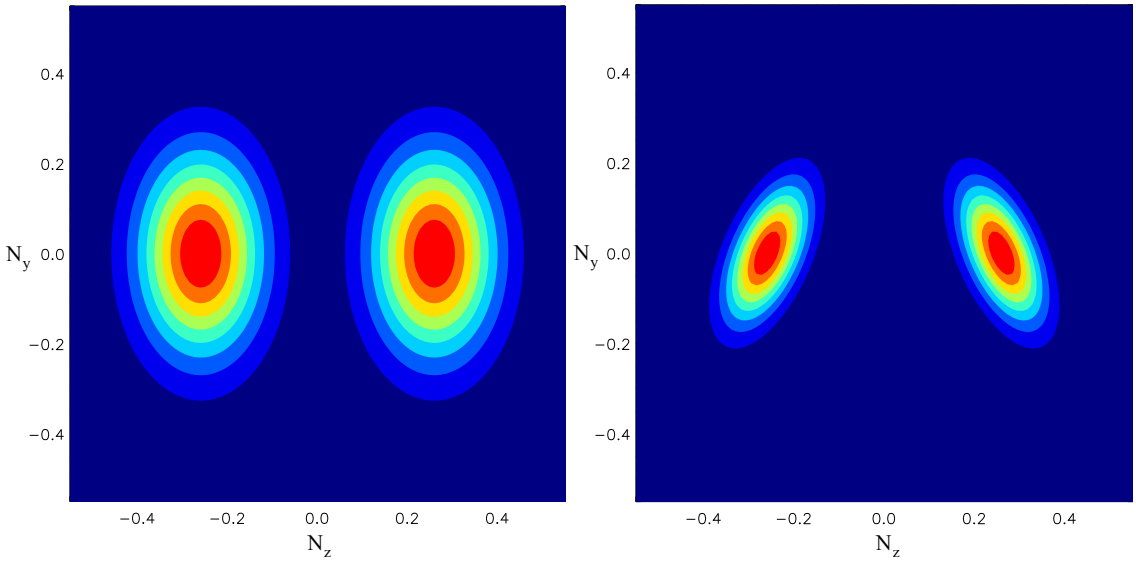

Figure 2.5: **Left**: A contour plot of the transmissivity as a function of N_y and N_z as given by Mjølhus. $f = 15$GHz, $L_n = 0.05$, $Y = 0.35$. **Right**: The transmissivity when the shear is included and given by Cairns and Lashmore-Davis. Here $L_\theta = -0.005$ for clarity. We can see the effect is to rotate the window about its centre of mass and compress reduce its width. A shear in the opposite direction causes a rotation in the opposite direction.

they showed the modified transmissivity to be:

$$\mathfrak{T} = \exp\left\{-\pi\frac{L_n\omega}{c}\frac{\left(\frac{2(N_{\parallel,opt}-N_\parallel)}{N_{\parallel,opt}} - rN_yN_{\parallel,opt}\right)^2 + N_y^2\left(\frac{2}{1+Y}\frac{1}{N_{\parallel,opt}^2} - r^2N_{\parallel,opt}^2\right)}{\left(\frac{2}{1+Y}\frac{1}{N_{\parallel,opt}^2} - r^2N_{\parallel,opt}^2\right)^{3/2}}\right\} \tag{2.22}$$

The effect of this modification is to introduce a tilt of the mode conversion window about its maximum in the presence of magnetic shear as demonstrated in Figure (2.20). One can see that this reduces to (2.21) in the event $r = 0$.

Both approaches to the problem of sX-O mode conversion above assume that the inhomogeneity is caused by the gradient in density and is also only in a single direction. In a tokamak however it may be the case that the magnetic field may vary over the mode conversion region and moreover, the field may vary in a different direction to the density, which leads to the possibility of the intersection of cut-off surfaces. The inclusion of in-

homogeneity in two dimensions will not be presented here but it has been discussed in [29, 30, 31, 32]; publications which are of particular note are by Shalashov and Gospodchikov [33] and Popov [34].

2.3.2 sX - B conversion

Let's consider the slow X wave generated by the process above. The wave then begins to propagate towards the Upper Hybrid Resonance (UHR) from the high density side. There are several things to consider as this wave approaches the resonance. The perpendicular component of the refractive index begins to rise sharply indicating that its phase velocity falls and as such so does its wavelength. In the cold plasma theory, the wave takes an infinite amount of time to reach the resonance as the refractive index is singular at this point. Collisional damping of the wave may occur as the electrons are accelerated in the wave field and then lose their kinetic energy in random collisions with the ions; this acts as a sink of energy for the X wave. The electron ion collision frequency, ν, is given by:

$$\nu = \frac{\ln \Lambda}{2\sqrt{2}\pi} \frac{\omega_{\mathrm{p}}^4}{n_{\mathrm{e}} v_{\mathrm{th}}}, \tag{2.23}$$

where lambda is the coulomb logarithm and is typically between[3] 10 and 20. This collision frequency is many orders of magnitude less than the wave frequency, but since the wave takes an infinite amount of time to reach the upper hybrid in the cold plasma theory, the wave is damped.

As we approach the upper hybrid, the wavelength shrinks to close to the size of the electron Larmor radius, which means that if we are to have an accurate description of the process we need a theory which includes the finite Larmor radius effects. This only comes when we allow the electrons to possess a finite thermal velocity as in Section 2.2 [35]. The X wave has a longitudinal component as pointed out by Chen [17] which grows as the X wave approaches the UHR. This longitudinal component begins to perturb the local electron

[3] See page 34 of the 2011 NRL plasma formulary

density, as we are now allowed some charge separation across the magnetic field. The electrons begin to participate in the perturbed electric field, adding their own component of field to the disturbance. As the wavelength of the X wave approaches $1/4\rho$ electron Bernstein waves are born and propagate the energy away from the UHR to higher density regions. This process is typically much more efficient than the collisional damping [36] and so will be considered to be 100% from here on in.

2.3.3 Direct X - B tunnelling

It is also possible to tunnel from the X mode in the vacuum straight to the Bernstein mode at the UHR [19]. If we look again at Figure 2.2 (b) we can see that the X mode dispersion relation has a triplet structure, i.e. a cut-off - resonance - cut-off structure. The right hand (high density) cut-off can be ignored if the distance between it and the UHR is much greater that the wavelength and we have a regular tunnelling problem. However in the case where the right hand cut-off is close to the UHR, as it can be in a tokamak H-mode, then we have may also have reflection from this cut-off and set up standing wave structures in that region leading to enhanced tunnelling from the left hand side. This form of tunnelling is covered by Ginzburg [19] for angles normal to the field. To quote the result given there

$$\begin{aligned} \mathfrak{T} &= 4e^{-\delta_0}\left(1-e^{-\delta_0}\right)\sin^2\frac{1}{2}\delta_0 \\ \delta_0 &= 2kL_nY^{3/2}\left(1-Y\right)\left(1+Y\right)^{1/2}\int_0^1\sqrt{\left(1-t^2\right)\left(1+\frac{1-Y}{1+Y}t^2\right)}\,dt \end{aligned} \tag{2.24}$$

This kind of tunnelling will produce an interference-like pattern with δ_0, enhancing or diminishing the transmitted signal due to the $\sin^2\frac{1}{2}\delta_0$ term which originates from including the high density cut-off. If we only include the change in L_n with angle we can reason that we would see rings on the high density cut-off surface provided the density gradient is high enough to allow efficient tunnelling.

2.4 Reasons for imaging the mode conversion

The electron Bernstein waves and their subsequent mode conversion are sensitive to many parameters. Their brightness depends on the temperature at which they are born and their refraction through the magnetic field. Their conversion to electromagnetic waves depends on the density gradient, the magnetic field vector, the mode conversion surface curvature, the magnetic shear and any and all fluctuations in these quantities thereof.

Simple one dimensional observations can and have provided some unique insights into these quantities and some of this work is referenced in this thesis where it is relevant. However, in order to take full advantage of this process and the information it contains one must have access to more information. Providing three dimensional images (angle and frequency) of the mode conversion process the amount of information drastically rises providing some new insight into the plasma properties that affect the mode conversion.

Section 1.4 introduced the idea that one can measure current densities with very fine radial resolution using a technique that uses observations of the mode conversion process. A technique using a fast rotating mirror to scan over the mode conversion window in time provided some intriguing results. There are a few problems involved with this technique however, the biggest being the limited time resolution due to the maximum rotation speed of the mirror, which doesn't allow several periods within an ELM cycle. Not only does this mean that we are unable to study how the physics changes in this period, but we must also assume that the parameters of the model that we're fitting don't change within one period of the mirror, which is certainly not true in general. There are also features of the spinning mirror data that are relatively static and are not fitted by the model. With this in mind there are obvious benefits to obtaining an entire image at a given time.

There have not been any images of the mode converted emission from a tokamak plasma to date. This means that there is potentially a wealth of untouched physics in this process. For example all of the studies of the mode conversion in tokamaks has been limited to the midplane. What happens off midplane when the effects of two dimensional inhomogeneities are more important Or what happens on small timescales? The majority of EBW

emission studies report a high level of intensity fluctuations $\delta I/I$ in H mode; what causes this? The hope is that the increased information one gets from forming 2D images of the emission will shed light on some of these questions and perhaps raise others.

Chapter 3

Interferometric imaging in the microwave region

3.1 Microwave imaging techniques

The conventional approach to imaging microwave emission in laboratory plasmas is to use optical components, such as mirrors and lenses, to focus radiation from the plasma onto a plane of detecting antennas [37, 38]. We may however consider an alternative in this frequency range as it is possible to perform phase sensitive detection. If we are able to record the phase and amplitude of the electric field at a number of different points, this allows us to use the principle of constructive interference to focus the imaging device by altering the phase of the recorded signals. If we digitally record the information in full vector form, we are able to perform this focusing after the fact, choosing from any number of focusing schemes [39, 40].

There is also a further advantage resulting from the total number of constraints which we can put on the real brightness distribution from our measurements. In the case of conventional imaging, the total number of constraints on the image is equal to the number of antennas n_a, as the image is made up of n_a pixels. In the phase sensitive case however, the reconstructed image is the result of a convolution of the real image with the array beam pattern. This beam pattern, as we shall see later, is made up of Fourier components from

each antenna pair. This gives us a total of $n_a(n_a - 1)$ constraints on the image [41]. As the number of antennas rises we have of order n_a^2 image constraints in the phase sensitive case and only n_a constraints in the conventional case. Provided the array configuration is designed to minimise the redundancy in these antenna pairs and minimise the level of oscillations in the array beam pattern, this can be a great advantage.

The phase-sensitive method, then, has no lenses or mirrors and the potential of higher image quality. It is however subject to some drawbacks. The phase sensitive system requires preserving the relative antenna phase over many meters of signal transmission, which is typically non-trivial. It also requires a very high data throughput if the signal manipulation is to be done computationally. Further, the images produced are often more difficult to interpret, being subjected to a convolution of a non-trivial array beam pattern. If one designs a system which accepts signals from both above and below the desired centre frequency, we must record double the number of channels per antenna, both real and imaginary components, if the phase is to be preserved, this is elaborated on in section 4.1.1.

With these points in mind it was decided that a phased array should be built to facilitate measurements of the microwave emission from MAST.

3.2 Phased arrays and aperture synthesis

Consider the situation illustrated in Figure 3.1, which shows two antennas being illuminated by a point source at a distance much further than the distance between the two antennas. There is a phase difference in the radiation received at the two antennas due to the extra distance the radiation has had to travel to reach one of the antennas over the other. If we were to collect the antenna signals and then add them together, the signals from these antennas would constructively interfere if the phases were adjusted so as to compensate for this difference. Thus we may direct the sensitivity of the two antennas by ensuring that we have constructive interference between signals which have approached from the direction of interest. In the case where the source is much further from the antennas than

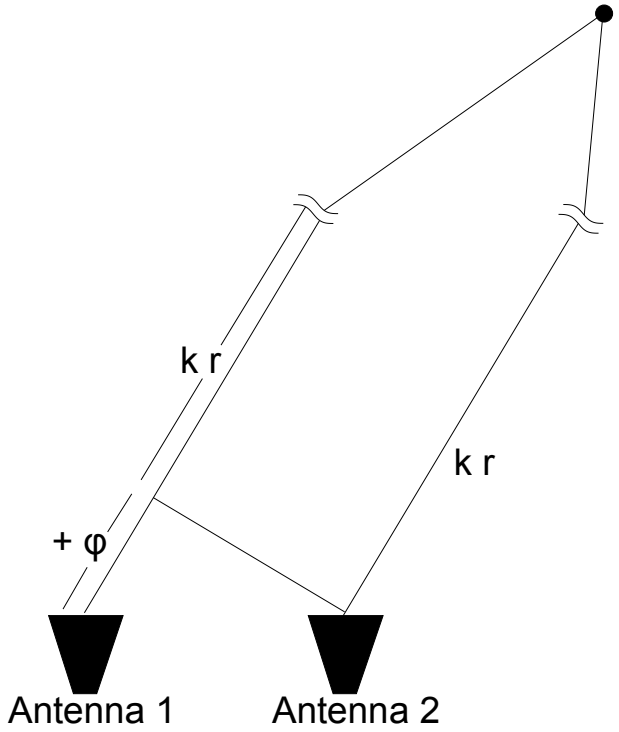

Figure 3.1: The phase difference between two antennas for emission from a point source is a function of the incident angle of the radiation. These signals will constructively interfere if they are adjusted in phase so as to compensate this difference.

the distance between the antennas this phase difference ϕ may be written in terms of a dot product of the vector between the two antennas, $\boldsymbol{b}$, and a unit vector in the direction of the source, $\hat{\boldsymbol{\alpha}}$ [42, 43].

$$\phi = k\boldsymbol{b} \cdot \hat{\boldsymbol{\alpha}} \tag{3.1}$$

here $k = 2\pi/\lambda$ is the wavenumber and λ is the vacuum wavelength. In general, constructive interference between two signals will be produced for any ϕ_{possible} which differs from ϕ by an integer multiple of 2π. To help avoid this ambiguity, we may add the signals from antennas at several different locations. We may then build up an image of the emission amplitude by adjusting the phases on several antennas such that we scan the array direction across the area of interest, recording the summed signal's amplitude as a function of

angle.

To take this further let us write the total voltage received at the i^{th} antenna, s_i, as a sum over an infinite number of point sources, and let us take the origin of our coordinate system as an arbitrary phase reference. Then:

$$s_i = \frac{1}{r_i} \int g\left(\boldsymbol{r}_i\right) E\left(\boldsymbol{x}\right) e^{ik(r_i - x)} \, d\boldsymbol{x} \tag{3.2}$$

where we have used the coordinate system illustrated in Figure 3.2 and $g\left(\boldsymbol{r}_i\right)$ is the antenna voltage gain pattern.

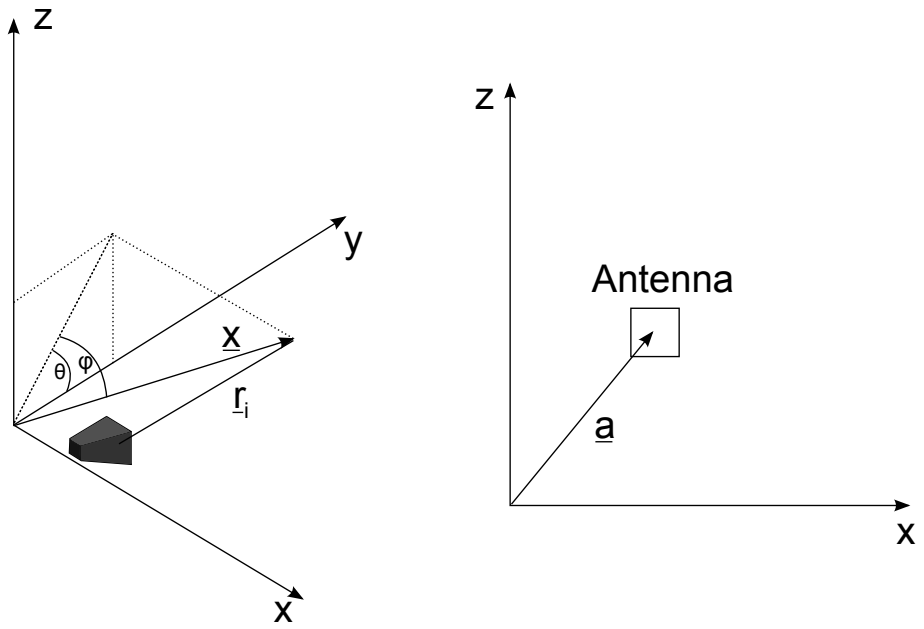

Figure 3.2: The coordinate system for describing the array. Here, $\boldsymbol{r}_i$ is the vector from the centre of the antenna aperture to point $\boldsymbol{x}$, and $\boldsymbol{a}_i$ describes the antenna location, which lies in the $\{x, z\}$ plane. $\boldsymbol{r}_i = \boldsymbol{x} - \boldsymbol{a}_i$.

If we now approximate the vector magnitude in the exponent as the projection of a unit vector in the direction of the source $\hat{\boldsymbol{\alpha}}$, i.e. $r_i - x \simeq \boldsymbol{a}_i \cdot \hat{\boldsymbol{\alpha}}$ and neglect the amplitude difference between antennas due to the antennas' displacement, we may write:

$$
\begin{aligned}
s_i &= \int g\left(\hat{\boldsymbol{\alpha}}\right) E\left(\hat{\boldsymbol{\alpha}}\right) e^{ik\boldsymbol{a}\cdot\hat{\boldsymbol{\alpha}}} d\hat{\boldsymbol{\alpha}} \\
&= \int g\left(\eta,\xi\right) E\left(\eta,\xi\right) e^{ik(a_{x,i}\eta + a_{z,i}\xi)} d\eta\, d\xi
\end{aligned} \tag{3.3}
$$

where we have cast the dot product in our coordinate system explicitly, $\eta = \sin\phi, \xi = \cos\phi\sin\theta$. We identify this as a Fourier transform of the product of the complex electric field multiplied by the antenna voltage gain pattern.

We may recognise the relation in (3.3), as a Fourier transform relationship between the quantities $g\left(\eta,\xi\right) E\left(\eta,\xi\right)$ and $s_i\left(\frac{a_{x,i}}{\lambda}, \frac{a_{z,i}}{\lambda}\right)$. Thus, s_i measured at a particular location in the $\{x, z\}$ plane is a sample of this Fourier transform. Measuring antenna voltages at multiple locations simultaneously allows us to sample this Fourier transform and make an estimate of the complex field via the inverse Fourier transform:

$$
\tilde{g}\left(\eta,\xi\right)\tilde{E}\left(\eta,\xi\right) = \sum_{i=1}^{n_a} s_i e^{-ik(a_{x,i}\eta + a_{z,i}\xi)} \tag{3.4}
$$

If we then wish to estimate the intensity distribution, $\tilde{I}(\eta,\xi)G(\eta,\xi)$, we need to take the product of this estimate with its complex conjugate,

$$
\tilde{I}(\eta,\xi)G(\eta,\xi) = \sum_{i=1}^{n_a} s_i e^{-ik(a_{x,i}\eta + a_{z,i}\xi)} \sum_{j=1}^{n_a} s_j^* e^{ik(a_{x,j}\eta + a_{z,j}\xi)} \tag{3.5}
$$

Expression (3.5) contains all the information necessary to provide an estimate of the power distribution and there is no difficulty, even in practice, of evaluating it. There are gains to be made however by following the argument a little further. First note that the n_a terms which are like $s_i s_i^*$ simply denote the power measured at an individual antenna since all the phase terms exactly cancel. Thus it is the remaining $n_a(n_a - 1)$ cross terms which are responsible for the shape of the reconstructed image. With this in mind let us define the cross correlation function as:

$$
\Gamma_{i,j} \equiv \int s_i s_j^* dt = \langle s_i s_j^* \rangle, \tag{3.6}
$$

The angular brackets denote a time average from here on. Substituting the expression (3.2) into equation (3.6) we may write

$$\begin{aligned}\Gamma_{i,j} &= \frac{1}{r_i r_j}\left\langle \int E(\boldsymbol{x})\, g(\boldsymbol{r}_i)\, e^{ik|\boldsymbol{r}_i-\boldsymbol{x}|}\, d\boldsymbol{x} \int E(\boldsymbol{x}')\, g(\boldsymbol{r}_j)\, e^{-ik(r_j-x')}\, d\boldsymbol{x'} \right\rangle \\ &= \frac{1}{r_i r_j}\int\int \langle E(\boldsymbol{x})\, E^*(\boldsymbol{x}')\rangle\, g(\boldsymbol{r}_i)\, g^*(\boldsymbol{r}_j)\, e^{ik(r_i-x-r_j-x')}\, d\boldsymbol{x}\, d\boldsymbol{x'} \end{aligned} \tag{3.7}$$

Now we impose the additional constraints on our source that it be incoherent [44]. That is that the field emission from one part of the source is *uncorrelated* from any other. Mathematically this implies that [45, 44]

$$\langle E(\boldsymbol{x})\, E(\boldsymbol{x}')\rangle = I(\boldsymbol{x})\, \delta((x) - \boldsymbol{x}') \tag{3.8}$$

With this condition and the far field approximations made above, the expression (3.7) reduces to

$$\Gamma_{i,j} = \int G(\eta,\xi)\, I(\eta,\xi)\, e^{ik(u\eta+v\xi)}\, d\eta\, d\xi, \tag{3.9}$$

where we have used the definition $u = b_x/\lambda$ and $v = b_z/\lambda$ and also set the x and z components of $\hat{\boldsymbol{\alpha}}$ to be $\xi = \sin\theta$ and $\eta = \cos\theta \sin\phi$ respectively. Equation (3.9) can be identified as a sample of the two dimensional Fourier transform of the product of the brightness distribution and antenna gain pattern at a point in Fourier space $\{u, v\}$. Knowing this we may construct an array of antennas where we measure the cross correlations of each pair of antenna voltages, thus sampling the Fourier transform of our desired image. If we have enough antenna pairs, we may have enough samples in Fourier space to perform an inverse Fourier transform and obtain an approximation to the image. The above is known as the van Cittert - Zernike theorem [46, 47] and describes the propagation of spatial coherence [48].

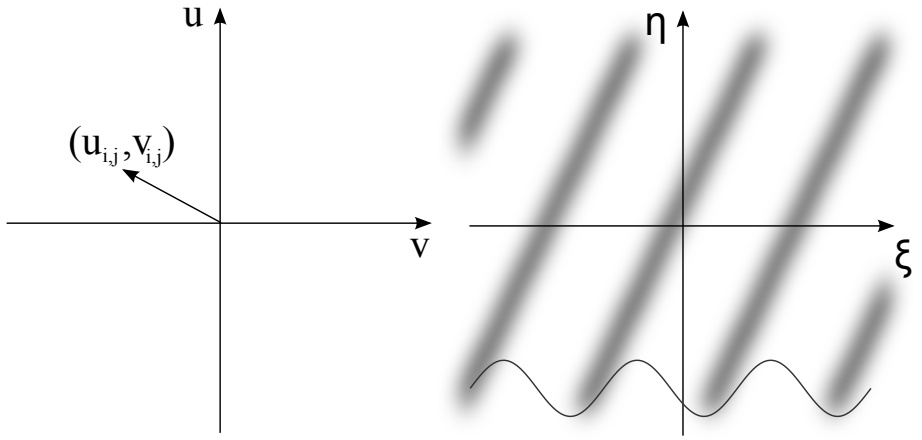

Figure 3.3: The u, v coordinates map to complex wave basis functions in ξ, η. The direction and frequency of the wave in ξ, η is controlled by the length and direction of the vector $u_{i,j}, v_{i,j}$, and the phase and amplitude of the basis function is set by the measurement of the complex correlation of antennas i and j.

3.2.1 The Fourier plane

The problem described in section 3.2 highlights an important coordinate space for performing aperture synthesis imaging, namely the $\{u, v\}$ coordinates. These are the Fourier dual coordinates to $\{\xi, \eta\}$ and depend only on the positions of the antennas relative to each other and the vacuum wavelength of the radiation being observed.

The measurement of a cross correlation of antenna voltages $\Gamma_{i,j}$ corresponds to the measurement of the amplitude and phase of a wave-like structure in the $\{\xi, \eta\}$ coordinates as shown in Figure 3.3. The direction and spatial frequency of this wave is given by the location of the corresponding baseline in $\{u, v\}$ space. The image, to first order, is the summation of these waves for all points measured in the $\{u, v\}$ space, which in turn is defined only by the array geometry and the wavelength of the radiation. Thus which basis functions can and cannot exist in the reconstructed image is given by the array geometry.

Another note to be made about the $\{u, v\}$ plane comes from the Hermitian symmetry of the cross correlation, i.e.

$$\Gamma^*_{i,j}(u,v) = \Gamma_{i,j}(-u,-v) \tag{3.10}$$

Hence there is a reflective symmetry in the $\{u,v\}$ plane. This can be seen from a physical standpoint by considering the cross correlation of two antennas, first going from antenna 1 to 2, then from 2 to 1. It is clear that the correlations contain the same information, but the phase difference between them is reversed since the phase reference is changed. This will be an important point for the measurement of the polarisation of the radiation.

3.2.2 Including the effect of polarisation

In order to see how we may include the effects of polarisation, it is first useful to introduce the Stokes parameters. The Stokes parameters form a vector which contains full information about the polarisation of incident radiation. If we define the electric field as in terms of the complex components E_x and E_z like so:

$$\boldsymbol{E} = \left(E_x\hat{\boldsymbol{x}} + E_z\hat{\boldsymbol{z}}\right)e^{i\omega t} \tag{3.11}$$

The four components, I, Q, U and V are defined as:

$$\begin{aligned} I &= \langle E_x^2(t)\rangle + \langle E_z^2(t)\rangle \\ Q &= \langle E_x^2(t)\rangle - \langle E_z^2(t)\rangle \\ U &= 2\Re\langle E_x(t)\,E_z^*(t)\rangle \\ V &= 2\Im\langle E_x(t)\,E_z^*(t)\rangle \end{aligned} \tag{3.12}$$

I is a measure of the total intensity of the radiation, Q and U represent the linearly polarised components, and V represents the circularly polarised components. These can be interpreted in a more directly physical way via:

$$
\begin{aligned}
m_l &= \frac{\sqrt{Q^2+U^2}}{I} \\
m_c &= \frac{V}{I} \\
m_t &= \frac{\sqrt{Q^2+U^2+V^2}}{I} \\
\theta &= \frac{1}{2}\arctan\left(\frac{U}{Q}\right)
\end{aligned}
\tag{3.13}
$$

where m_l, m_c and m_t are the total fractions of power polarised in linear, circular and total polarised respectively [49]. θ is the position angle of the plane of linear polarisation. The parameter m_t is only required when the signals have an unpolarised part, such as may occur with either thermal or scattered light.

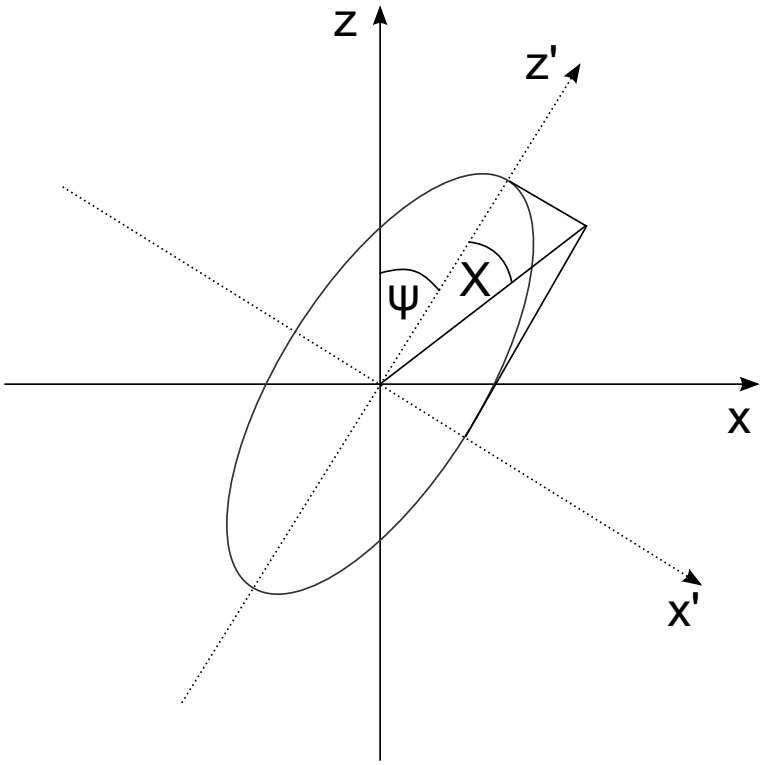

Figure 3.4: Any antenna's response to polarised radiation can be described in terms of its polarisation ellipse. The parameter ψ describes the inclination of the ellipse and χ describes the degree of ellipticity.

We may describe an antenna's response to polarised radiation by defining its polarisation

ellipse as demonstrated in Figure 3.4. Here ψ is the angle between the principal axis of the antenna polarisation ellipse and the normal z axis, known as the position angle. χ is the ellipticity angle and describes the degree of ellipticity.

If we consider the coordinates set out in Figure 3.4 we may write the field components $\{E_{x'}, E_{z'}\}$ in terms of $\{E_x, E_z\}$ like so:

$$\begin{aligned} E_{x'} &= E_x \cos\psi - E_z \sin\psi \\ E_{z'} &= E_x \sin\psi + E_z \cos\psi. \end{aligned} \tag{3.14}$$

The antenna response is then given by

$$\begin{aligned} s_i &= E_{z',i} \cos\chi_i - iE_{x',i} \sin\chi_i \\ &= (E_x \sin\psi_i + E_z \cos\psi_i)\cos\chi_i - i\,(E_x \cos\psi_i - E_z \sin\psi_i)\sin\chi_i \end{aligned} \tag{3.15}$$

The complex factor represents a phase shift in the signal from z' to x'. Here we will only be interested in linearly polarised antennas so we set $\chi_i = 0$. With this new description of the electric field received by an antenna we may insert 3.15 into 3.6 to obtain

$$\begin{aligned} \Gamma_{i,j} = \frac{1}{2}[&(I_v + Q_v)\sin\psi_i \sin\psi_j \\ &+ (U_v + iV_v)\sin\psi_i \cos\psi_j \\ &+ (U_v - iV_v)\cos\psi_i \sin\psi_j \\ &+ (I_v - Q_v)\cos\psi_i \cos\psi_j] \end{aligned} \tag{3.16}$$

The Stokes parameters here have an subscript v to denote that they are the so-called stokes visibilities. These are measurements of the sample of the Fourier transform of the Stokes maps at the location $\{u, v\}$.

We may note at this point that for completely unpolarised radiation as considered in section 3.2, $U_v = V_v = Q_v = 0$ and we recover the equations derived there.

If we consider antennas of position angles taking either 0 or $90°$ we can see that to measure I_v for example we require a correlation of two antennas at $0°$ and then *along the same baseline* two antennas at $90°$. We may then add these two measurements to obtain I_v or subtract them to obtain Q_v. Similarly if we are interested in circularly polarised emission, we may take two antennas at $0°$ and $90°$ and *along the same baseline* antennas at $90°$ and $0°$. Adding these gives us U_v and subtracting gives us iV_v.

For the measurement of circular polarisations one may be tempted into thinking we may take the correlation between an antenna at $0°$ and one at $90°$ and then simply reverse the direction of correlation to obtain the other necessary measurement. This is not the case since the symmetry described in equation (3.10) forbids us from gaining any new information from this process. In this case there is a phase difference associated with the propagation of the radiation and a phase difference associated with the rotation of polarisation. We must keep the same baseline direction in order to distinguish these.

3.2.3 The sensitivity of an aperture synthesis radiometer

Radiometric sensitivity is defined as the minimum input change that can be detected at the output [50]. With this in mind let us calculate the standard deviation of the amplitude of the cross correlation following the procedure in [50, 51, 52]. The variance of a cross correlation $\sigma_{i,j}$ of two signals v_i and v_j is given in terms of their 4^{th} order correlation and the magnitude of the 2^{nd} order correlation. For an integration period T of a signal of bandwidth B we find that

$$\sigma_{i,j}^2 = \frac{\langle v_i v_i^* v_j v_j^* \rangle - |\langle v_i v_j^* \rangle|^2}{2TB} \tag{3.17}$$

Using the identity that for circular, complex, zero mean Gaussian random variables [45]

$$\langle v_i v_i^* v_j v_j^* \rangle = \langle v_i v_i^* \rangle \langle v_j v_j^* \rangle + |\langle v_i v_j^* \rangle|^2 \tag{3.18}$$

for signals with additive noise n_i i.e. $v_i = s_i + n_i$, neglecting all the uncorrelated terms subjected to averaging and recognising that $s_i s_i^* = P_{\text{signal},i}$ and $n_i n_i^* = P_{\text{noise},i}$ we find that

$$\sigma_{i,j}^2 = \frac{\left(P_{\text{signal},i} + P_{\text{noise},i}\right)\left(P_{\text{signal},j} + P_{\text{noise},j}\right)}{2TB} \tag{3.19}$$

The expression (3.19) holds for uncorrelated noise and gives us a good estimate of the noise present in the correlation measurement. However, as we shall see later it is possible to have correlated noise which further limits the sensitivity of the radiometer.

3.2.4 The effect of antenna cross talk

When dealing with phased arrays, one must account for the many ways which a signal may reach your digitiser in order to have a complete picture of what is going on. Of particular importance when dealing with wide field arrays, with a small number of antenna elements which are irregularly spaced, is the mutual coupling between antenna elements. Figure 3.5 illustrates the many ways which a signal may pass through the RF part of the system. 1) Signals approaching the antenna may be picked up in the regular way. 2) Some proportion of this signal is then reflected due to the fact that there is non-perfect impedance matching between the air and the coaxial transmission line. This reflected signal is then re-emitted by the antennas and some proportion of this signal is subsequently picked up by neighbouring antennas. 3) The thermal noise of the amplifiers may be emitted by the antennas and subsequently be picked up by the neighbouring antennas. 4) The result is a superposition of all these signals. Many of which are well below the amplitude of the main signal. While at first this does not appear to be a significant problem, it is the coherence of these signals which ensures a small but non-negligible effect on the cross-correlations. Unlike the other unwanted signals, such as the main component of the system noise, these signals will not average to zero in the correlation.

To examine the effect of these signals, lets consider the recieved signal to be a superposition of the main signal s_i, the component of the signal from the neighbouring antenna s_j,

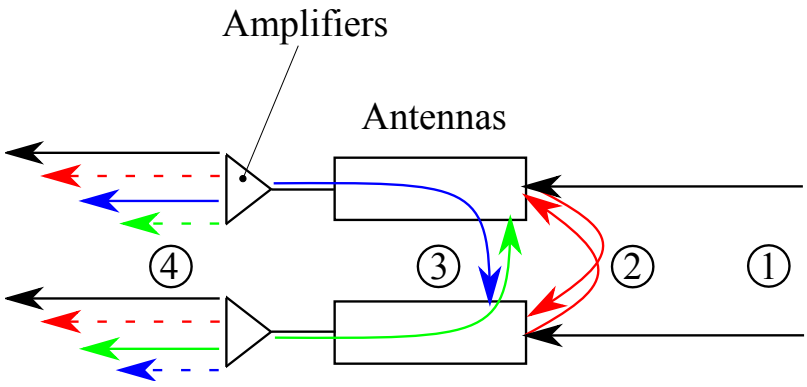

Figure 3.5: A diagram illustrating the different ways a signal can propagate at the antenna. 1) The signal comes in from the source as we have been assuming. 2) Part of this signal may be then be reflected and re-emitted by the antenna, consequently being picked up by its neighbours. 3) Thermal noise from the amplifiers may be emitted and picked up by neighbouring antennas. 4) All of these signals make up the measured signal and affect the cross correlation in different ways.

phase shifted and attenuated by the complex scattering parameter $S_{i,j}$, the noise n_i and the phase shifted and attenuated noise from the neighbour $r_{i,j}n_j$:

$$v_i = s_i + n_i + S_{i,j}s_j + r_{i,j}n_j \tag{3.20}$$

Now we may assume that $S_{i,j} = S^*_{j,i}$ and that $|S_{i,j}| \ll 1$. Then, neglecting all the uncorrelated terms and terms which are second order in $S_{i,j}$, we may write the cross correlation $v_i v_j^*$ as in terms of the wanted cross correlation $\Gamma_{i,j}$, the antenna power $P_{\mathrm{Ai}} = s_i s_i^*$ and the noise power $P_{\mathrm{ni}} = n_i n_i^*$. We get:

$$v_i v_j^* = s_i s_j^* + S_{i,j}\left(P_{\mathrm{Ai}} + P_{\mathrm{Aj}}\right) + r_{i,j}\left(P_{\mathrm{ni}} + P_{\mathrm{nj}}\right) \tag{3.21}$$

The cross correlation to first approximation, therefore only contains additive terms of a constant phase. The noise cross term is proportional only to the sum of noise powers which is easily measured, and the antenna cross term is proportional only to the sum of antenna powers. We now see that the two effects may affect us in different circumstances. The antenna cross talk will affect us when the signal amplitude is high, but the correlations

are low; this can often be the case. The noise correlation may affect us when either the signal amplitude is low, or when the correlations are low.

The noise term is very straightforwardly estimated by taking correlations when no signal is present. These may then be simply subtracted from the correlation measurements. The signal cross term is more difficult to estimate, since the cross correlation term $\Gamma_{i,j}$ must be known to a high degree of accuracy, due the fact that $|S_{i,j}| \ll 1$. One option is to have a very bright, very uniform noise source. In this case the antenna amplitude will be high, but the correlations will approach zero. We may then subtract the resulting correlations scaled appropriately with the antenna power to remove this effect all together.

This elegant method of cross talk subtraction was first realised by Dong et al [53], however they do not formulate the problem including noise cross talk between the antennas. It is considerably simpler than previous attempts [54, 55, 56, 57], which try and correct the antenna signals directly in various different ways.

3.2.5 Fringe washing - the effect of finite bandwidth

Until now, we have only been working with signals which are quasi-coherent. That is to say we have assigned our signals a definite frequency, whilst still allowing some of the benefits of having a finite bandwidth. The assumption in 3.8, for example could not be valid if we had a only a single frequency, since it suggests there is no stable phase relationship between point in the image. A truly monochromatic source cannot change its phase and hence there must always be a stable phase relationship. Apart from this implicit assumption, there is something to be learned from explicitly considering the effects that a finite bandwidth may have on cross correlations of antenna signals.

Let us consider the phase shift in expression 3.1 as a physical geometrical delay, τ_g and consider the autocorrelation in its more general form, as a function of time delay:

$$\Gamma(\tau) = \langle s(t)\, s^*(t - \tau_{\mathrm{g}}) \rangle \tag{3.22}$$

The well known Wiener-Khinchine relation [58, 59] states that that the power spectrum of a signal is the Fourier transform of the autocorrelation function of that signal. This theorem holds whether the signal is deterministic or statistical and may be written as:

$$|H(\nu)|^2 = \int_{\infty}^{\infty} \Gamma(\tau_{\mathrm{g}})\, e^{i2\pi\nu\tau_{\mathrm{g}}} d\tau_{\mathrm{g}} \tag{3.23}$$

and

$$\Gamma(\tau) = \int_{\infty}^{\infty} |H(\nu)|^2 e^{i2\pi\nu\tau_{\mathrm{g}}} d\nu \tag{3.24}$$

where $H(\nu)$ in this case is the amplitude response as a function of frequency, ν, of the receiving system. If we assume this to be a Gaussian with bandwidth factor σ, like so [49]:

$$|H(\nu)|^2 = \frac{1}{2\sigma\sqrt{2\pi}} \exp\left\{-\frac{(\nu-\nu_0)^2}{2\sigma^2}\right\} \tag{3.25}$$

and calculate the correlation response from 3.24, we get:

$$\Gamma(\tau_{\mathrm{g}}) = \exp\left\{2\pi^2\sigma^2\tau_{\mathrm{g}}^2\right\} \exp\left\{i2\pi\nu_0\tau_{\mathrm{g}}\right\} \tag{3.26}$$

We can see from equation 3.26 that we retain the usual correlation function expressed in 3.9, if we substitute τ_{g} for the phase in expression 3.1 in the second exponential. But it is enveloped by another exponential function which depends on the bandwidth of the receiving system and the geometrical delay.

So the effect of the bandwidth, then, is to decrease the correlation magnitude with increasing delay between the signals. This decorrelation effect is called fringe-washing [49, 60, 61], because of its tendency to "wash out" or reduce the correlations.

This is a particular problem for large interferrometric arrays, when the delay from one side to the other can be significant. In our diagnostic this effect is negligible. It is however

significant when considering the effect of multiple reflections as we do in section 5.3.2, when we look at calibrating the diagnostic by directing a source through the MAST vessel.

Chapter 4

Hardware design and implementation

We now go on to consider the design, construction and performance of the hardware developed to make SAMI. Each part of the diagnostic has been developed by the SAMI team at Culham, right down to the design and construction of the digitiser and the antennas themselves. The spinning mirror experiment in section 1.4 informed us of a frequency range of interest between 10 GHz and 14 GHz. The reason is that interesting effect could be seen at the fundamental harmonic, typically up to 18 GHz and the third harmonic spinning mirror measurements were in agreement with another magnetic field diagnostic which measures the Motional Stark Effect (MSE) [62].

As is shown in figure 4.1, SAMI uses antipodal Vivaldi antennas to feed signals into a full vector heterodyne frequency down-converter. This heterodyne down-converter is designed in order to minimise the signal loss and maximise the signal-to-noise ratio. The signals are then passed to two 14 bit 250MHz digitisers. These digitisers are controlled by Field Programmable Gate Arrays (FPGAs), the firmware for which was developed specifically for SAMI by Huang and Vann [63, 64]. Once the signals are digitised all the signal processing and image formation is done offline on a dedicated computer.

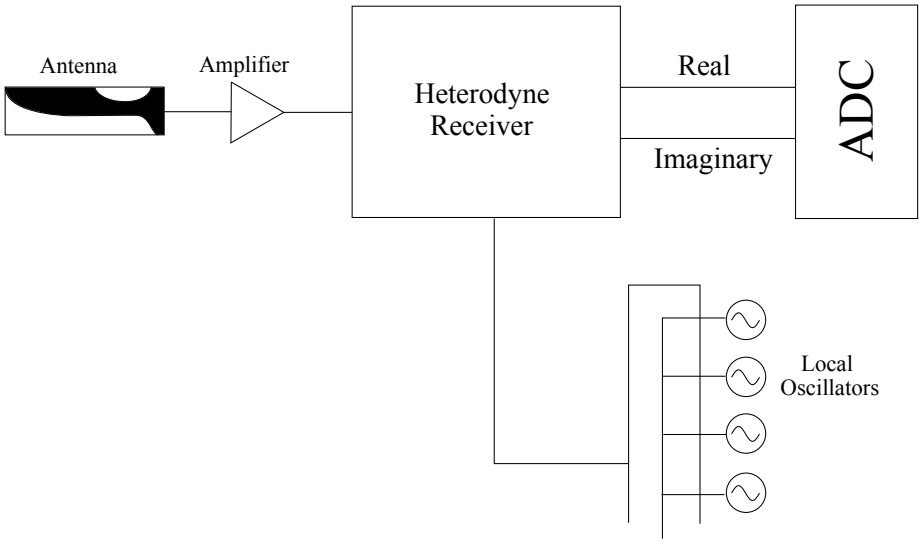

Figure 4.1: A broad schematic of the signal path for one of SAMIs 8 antenna channels. The signal from the antenna goes into a heterodyne receiver, which is also fed with a local oscillator. The heterodyne receiver converts the antenna signal into real and imaginary baseband signals. Here we consider the heterodyne down-converter to be the combination of the tuner and the local oscillator.

4.1 The full vector heterodyne down-converter

4.1.1 The heterodyne and sideband principles

Given the range of frequencies in which we are interested, we must build a receiver which can tune into a relatively narrow bandwidth around several frequencies in this range. Also, given the very wide range of frequencies, we must construct a system which is very wideband. To deal with these two points, we designed a full-vector heterodyne down-converting system, which resorted to coaxial technology, accepting the higher attenuation that this brings at the higher end of the operating range in favour of the simplicity of eliminating the frequency bands introduced by wave-guide transmission.

The heterodyne system involves multiplying the incoming high frequency signal ω_{RF} with a known high frequency local oscillator signal ω_{LO}. The result is a signal which contains frequencies $\omega_{\mathrm{RF}} + \omega_{\mathrm{LO}}$ and $\omega_{\mathrm{RF}} - \omega_{\mathrm{LO}}$. Passing this then through a low pass filter of

bandwidth B removes the $\omega_{\mathrm{RF}} + \omega_{\mathrm{LO}}$ part of the signal and allows us to effectively tune into radiation in the band $\omega_{\mathrm{LO}} \pm B$. Practically, the $\omega_{\mathrm{RF}} + \omega_{\mathrm{LO}}$ part of the signal is filtered out by strong suppression in the coaxial transmission and by the low noise amplifiers which sit just infront of the heterodyne receiver. The bandwidth, B, of the system is then set by a low-pass filter infront of the digitiser designed to prevent aliasing.

Frequencies $(\omega_{\mathrm{LO}} - B) < \omega_{\mathrm{RF}} < \omega_{\mathrm{LO}}$ form the so called lower sideband and frequencies $\omega_{\mathrm{LO}} < \omega_{\mathrm{RF}} < (\omega_{\mathrm{LO}} + B)$ form the upper sideband. This distinction is important as we may realise from considering a signal made of a superposition of an upper sideband signal and a lower sideband signal,

$$s = \cos\left[\left(\omega_{\mathrm{LO}} + \delta\omega_{\mathrm{u}}\right) t + \phi_{\mathrm{u}}\right] + \cos\left[\left(\omega_{\mathrm{LO}} - \delta\omega_{\mathrm{l}}\right) t + \phi_{\mathrm{l}}\right] \tag{4.1}$$

If we now multiply s by a local oscillator signal $\cos\left(\omega_{\mathrm{LO}} t\right)$ and keep only the terms which would survive the low pass filter we are left with

$$s = \frac{1}{2}\left[\cos\left(\delta\omega_{\mathrm{u}} t + \phi_{\mathrm{u}}\right) + \cos\left(\delta\omega_{\mathrm{l}} t - \phi_{\mathrm{l}}\right)\right] \tag{4.2}$$

The expression (4.2) reveals the principle difference between the upper and lower sidebands after mixing (multiplying by the local oscillator signal) that is the phases behave oppositely in upper and lower sidebands. This especially important for a phase sensitive device as this behaviour makes measuring the phase of dual sideband signal very difficult. We may however use this principle to construct a system, as is often done in heterodyne detectors, to completely suppress the upper or lower sideband. Consider the two signals s_1 and s_2. The latter is simply the former with a $\pi/2$ phase shift *before* the mixing stage, so $\phi_{\mathrm{u}} = \phi_{\mathrm{l}} = \pi/2$. Consider also two signals $\hat{s}_1$ and $\hat{s}_2$ which are simply s_1 and s_2 with $\pi/2$ phase shifts introduced *after* the mixing stage. Here the hat operator denotes a Hilbert transform rather than the usual unit vector notation and has the efect of shifting the signal by 90° in ph ase. After some algebra we can obtain:

$$
\begin{aligned}
s_1 - \hat{s}_2 &= \cos\left(\delta\omega_{\mathrm{u}} t + \phi_u\right) \\
\hat{s}_1 + s_2 &= -\sin\left(\delta\omega_{\mathrm{u}} t + \phi_u\right) \\
s_1 + \hat{s}_2 &= \cos\left(\delta\omega_{\mathrm{l}} t - \phi_l\right) \\
\hat{s}_1 - s_2 &= -\sin\left(\delta\omega_{\mathrm{l}} t - \phi_l\right)
\end{aligned} \tag{4.3}
$$

In practice this separation is limited by the phase and amplitude imbalance of s_1 and s_2. Often these imbalances can be corrected for, leading to high values of suppression of either sideband.

The ability to separate the two sidebands from each other allows us to effectively double the number of frequency channels available, giving us two closely spaced channels of bandwidth B for each local oscillator frequency.

In hardware we may split the heterodyne down-converter into two sections which here we will call the local oscillator and the heterodyne receiver.

4.1.2 The local oscillator

The local oscillator designed for SAMI consists of 16 fixed frequency Dielectric Resonance Oscillators (DROs) covering the range from 5 - 17.25 GHz (half the tuning frequencies due to the use of second harmonic mixers, see section 4.1.3). These oscillators feed into a sixteen to one switch, which is able to switch in less than half a microsecond and is controlled by the FPGA. The oscillator signal is then split sixteen ways by five one-to-four power dividers and the signal is boosted by power amplifiers (see figure 4.2). The signal power is then tuned by a series of attenuators to provide the correct power to within 1 dB to the mixers. This arrangement offers a few advantages over the alternative Voltage Controlled Oscillators (VCOs):

- The DROs have a much greater frequency stability than than VCOs.
- The DROs also have a much lower amplitude and phase noise, resulting in a much lower noise in the receiver.

- The switch means that any number of frequencies in any order can be selected allowing for example to switch quickly between frequency 4 and 10 only. This also allows us to vary the temporal resolution for a given frequency by reducing the sweep time.
- The frequency channels are precisely set and can be calibrated individually. This also means that we can avoid sweeping up through system resonances as we would with a VCO, thereby making the calibration more reliable.

Another alternative to the proposed system would be a Direct Digital Synthesis (DDS) technique. DDS allows the generation of a high quality local oscillator signal in any chosen frequency in our range. The typical switching time of a DDS system can be down to tens of nanoseconds. However, the DDS systems were outside the budget of the SAMI development and so the above solution was settled on as a good compromise.

4.1.3 The heterodyne receiver

Each antenna signal feeds directly into a Low Noise Amplifier (LNA) which is placed as close to the antenna as possible to minimise the signal loss. These amplify the signal by 27 dB and have a typical noise figure around 4.5. The signal is then split equally into a zero and 90° phase by a 90° hybrid coupler. These are each mixed with the second harmonic of the local oscillator signal via a second harmonic mixer. The advantage of using second harmonic mixers is the reduced requirements for the local oscillator and the local oscillator signal transmission lines. The resultant intermediate frequency (IF) is amplified by 40 dB and lowpass filtered before being digitised.

The mixers have some sensitivity to harmonics other than the second of the local oscillator. This sensitivity is very much reduced, but can be important if the signal in this frequency range is much higher than the signal of interest. Below is a table which details the response of the mixer to various harmonics.

Below is a list of the important components used and they are refered to by number in figure 4.2.

			RF	
		1	**2**	**3**
	1	-33 dB	-45 dB	-40 dB
LO	**2**	0 dB	-50 dB	-40 dB
	3	-30 dB	-45 dB	-50 dB

Table 4.1: Sensitivity of the mixers to different combinations of harmonics

1. LNAs: *Quinstar QLW-06404527*
2. Hybrid Couplers: *Krytar 3100400K*
3. Second Harmonic Mixers: *Miteq SBE0440LW1*
4. Wideband Power Amplifiers: *Mini-Circuits ZVA-213-S+*
5. Fixed Frequency DROs: *Miteq -XX-XXXXX-ST-R*
6. 16-1 SPDT switch: *P16T-0R5G18G-60-T-SFF*
7. 4-Way Power Splitters: *Krytar 7020180*
8. IF amplifiers: *Mini Circuits ZKL-1R5*
9. Digitiser: *4DSP FMC108*
10. FPGA: *Xilinx Virtex 6*
11. FPGA IO Board: *Xilinx ML605*

4.1.4 Installation on MAST

SAMI was installed on the MAST vessel looking through a 15 cm diameter window of fused silica, situated 20 cm above the midplane, between the two MAST Neutral beam Injectors (NBIs). Figure 4.3 shows the SAMI set up installed on the vessel, minus the antenna array for clarity. The heterodyne receiver is mounted on an angled bracket to the left of the window and is completely electrically insulated from the vessel. The cables that can be seen leaving the top of the photo mainly consist of the IF cables which carry the

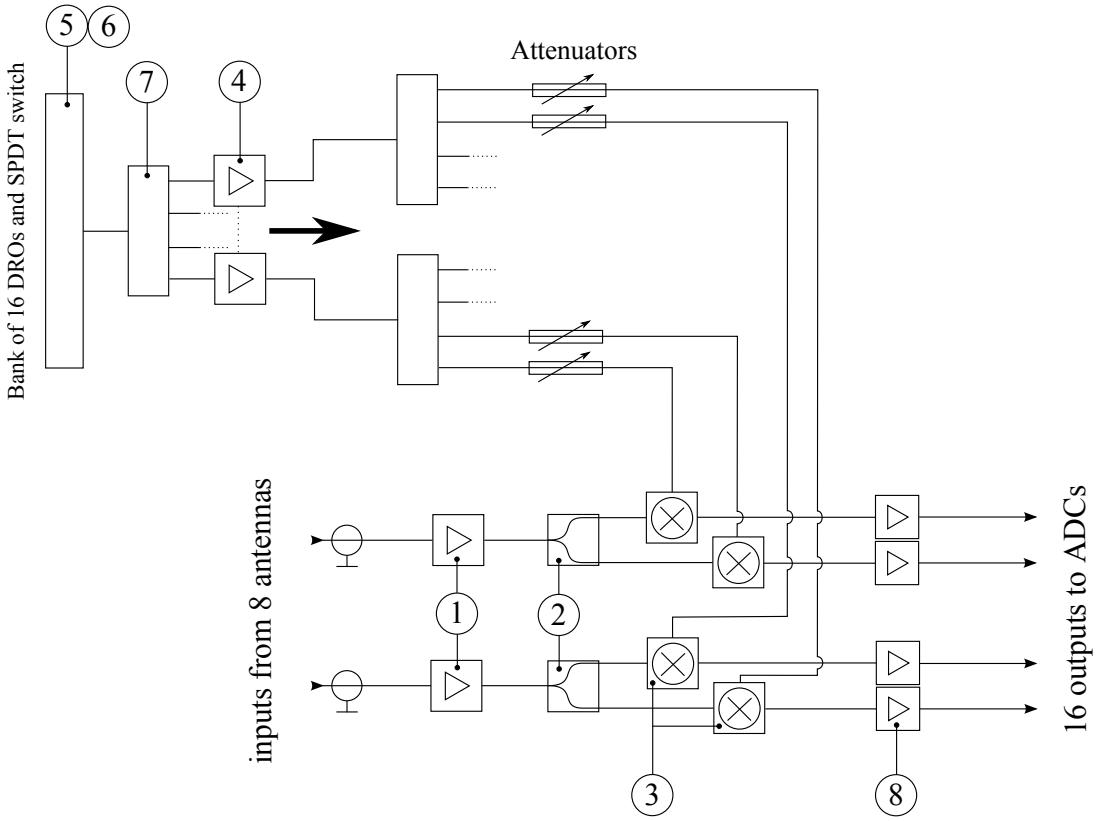

Figure 4.2: The schematic for the vector heterodyne frequency down-converter. The numbers refer to the components in the above list.

IF signals back to the digitiser which sits in a cubicle (out of shot). The local oscillator is also situated in the same cubicle as the digitiser, and the local oscillator signals are carried to the receiver via a high frequency armoured cable.

The antennas themselves are mounted into a polycarbonate plate which is designed so that it may be easily replaced. The reason for this is that we wanted to be able to easily change the array shape to allow flexibility in the array shape design. We could for instance design an array such that it is more sensitive to particular parameters, such as magnetic field pitch, or to have minimal sidelobe oscillations to obtain a clearer picture of the emission pattern.

The antennas could be mounted onto the plates in two polarisations, to allow us to observe emission of both polarisation components. The mounts attached to the array mounting

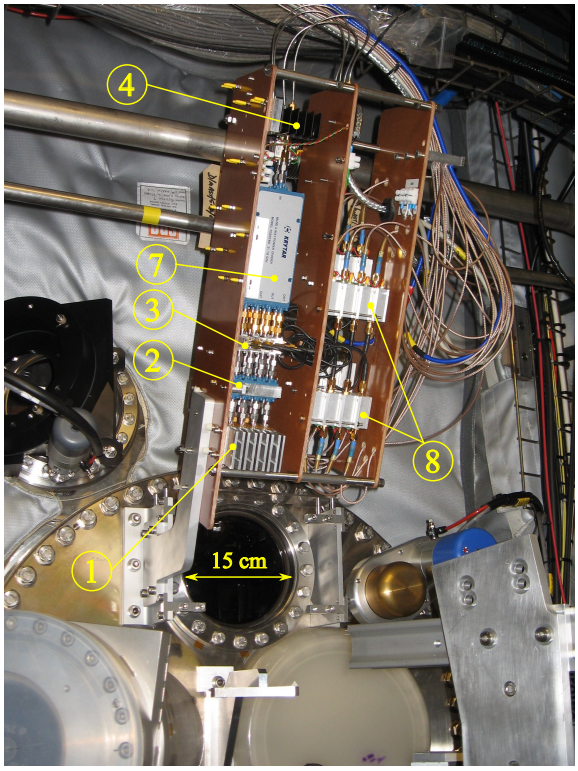

Figure 4.3: The heterodyne receiver mounted on the MAST vessel. The antenna array plate (not shown) sits just behind the 15 cm diameter port in sector 7. This port sits 20 cm above the midplane.

plate through holes designed with flats to keep the antennas either vertical or horizontal. Figure 4.5 shows the antenna holder, which slots into the array mounting plate, in both its positions.

4.2 Antenna design

4.2.1 Vivaldi antipodal antennas

The antennas need to be very broadband, operational in the range from 10 - 40 GHz, small enough so that we may fit at least 16 into a 15 cm diameter port window and have a wide enough beam to cover the whole plasma surface. Some of these requirements were met by

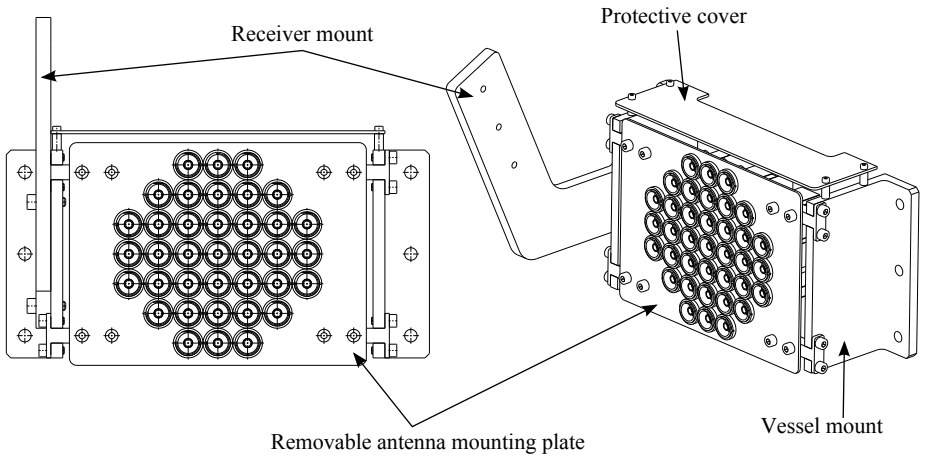

Figure 4.4: The antennas were mounted onto the vessel via a removable array plate. The object was to be able to easily interchange array shapes allowing for improvements in design.

a quad ridged horn antenna made by Flann Microwave, but only 3 of these antennas could be accommodated in the small port. The Flann DP421-B antennas formed part of our pilot experiment described in section 5. Eventually a cheap printed circuit board design known as an antipodal Vivaldi antenna described in this thesis [65] and this paper [66] satisfied all our requirements.

This design consists of an etched conducting layer either side of a substrate of low dielectric constant, RT/Duroid 5880. A thickness of 0.381 mm was used with a 35 micron layer of copper. The shape of the copper layers, detailed in figure 4.7, has an exponentially tapered flare opening of the form $y = c_1 e^{Tx} + c_2$. One side then has a linear transition to a 50 Ohm microstrip of width W_{ms} and connects to a k* connector, the other side opens out into a ground plate. Table 4.2 details the parameters chosen for the final design.

The antipodal design was trialled against a notched Vivaldi antenna shown in figure 4.6. The notched type antenna was found to be less broadband and have resonant structures in its response with frequency. The Antipodal type however was flat within 2 dB accross the measurable range (up to 26.5 GHz). On this basis the antipodal type was selected.

The beam pattern for the antipodal type antennas was measured at the university of Strath-

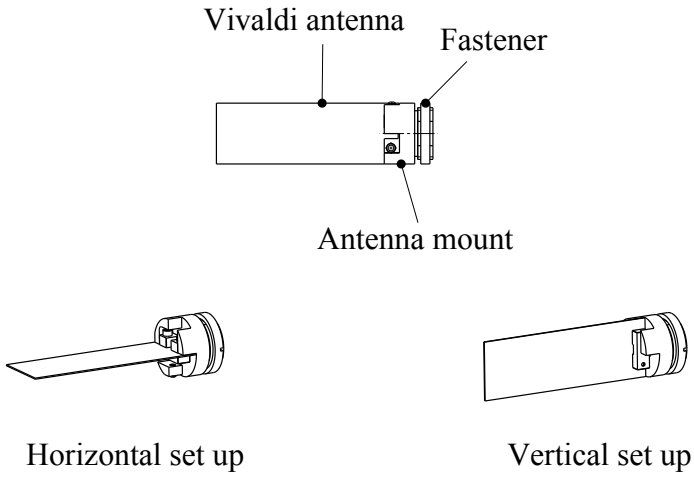

Figure 4.5: The specially designed antenna mount could hold antennas in one of two polarisations and attached to the array plate via a special nut.

clyde using their scalar network analyser. The antennas' scattering parameters, the parameters which tell us how much of the signal leaks from one antenna to another, was also measured. The method and results from these experiments are presented in section 5.2.

4.3 Designing an aperture synthesis array

Any phased array system will generate unwanted artefacts in an image due to the fact that an array can measure only a discrete number of points in $\{u, v\}$ space. Thus oscillations that would have been cancelled by other nearby points in $\{u, v\}$ remain in the reconstructed image. This is like multiplying the Fourier space with a sharply peaked gridding function resulting in oscillations in real space known as grating or sidelobes.

A central motivation for array design is to choose the antenna locations such that these spurious sidelobes are minimal in the reconstructed image. In order to quantify this it is instructive to consider the array's response to a point source. The response of an array to a point source at $\xi = \eta = 0$ is given by the so called equivalent array factor, AF_{eq} by analogy with the phased array [67]:

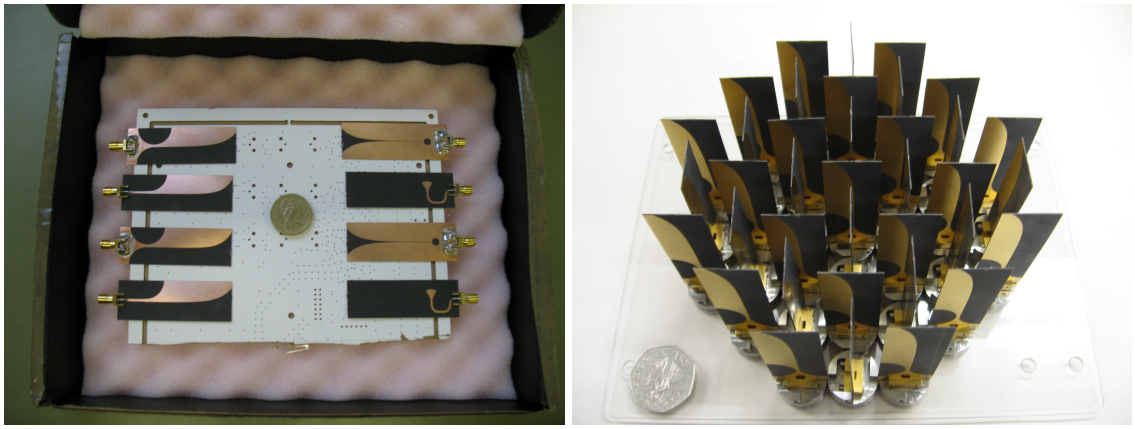

Figure 4.6: **Left**: Two types of Vivaldi antenna, the antipodal (left) and the notched (right). The antipodal antenna had a much greater operational frequency range and flatness. **Right**: An arrangement of 37 antipodal Vivaldi antennas held by metal holders attached to a polycarbonate plate. The plate determines the shape of the array and may be easily changed.

$$AF_{\text{eq}} = \text{Re}\left\{\sum_{l=1}^{n_b} e^{i2\pi(u_l\xi+v_l\eta)}\right\} \tag{4.4}$$

$$= \frac{1}{2}\sum_{m=1}^{n}\left(e^{ik(x_m\xi+z_m\eta)}e^{-ik(x_m\xi+z_m\eta)}\right) - \frac{n}{2}, \tag{4.5}$$

where n_b is the number of baselines and k is the wave number. Expression (4.5) is more efficient to calculate than (4.4) since it involves only a sum over the number of antennas, n. It also reveals the connection between the traditional phased array and the aperture synthesis techniques.

To characterise the oscillations in the image quantitatively, combined with the beam pattern limiting the field of view it is useful to define the modified beam efficiency function as in equation 4.6. The Main Beam Efficiency (MBE), ϵ, defined in [67], where we have multiplied the equivalent array factor by the antenna gain pattern.

$$\epsilon = \frac{\iint\limits_{\text{mainlobe}} G(\xi,\eta)\,|AF_{\text{eq}}(\xi,\eta)\,|d\xi d\eta}{\iint\limits_{4\pi} G(\xi,\eta)\,|AF_{\text{eq}}(\xi,\eta)\,|d\xi d\eta}, \tag{4.6}$$

where we have included the magnitude signs as AF_{eq} may be negative. Finding the max-

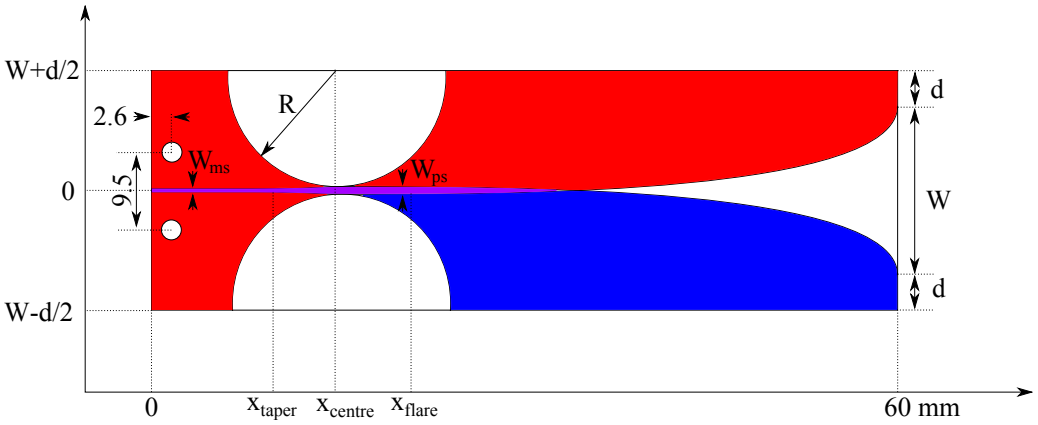

Figure 4.7: The antipodal Vivaldi antenna parameters. The different colors represent different sides of the PCB. The blue side consists of a microstrip tapering out to a wider parallel strip. It then has an exponential flare out to a point defined by d at the end of the antenna. The red side has the same exponential flare but lacks the strip feeds and has a ground plate instead.

Design Parameter	**value [mm]**
micro-strip line conductor width W_{ms}	1.14
Linear taper beginning X_{taper}	12.0
Parallel strip-line conductor width W_{ps}	1.46
Linear taper end and semicircle centre X_{Rcentre}	15.0
Semicircle radius R	9.27
Beginning of flare opening x_{flare}	17.0
Flare opening parameter T [mm^{-1}]	0.157
Constant c_1	$6.275 \cdot 10^{-4}$
Constant c_2	-0.739
Slot width W	14.0
Edge metallisation width D	3.5

Table 4.2: The design parameters for the antipodal Vivaldi antennas used in SAMI

imum of equation (4.6) is like minimising the side lobe oscillations and is equivalent to maximising the power carried in the main lobe in a traditional phased array. It also contains many local maxima which simple optimisation algorithms will find it hard to avoid. We thus require a good global optimisation scheme.

SAMI has the ability to switch between groups of antennas using sub-microsecond two to one switches, similar, but more broadband than the switch which controls the local oscillator. The idea behind these switches is that provided the source does not move in between switching, we may effectively double the coverage of Fourier space and enhance the image quality, without the expense of new receiving channels. It was thus necessary to have an optimisation scheme which could also optimise two groups of antennas simultaneously, looking at the MBE of the combined system.

4.3.1 Antenna placement optimisation strategy

Simulated annealing (SA) is a global optimisation algorithm based on the analogy of annealing in metallurgy. In this algorithm the function to be maximised is randomly perturbed and an uphill step is always accepted as a new best solution. Further, in order to prevent the algorithm being caught in a local maximum, a downhill step is accepted according to some probability P which is in turn dependant on the so called temperature parameter T as in equation (4.7).

$$P = e^{(\epsilon_{current} - \epsilon_{new})/T} \tag{4.7}$$

The temperature parameter is lowered slowly and incrementally until either the process reaches some predefined $T_{\min}$ or it goes through a number of iterations without accepting a new solution. The process is then said to have frozen. Here the antenna positions are randomly perturbed, which in turn leads to a new value of AF_{eq}, which leads to a new value of ϵ. This is compared to the previous value and accepted or rejected according to these conditions. The difficulty with this type of algorithm is deciding on a suitable

cooling schedule and perturbation method.

Simulated annealing has been used in antenna placement optimisation by Cornwell [68], but the function optimised there was a function only of the distance between samples in Fourier space. In contrast the present work considers directly the effect of antenna placement in real space by calculating the total side lobe level.

Two schemes for placing the antennas were trialled: first having the antennas all lie on a square grid of spacing equal to the width of one antenna and secondly allowing the antennas to take on any place within the aperture provided they did not overlap each other. In the case of placement on the square grid, one antenna was chosen at random and moved one space in the x and or z direction according to a uniform random integer from -1 to 1. In the case of free placement of antennas, the antenna positions were perturbed one at a time by a distance given by a Gaussian random number of standard deviation dx, for both x and z. If the perturbation of the antenna took it outside the boundary, it was reflected back inside and if the perturbation caused it to clash with another antenna, another antenna was chosen at random and perturbed until a move which didn't cause a clash was found.

When optimising two groups of antennas simultaneously, the highest values of ϵ were often found when the antennas of each group were closest to those in the same group. Early optimisations got stuck in local maxima due to the size of the antennas preventing this clustering from occurring. Often an antenna would get stuck the other side of the other group and it was too expensive in terms of ϵ for that antenna to join its group, since this either meant breaking up the intervening group or the sole antenna moving around the intervening group. To prevent this, a random antenna from group 1 was swapped with another from group 2 every 10 iterations and this move would be accepted according to the same conditions as a normal perturbation. This step significantly improved the convergence speed.

When the optimisation was first carried out the area defining the main lobe was allowed to be defined by the current array configuration. This led to the algorithm attempting to get all the antennas as close as possible to each other to maximise the area of the main

lobe integral even at the expense of increased side lobes. In order to prevent this, the area of the main lobe integral was fixed at half the achievable angular resolution so that the only way in which the algorithm might maximise ϵ was to minimise the side lobes in the surrounding region.

4.3.2 Results for 2 cm antennas

The first optimisation was for eight antennas on a regular square grid to try and keep processor time down and to force the Fourier samples onto a regular grid. The result can be seen in Figures 4.8 - 4.10. The MBE for this configuration is 18.5% and the AF_{eq} contains significant oscillations.

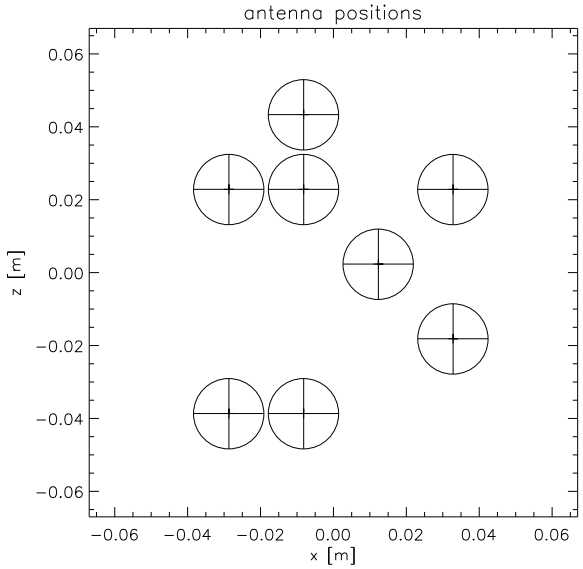

Figure 4.8: The optimal antenna placement found by the SA algorithm for 8 antennas at 20 GHz on a square grid. 23 of the 28 possible Fourier samples are repeated. The antennas here are denoted by circles of the size of the exclusion zone which other antennas must not be inside.

Next the condition of a square grid was lifted to see if the MBE could be enhanced further by free placement of antennas. Initially we tried optimising 5 antennas to see if the algorithm produced something reasonable. The results can be seen in figure 4.11, where the antennas have adopted a pentagonal shape, forming concentric circles in Fourier space.

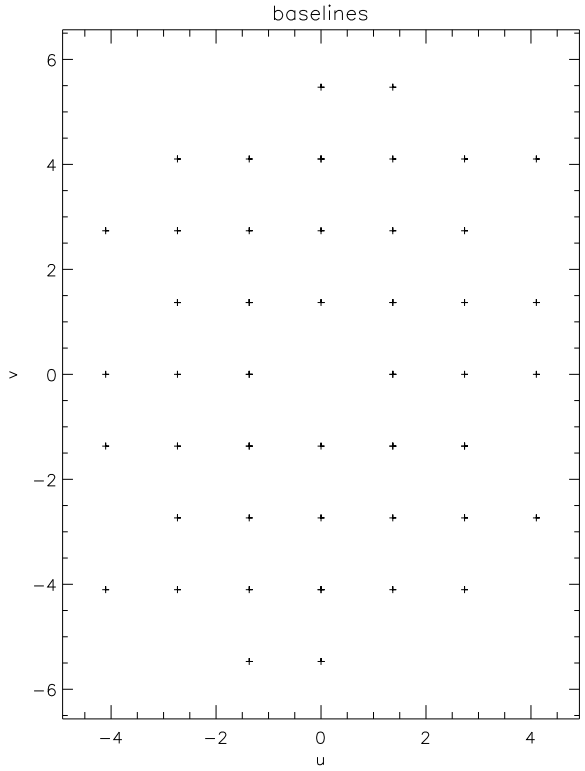

Figure 4.9: The corresponding samples in Fourier space for 8 antennas on a square grid shown in figure 4.8

The modified beam efficiency for the 8 antenna free placement configuration was 27.8%, a significant improvement on the grid system. We can see that the SA has chosen to arrange the antennas such that the samples in Fourier space lie in an elliptical envelope, even though this leads to a non circular central lobe which does not completely fill the main lobe area.

The cooling schedule used was the so called Cauchy cooling schedule $T = \frac{T_0}{m}$, where $m = 1, 2, 3...$ is the iteration number. It was found that this provided the fastest convergence spending more time refining reasonable estimates than the linear schedule. It was often possible to tell that improvements could be made on the solution by slower annealing as fast annealing often produced a rotation of the elliptical envelope in Fourier space or produced baselines very close to each other.

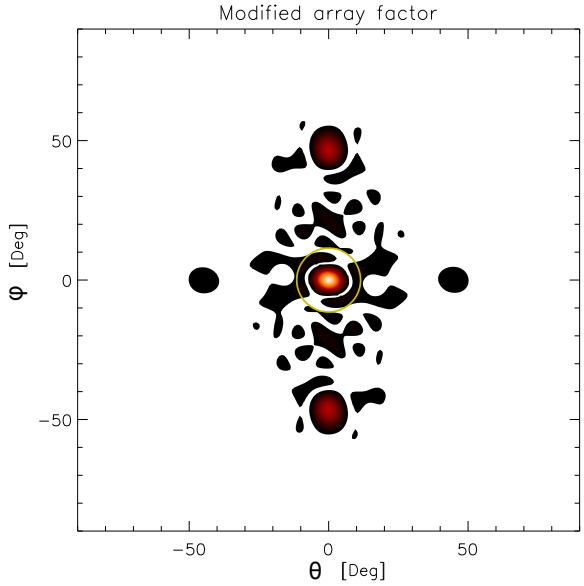

Figure 4.10: The modulus of the modified array factor AF_{eq} for the array of figure 4.8. The yellow ring denotes the main lobe integration area. The overall side lobe level is quite low, but this configuration suffers from the presence of grating lobes at the top and the bottom.

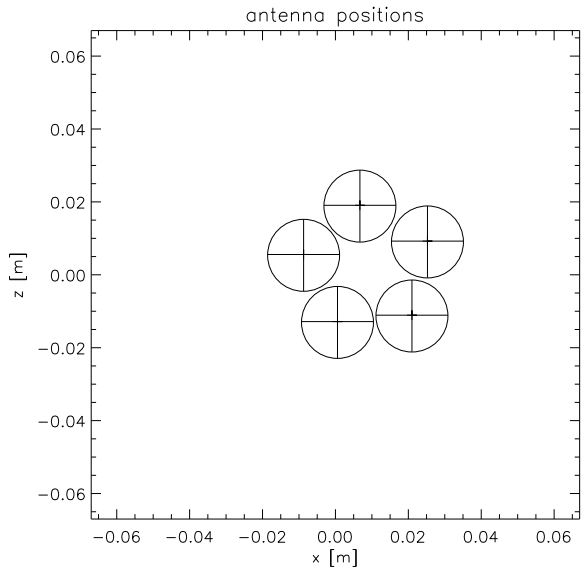

Figure 4.11: The optimal antenna placement for a 5 antenna system where the antennas are allowed to take any position within the aperture. The antennas make a pentagon.

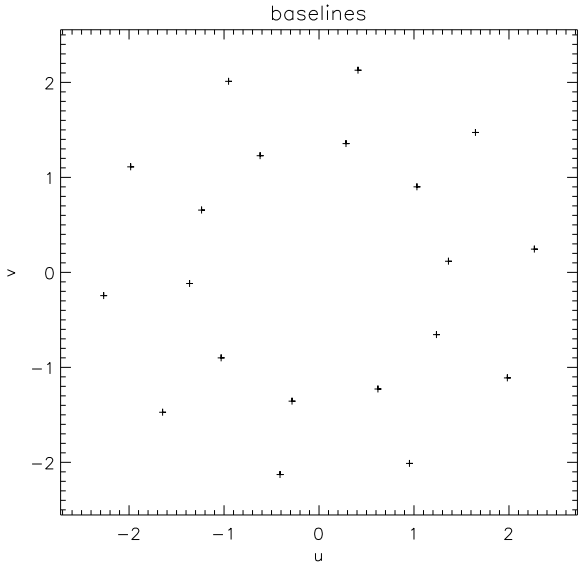

Figure 4.12: The sample positions in Fourier space corresponding to the antenna positions in figure 4.11. There is a clear circular structure present

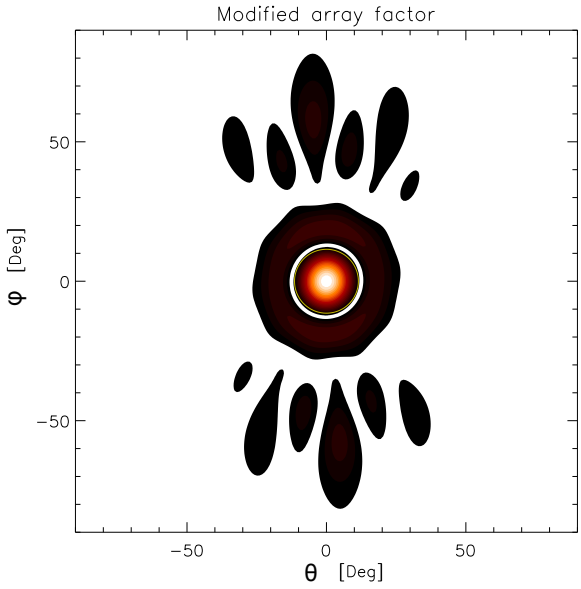

Figure 4.13: The Array factor multiplied with the antenna beam pattern. This configuration gave an MBE of 26.9%

Figures 4.17 - 4.19 give the results of the SA algorithm when optimising two groups simultaneously. Again we can see that the SA has arranged the antennas such that the baselines

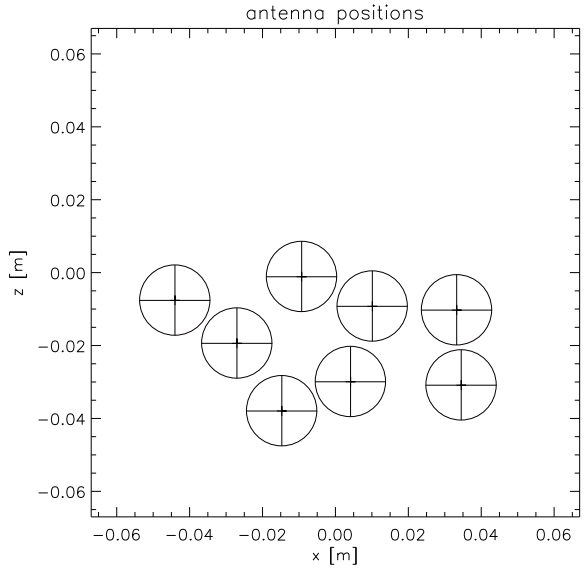

Figure 4.14: The optimal antenna placement found by the SA algorithm for 8 antennas with free placement.

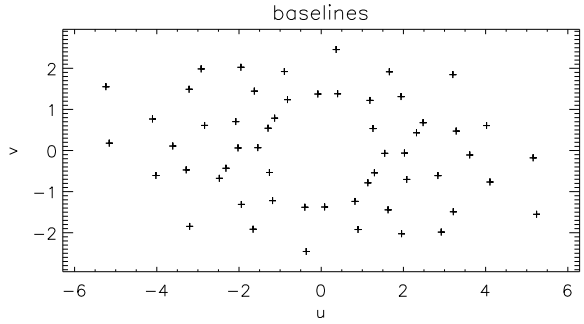

Figure 4.15: The samples in Fourier space for 8 antennas with free placement as shown in figure 4.14. The hole in the middle of this plot is present due to the antennas fixed size preventing these Fourier samples being formed.

lie in an elliptical envelope and remarkably the two groups have baselines which do not overlap each other. The MBE for this arrangement is 36.3%, again a marked improvement on the 8 antenna free placement configuration.

Also the antennas have grouped together since the shorter baselines contribute most highly to the beam efficiency. Adding longer baselines degrades the beam efficiency for a set number of antennas and so we are left with a trade off between beam quality and angular

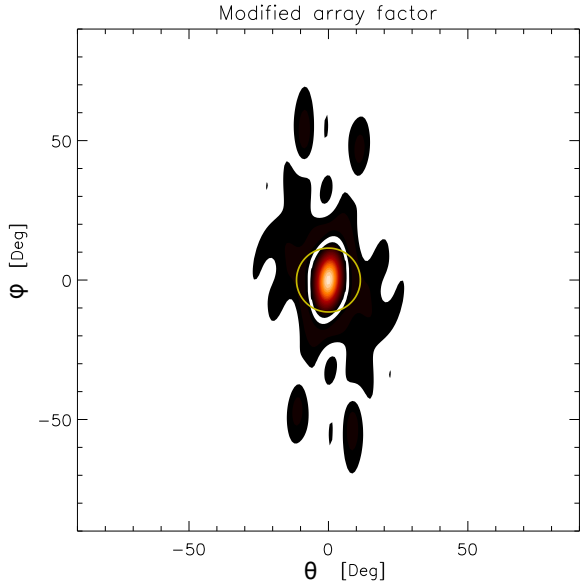

Figure 4.16: Same as Figure 4.10, but with the antenna position of figure 4.14. The grating lobes have now been removed leading to a higher MBE of 27.8%.

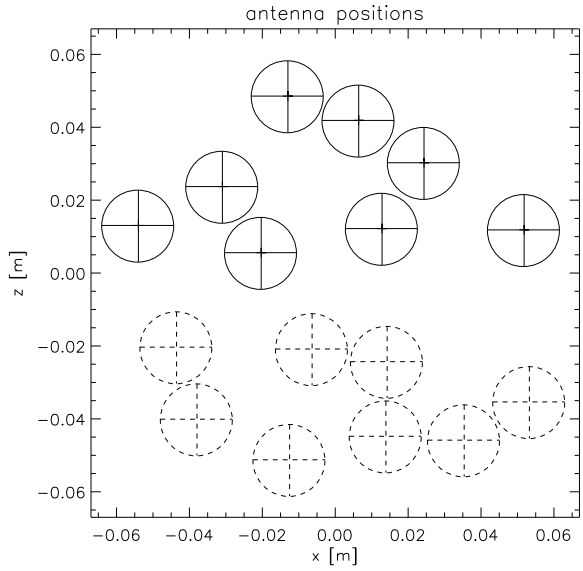

Figure 4.17: The optimal placement of two groups of 8 antennas found by the SA algorithm. solid lines - group 1, dashed lines - group 2.

resolution analogous to the interferometric uncertainty principle derived by Camps *et al* [67].

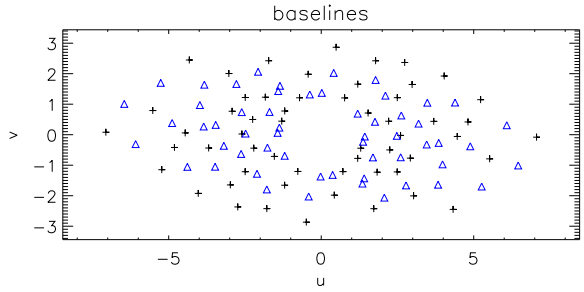

Figure 4.18: The corresponding baselines for two groups of 8 antennas as in Figure 4.17. crosses - group 1, triangles - group 2.

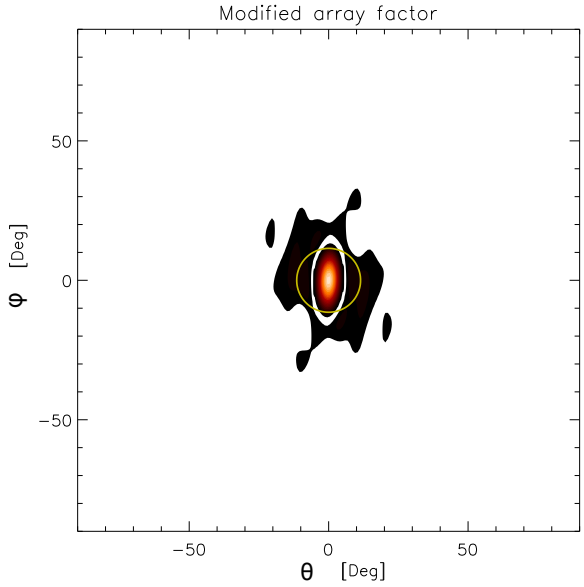

Figure 4.19: The modulus of the modified array factor AF_{eq} for the two groups in Figure 4.17. The MBE is 36.3%

4.3.3 Results for 1.5 cm antennas

Since the shorter baselines tended to produce a higher beam efficiency, an obvious extension to the problem was to make the physical size of the antennas smaller, to allow them to get closer together. The smallest practically achievable antennas for SAMI are 1.5 cm high. Figures 4.20 - 4.22 show the results for an eight 1.5 cm antennas. The beam efficiency found for these antennas is 40.6% compared to 27.8% for antennas of 2 cm. We can also see that the elliptical envelope in Fourier space no longer seems to be present.

Figures 4.23 - 4.25 show the results for optimising two groups of eight 1.5 cm antennas, the MBE for which is 44.0%. We also note the return of the elliptical envelope in Fourier Space. One may notice that, in each case, if there are baselines greater than 3 wavelengths present then this elliptical structure appears. If not, the optimal structure in Fourier space is more circular. It appears as though if the algorithm is required to have baselines greater than 3 wavelengths, either because the minimum antenna spacing forces it, or because there are many baselines to fit in, then it is beneficial to have the longer baselines in the direction of narrowest antenna beam pattern.

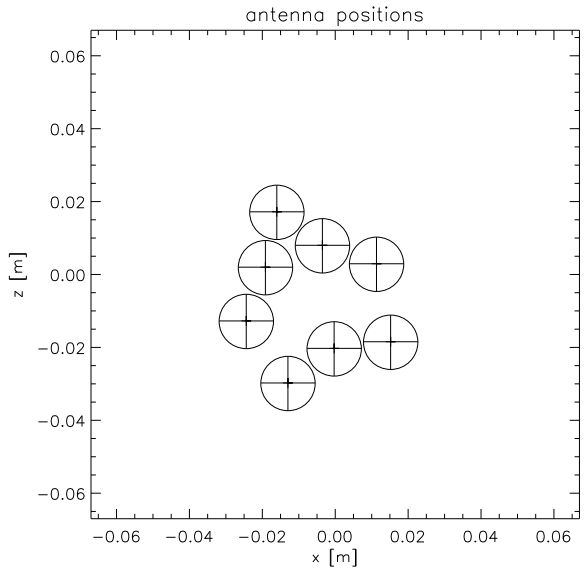

Figure 4.20: The optimal antenna placement found by the SA algorithm for 8 antennas of height 1.5 cm.

4.3.4 Conclusions for optimisation

A simulated annealing optimisation of a function designed to target unwanted oscillations in an image produced by the SAMI radiometer has been performed. Optimisation of this function for 8 antennas and for two groups of 8 antennas simultaneously, both for 2 cm antennas and 1.5 cm antennas, were carried out. The SA has provided reasonable approximations to optimal solutions of this modified beam efficiency function.

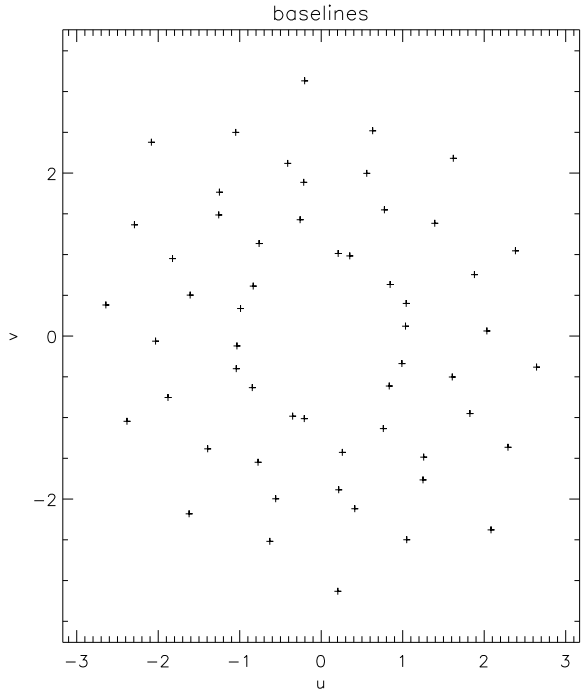

Figure 4.21: Fourier sample position for the antennas in Figure 4.20. We can see that the elliptical shape is not present.

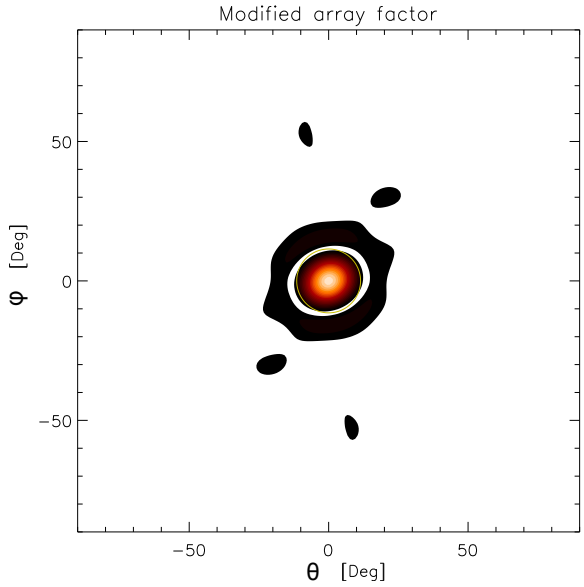

Figure 4.22: The modified AF_{eq} for the antenna placement in figure 4.20. The MBE here is 40.6%, which is a marked improvement on the 27.8% found for antennas of 2 cm height

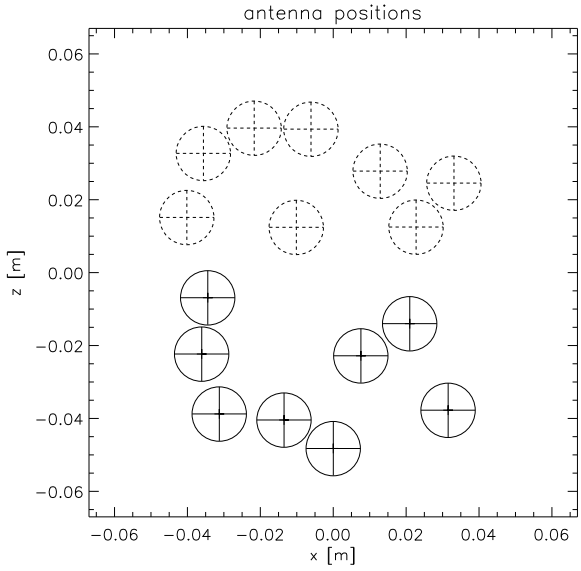

Figure 4.23: A re-run of the placement of 2 groups of 8 antennas this time for antennas 1.5 cm high.

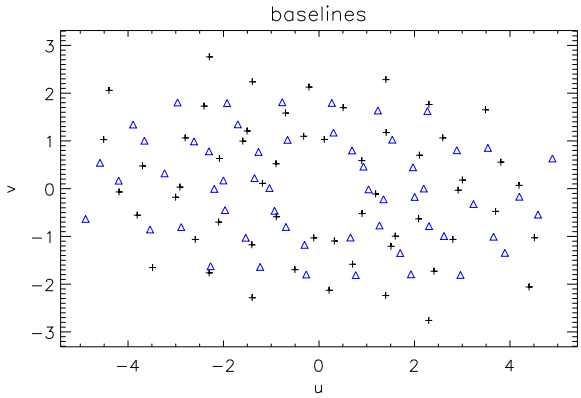

Figure 4.24: The sample positions here are beginning to show signs of going back to an elliptical pattern.

The solutions are arranged so that the corresponding samples in Fourier space have a fairly even coverage and additionally lie within ellipses if the baselines are forced to be greater than 3 wavelengths. These ellipses are a result of including the antenna gain pattern, shown in figure 4.26 in the beam efficiency function and allow higher frequency samples to exist in the narrower part of the antenna beam.

Unique solutions to this problem do not exist due to the hermitian symmetry in Fourier

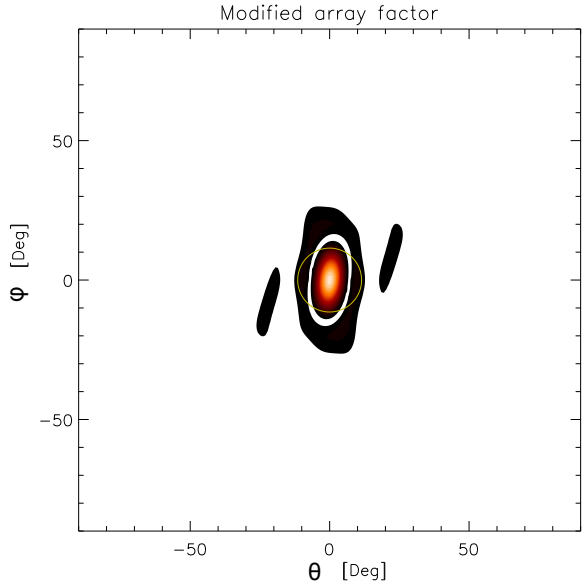

Figure 4.25: An MBE of 44.0% suggests as a result of having more baselines the algorithm is finding it hard to fit them in advantageous positions so far as the beam efficiency is concerned

space. It is also likely that many near optimal local maxima exist making the assessment of whether a truly global solution to the maximum of ϵ has been found difficult. Multiple runs were done for all cases, with different initial conditions and it was found that the MBE solution values always lay within ± 2 %. The same baseline features were also found in each run, giving some confidence in the method. However more work would be required to accurately asses the quality of the solutions found.

4.4 Data acquisition

4.4.1 FPGA controlled digitisation

A pilot experiment showed that we required 14 bit digitisation in order to reliably capture the range of signals from under the noise floor to the large spikes seen during the ELM bursts. Digitising this at a speed of 250 MHz was a demanding constraint and in order to keep the costs reasonable we decided to build our own Field Programmable Gate Array

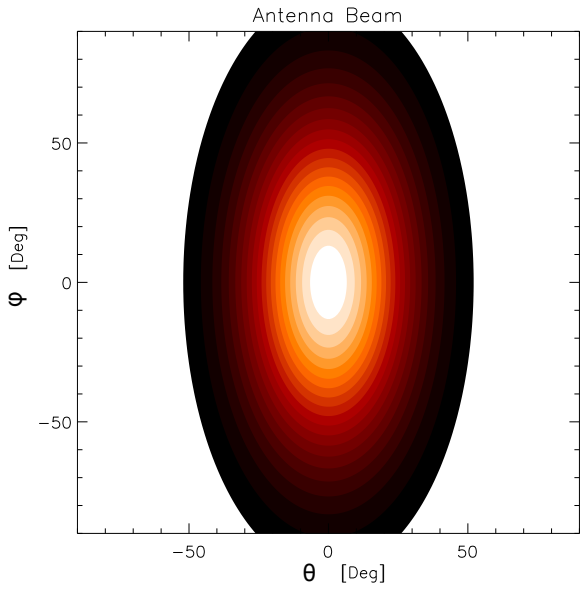

Figure 4.26: The main antenna beam for horizontally polarised antennas. The antenna beam is twice as wide in the E plane as in the H plane

(FPGA) controlled digitiser. The coarse workings of this system are detailed below but the details of the firmware are outside the scope of this thesis.

An FPGA is in essence a set of logic gates which can be "rewired" by software to act as any integrated circuit the user chooses. The complexity of current FPGAs allows part of the device to be configured to act as a processor, allowing it to run operating systems in a similar way to a computer. The FPGA brings many advantages, it is capable of doing real-time signal processing as if it were a bespoke digital circuit, what's more is that the function of its circuitry can be changed with a simple firmware upgrade and sidesteps the need for a construction of a new circuit. This brings a unique flexibility and indeed portability, since you interface with the FPGA in a standardised way, yet it may perform a large variety of tasks. There is a significantly lower hardware cost in an FPGA controlled digitiser solution than in a traditional digitiser of the same specifications, making it the ideal candidate for this project.

The FPGA not only controls the digitisers and is responsible for downloading the data and sending it over the network to a PC, but it also controls the fast switch that is connected

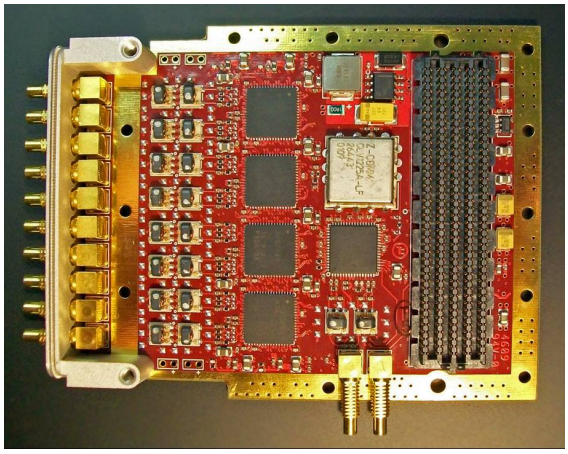

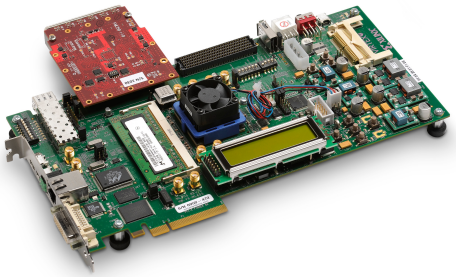

Figure 4.27: **Left**: One of the two 4DSP FMC108 digitisers used to digitise the 16 real and imaginary signals provided by the heterodyne receiver. **Right**: The Xilinx ML605 board with the 4DSP FMC108 ADC board attached. The Vertex 6 FPGA sits under the small fan in the centre.

to the local oscillator bank and generates the IF frequencies for the active probing signal for the active Doppler backscattering part of the diagnostic, which is not described in this thesis.

Chapter 5

SAMI calibration and proof of principle

5.1 Three antenna pilot experiment

Before building a full eight antenna system it was necessary to build a prototype experiment to demonstrate the principle of interferometric imaging and to inform the specifications of the final system. We were looking to finalise the digitiser speed and bit depth, as well as learn as much as we could about the behaviour of the system in a real experimental environment. To this end we constructed a three antenna system from three quad ridged dual polarisation horn antennas (Flann DP421-B), which are operational from 6 to 50 GHz. This system could only observe a single frequency at a time since the local oscillator used was a manually switched; it was borrowed from the JET ECRH group. The digitisation was done using three dual channel Agilent U2723 modular oscilloscopes.

This prototype system was installed on the MAST vessel and took data for several days. In this time we were unable to perform any imaging due to the fact that three antennas only have enough information to form the simplest images, more akin to tracking the position of a single source. Also, the fact that the digitisers ran on separate clocks, despite the published specifications, proved critical for the phase sensitivity of the system. The timing between the antenna signals was not sufficiently synchronised and there was a constantly-changing phase difference between each antenna.

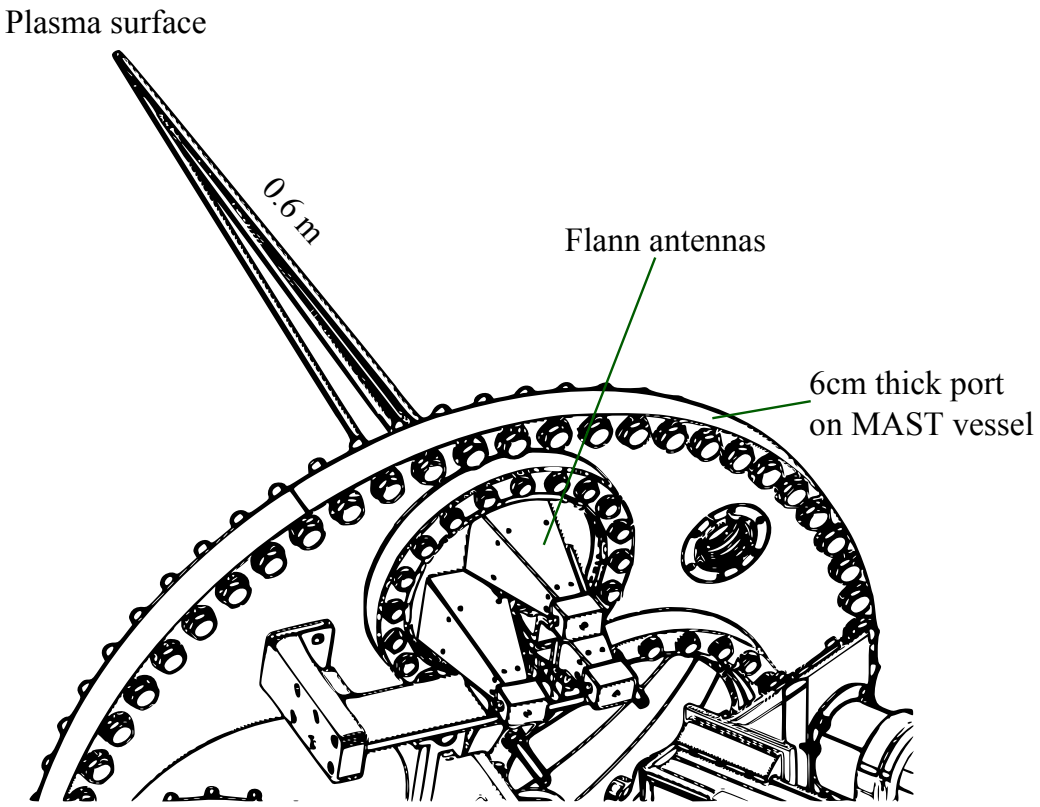

Figure 5.1: The pilot experiment was 3 antennas installed on the MAST vessel. This picture shows the three antennas mounted on the vessel port in sector seven. The rods here indicate where the antenna beams were centred, designed to be coincident at the plasma surface.

We were, however, able to get a great deal of useful information from the pilot experiment. The first thing we learned was the importance of sideband separation to the phase sensitivity of the device. Figure 5.2 shows the cross-correlation between the real and imaginary parts of each antenna signal from the plasma as a function of time lag and time. The signals have been filtered between 20 and 21 MHz. Referring back to section 3.2.5, we may recall that the cross correlation as a function of time is an oscillating component with an exponentially decreasing envelope. We should expect, then, to see an oscillating pattern as a function of time lag, and no change as a function of time, since the real and imaginary components must remain at 90° to each other. However this is clearly not the case for the left hand figure, showing some random drifts of the correlations in time. These

drifts correspond to a continually changing phase difference between the real and imaginary components, which is not acceptable. The right hand figure is the same quantity, for the same data, after the sideband separation procedure described in Section 4.1.1. We can see that these phase drifts were caused by interference between the upper and lower sidebands.

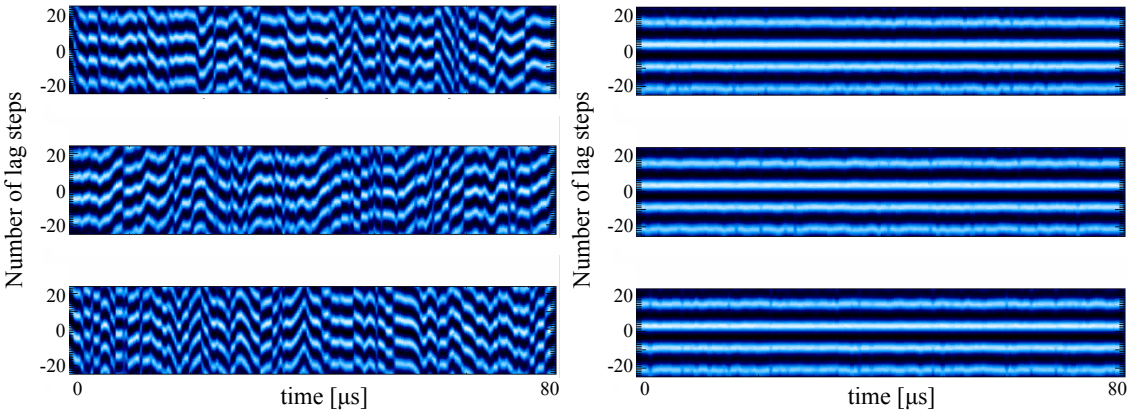

Figure 5.2: **Left**: The cross correlation as a function of time and time lag of the I and Q components. Antenna one at the top and antenna three at the bottom The bandwidth is 1MHz. As the I and Q components are always 90° apart, one would expect this graph to be a series of straight lines with time. Instead the lines drift randomly. **Right**: The same data, but for sideband separated I and Q. We can see that the random drifts with time have been removed and the I and Q components for a single sideband now remain 90° from each other.

The left hand side of Figure 5.3 show a spectrogram of the period when the reflectometer signal sweeps past our frequency channel. The reflectometer is another microwave diagnostic which directs its relatively high power signals towards the plasma density cut-off. It sweeps its frequency in a sawtooth like fashion in three frequency bands, starting from 17.6 GHz and ending at 59.7 GHz. In the figure, we see the frequency appear to start high and then fall to zero and continue reflected in the axis. The reflectometer sweep is in fact monotonic and the first, descending part, is when the reflectometer signal is in the lower sideband of our receiver and hence the frequencies are negative, but seen as high positive when only examining a single channel. The right hand side of Figure 5.3, shows the cross-correlation of I and Q components, this time unfiltered. We can see the width of

the characteristic bars increase as the signal frequency decreases, as we would expect from equation 3.26 and the phase between I and Q flips when the reflectometer signal passes the local oscillator signal, as expected from equation 4.2.

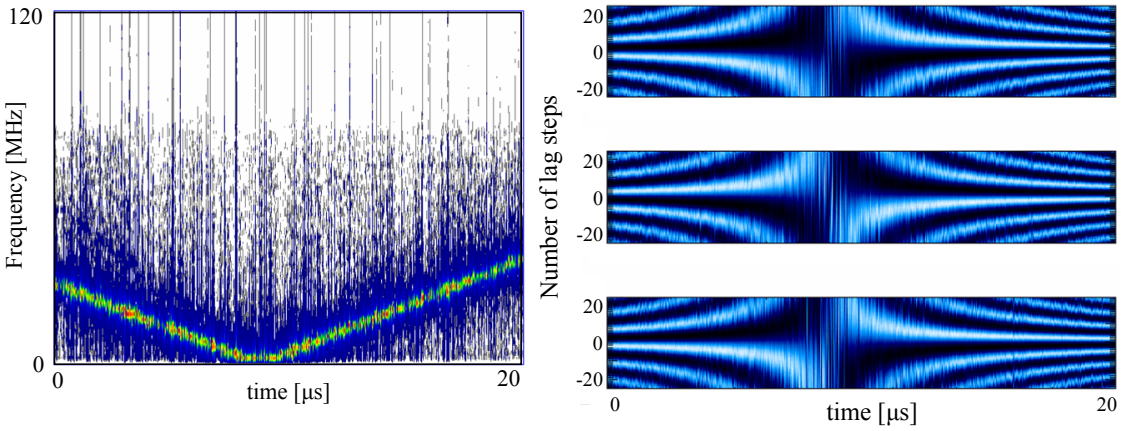

Figure 5.3: **Left**: A spectrogram for a period when the reflectometer is sweeping up through the band of our receiver. Although the reflectometer is sweeping only upwards in frequency during this period, we perceive a decline in frequency to zero and then a rise in frequency. This is because in the baseband the frequencies below the local oscillator are negative. **Right**: The cross correlation for I and Q as in Figure 5.2, unfiltered, and as the reflectometer passes through our frequency band. We may note the change in width of the horizontal bars and the eventual reversal of phase as reflectometer crosses the local oscillator frequency.

We were, also, able to see how the signal power varied with time. Figure 5.4 shows the power received at one antenna from the thermal plasma emission, compared with the D_α signal in the same time period. One can see that the D_α signal drops at 0.267 seconds, this corresponds to the transition from L mode to H mode. At this time, the signal from the antenna rises significantly. This is characteristic of observations of mode converted emission, as the density gradient rise in the mode conversion region, the tunnelling process becomes more efficient, leading to a higher observed power. The large spikes in D_α signal during the H mode period correspond to ELM events. We can see that we also receive large spikes in power at the antenna, the origin for which is as yet unknown. They are observed on many other machines [69, 70, 71] and it is conjectured that the sharp rise in emission during these events may be due to the production of supra-thermal electrons

during the ELM burst.

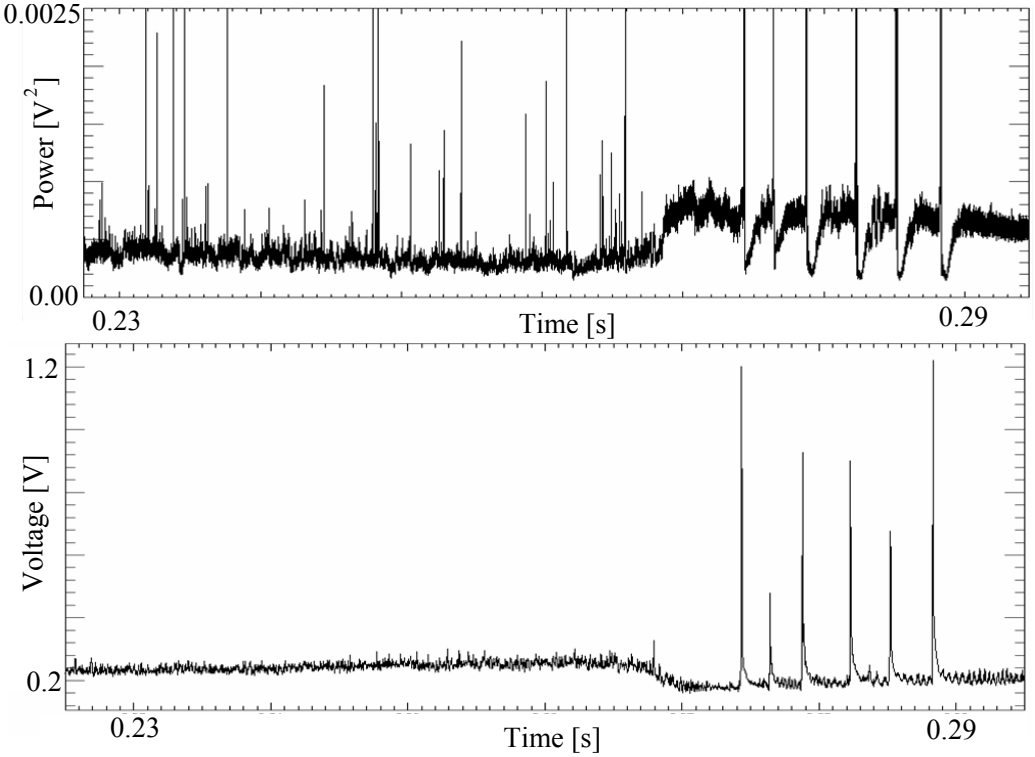

Figure 5.4: **Top**: The power trace for one of the antennas during the pilot experiment. **Bottom**: The D_α trace for the same time period as the above power trace. The drop in D_α signal at 0.267 seconds corresponds to a transition from L mode to H mode. Coincident with this is an increase in signal power at the antenna. The spikes in the D_α signal in the H mode period are ELM instabilities. We can see that the signal at the antenna collapses just after the ELM and rebuilds for the next one.

One may also notice that the antenna power collapses after the ELM burst, rapidly rebuilding before the next event. This again is due to the changing density gradient after the ELM event. This is consistent with recent observations of the pedestal pressure gradient, which suggests that the pressure gradient rapidly builds then remains constant for some time until the crash. The ELM crash in this instance is caused by the stability boundary moving due to the increasing pedestal width [72, 73].

After the pilot experiment was completed, the equipment was removed from the MAST vessel and the ADC timing errors were fixed a proof of principle experiment was con-

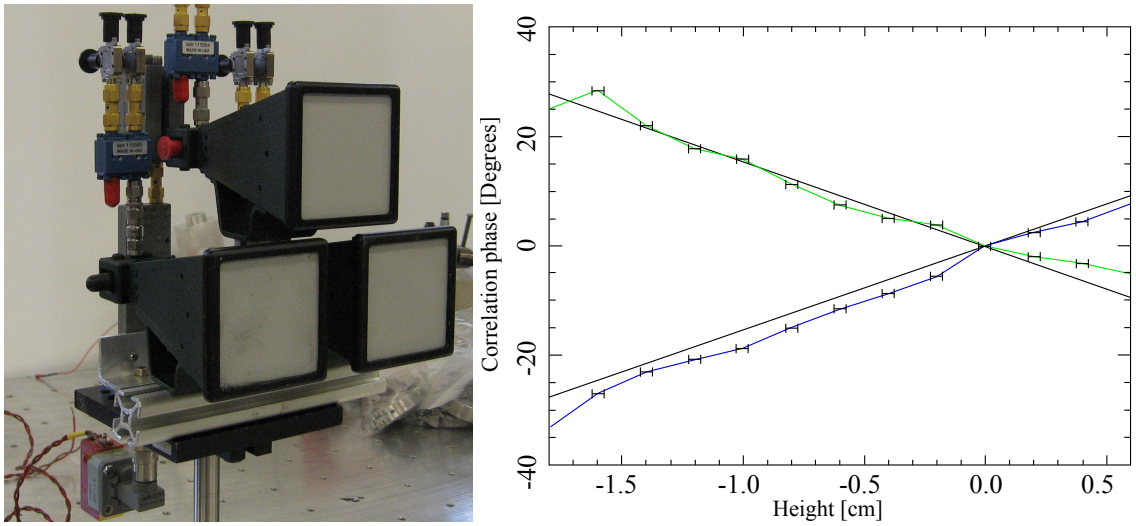

Figure 5.5: The predicted vs. measured correlation phase for the 3 antenna system. The phase agrees well with the predicted values within the experimental error. The small downward shift of the lower phase (blue), is due to the fact that the calibration was performed on an outlier (where the phases cross at zero)

ducted for the imaging. A 17.4 GHz Gunn diode oscillator connected to a Vivaldi antenna served as a source and was placed 81 cm from the array. The source was mounted on an adjustable mount which allowed us to raise or lower it in 2mm steps for a range of 2.5cm. Figure 5.5 shows the three antenna array and the measured vs predicted correlation phase. As can be seen, the correlation phase closely follows the predicted phase, with the majority of the scatter coming from the slight twist in the source antenna position during its movement.

These pilot experiments taught us about the digitiser requirements, requiring 14 bit digitisation in order to cover the largest spikes in emission and still have a sufficient number of bits to digitise the lowest amplitude signals. We also learned about the significance of digitiser synchronicity. We required that the digitisers did not drift by more than 10 picoseconds in 0.5 seconds, and learned that complicated parlance can obscure what the digitisers are actually capable of. This was one of the reasons which lead us to develop our own digitising system. Further, the effect of poorly separated sidebands was made very clear, causing the real and imaginary components to drift in phase making all measure-

ments of cross correlation phase impossible.

5.2 Measurement of antenna patterns and scattering parameters

Having designed the antennas ourselves it was necessary to characterise them. For this we performed experiments at the University of Strathclyde to take advantage of their scalar and vector network analysers. The important questions were:

- What is the flatness of the response with frequency?
- How broadband are the antennas?
- What is the antenna beam size / directivity?
- What are the antenna scattering parameters?

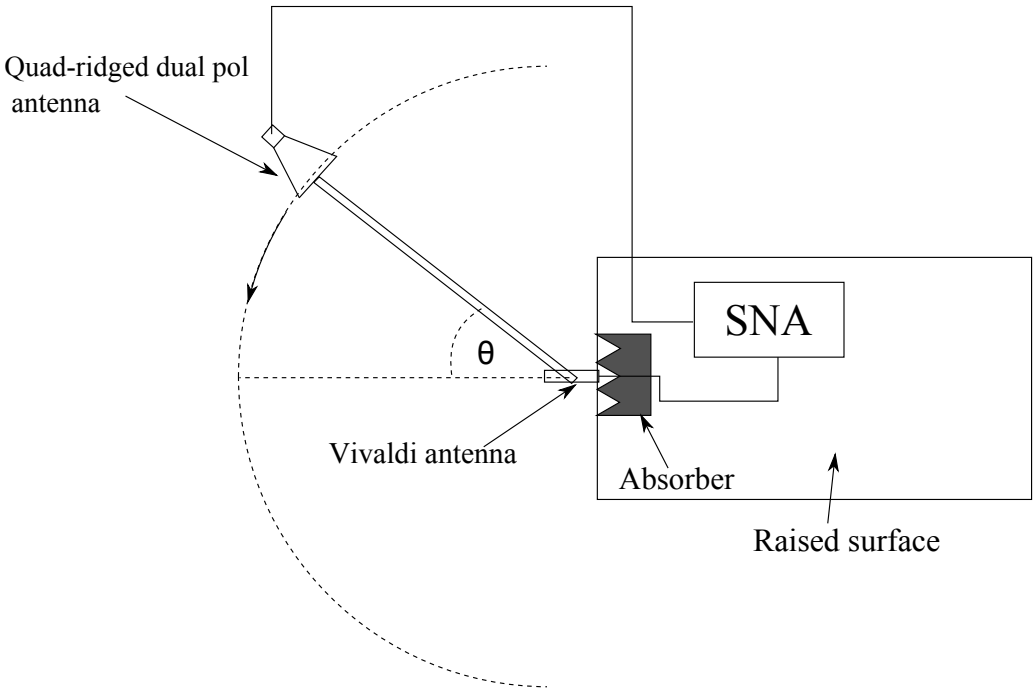

Figure 5.6: A schematic of the Scalar Network Analyser setup used to measure the beam patterns at Strathclyde university.

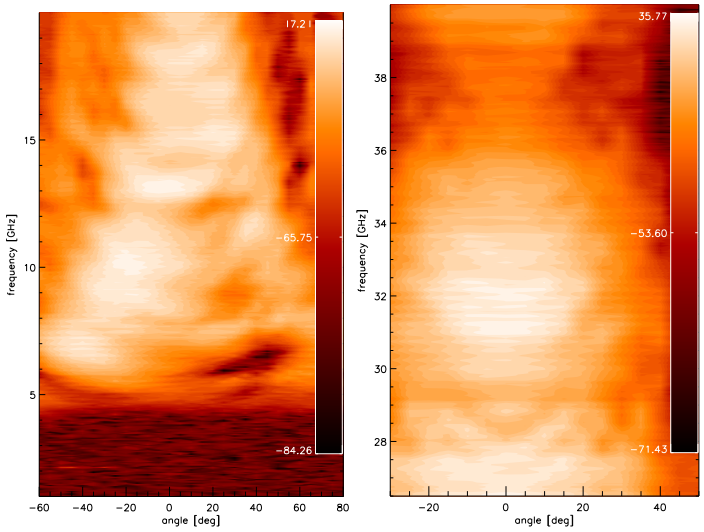

Figure 5.7: **Left**: The measured power *vs* angle and frequency for the E plane of the Vivaldi antenna (0 - 20 GHz). **Right**: Same as left but for 26 - 40 GHz. The low frequency cut-off is due to the quad-ridged antenna and not due to the Vivaldi antenna.

The beam pattern measurements were performed with the equipment outlined in figure 5.6. We connected a Scalar Network Analyser (SNA) to the Vivaldi antenna, which remained stationary at the centre of an arc traversed by a certified dual-polarised quad-ridged horn antenna, connected to the other end of the SNA. The SNA covered the range from 0 - 40 GHz, which had to be scanned in two segments: 0 - 20 GHz and 26.5 - 40 GHz, due to limitations in the transmission line. Figures 5.7 and 5.8 show the E and H plane beam patterns respectively. The E plane is the plane parallel to the antenna polarisation and the H plane is the plane perpendicular to the antenna polarisation. These figures show the beam patterns to be fairly wide and flat, with the H plane being at least twice as wide as the E plane. One may notice wave-like structures on the measured beam patterns which are a few dBm in power, these are a combination of the changes in the reflection parameter shown in Figure 5.9 and interference from reflected signals from objects around the room. Care was taken to minimise such reflections during the experiment using absorbing material, but nonetheless some remained at the level of 2-3dB. These beam pattern measurements are used in a qualitative sense to inform us of how the beam pattern behaves with frequency.

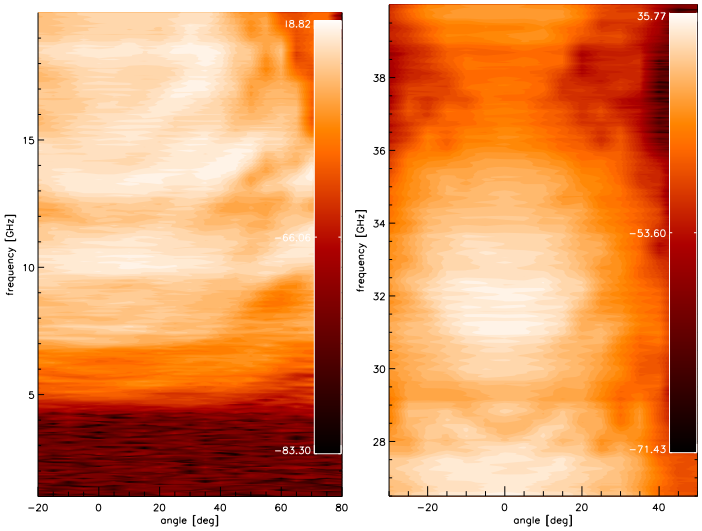

Figure 5.8: **Left**: The measured power vs angle and frequency for the H plane of the Vivaldi antenna (0 - 20 GHz). **Right**: Same as left but for 26 - 40 GHz

Another important measurement was the antenna scattering parameters S_{ij}. These are complex coefficients which describe how much incoming/outgoing signal is reflected and how much signal from one antenna leaks onto another. S_{ii} is the reflection coefficient for antenna i and S_{12}, S_{21} are the coefficients for the voltage received at antenna 1 from 2 and vice versa.

Figure 5.9 presents the measurements for the closest possible antenna spacing as this is where the antenna cross talk is likely to be highest. Note that the magnitude of the parameters S_{12} and S_{21} are below -20dB for all frequencies above 10 GHz. This implies that the antenna cross talk is very low even for short spacings. However, this number may rise in the presence of a semi-reflective port window. The parameters S_{11} and S_{22} are below -8dB between 10 and 27 GHz, with a small rise at higher frequencies. This implies a 16% reflection in the lower range, but when the operational frequencies of SAMI are considered (the green dashed lines in figure 5.9), in practice the reflection in the lower range is everywhere below -10dB for all channels apart from the last two.

These antennas are very broadband, having an acceptable reflection coefficient over our frequency range, especially when the precise frequency of our channels are taken into ac-

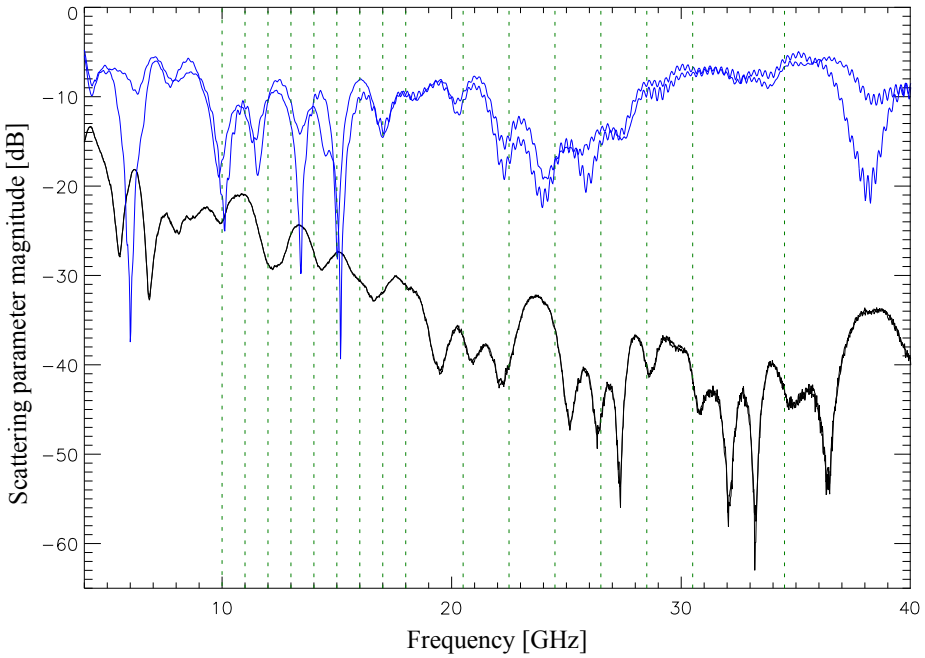

Figure 5.9: The magnitude in dB of the scattering parameters for two Vivaldi antennas at the closest possible spacing. Black: S_{21} and S_{12}, which are nearly coincident, blue: S_{11} and S_{22}. The green dashed lines are the operating frequencies of SAMI

count. They have low cross-talk parameters (S_{12}), below -20dB even at minimum spacing being, for all frequencies. They also have wide, although asymmetric beam patterns making them a good choice for a wide field imaging array. Finally they are small enough that many may be accommodated in our small port window.

5.3 Calibration

Calibration is an essential part of any new diagnostic. The sensitivity of SAMI to small changes, such as the torque applied to the k* connectors at the antennas, made accurate calibration essential. Many methods of calibration were trialled and at each stage we learned something valuable about the behaviour of both SAMI and our calibration equipment. In this section, however, I will present only the calibration experiments which produced the most reliable and best understood data, and which formed the final calibration which was

used in the later plasma results.

The final calibration was done in three stages. Two rounds of "off vessel" calibrations and one "on-vessel" calibration. The off vessel calibrations involved turning the array to face outward from the MAST vessel and used an independent source to illuminate the array. The through vessel calibration was done by pointing a noise-like source through port windows at various locations around the vessel. The noise-like source was used in an attempt to reduce as much as possible the result of coherent interference from reflected signals within the vessel.

5.3.1 Off vessel calibration

In order to calibrate SAMI, it was necessary to get detailed information about signals received by SAMI in a controlled environment, where the source was known precisely. However, it was found that the calibration values varied if the array was removed from the vessel, as this involved detaching the antennas from the receiver. As we are using coaxial transmission between the antennas and the receiver the torque of the connection proved a critical parameter to the measured phase. It was necessary, then, to make a controlled environment near the vessel in order to calibrate SAMI. We turned the array to face outward from the vessel and secured it so it was horizontal within a degree. We covered the surrounding area in microwave absorbing material to minimise reflections, creating an ad-hoc anechoic chamber: see figure 5.11 for a schematic. The antenna configuration used in these calibration experiments and the large majority of the MAST campaign is the 8 antenna free placement array found by the SA algorithm and is shown again here in figure 5.10

As a source, the first round of off-vessel calibration experiments utilised a Rohde and Schwartz SNA, which swept from 10 - 18 GHz, in conjunction with the Flann DP421-B antenna. To cover the higher frequency range we used a second harmonic mixer as a frequency doubler to generate the a second harmonic signal, the fundamental being strongly suppressed by similar second harmonic mixers in the receiver. This suppression was found

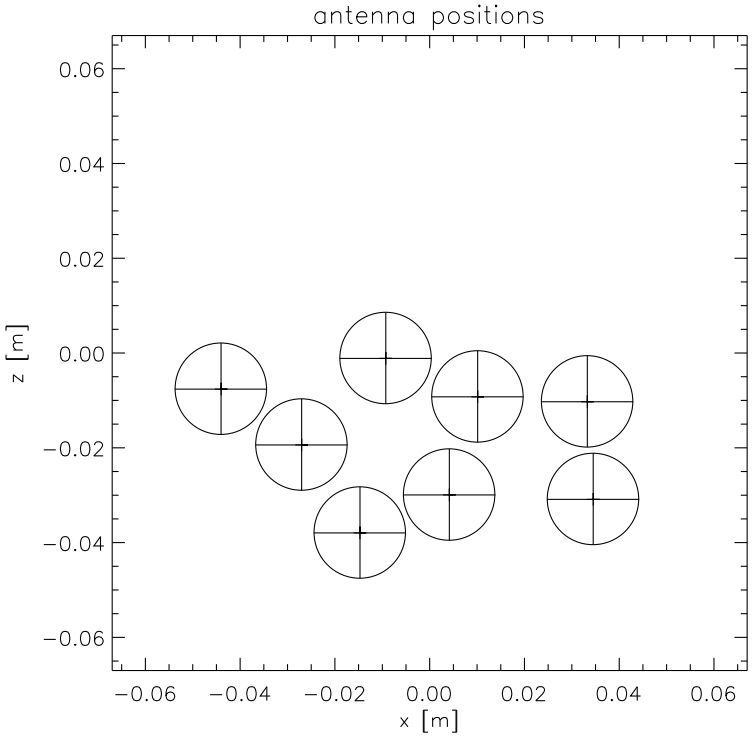

Figure 5.10: The optimal antenna placement found by the SA algorithm for 8 antennas with free placement. This is array configuration with which we ran performed experiments with for the majority of the MAST experimental campaign.

not to be enough however and the data from this experiment only provided information for the frequencies between 10 and 18 GHz.

As mentioned in section 4.1.1, the IF frequency sidebands have a destructive effect on the measurement of antenna phase. They must first be separated before any phase and amplitude calibration may take place. Assuming that the hybrids produce a perfect 90 degree phase shift and that the gains of each of the channels are equal, separation may be achieved by implementing the relations in expression (4.3) directly. In practice, however, the phase shift introduced by the broadband hybrid coupler is not perfect. This effect, combined with amplitude differences in the real and imaginary channels, caused by differences in amplifiers, gives a limit on the degree of separation that can be achieved. However, the deviation may be measured and we can correct for this effect, greatly increasing the suppression of the real upper (lower) sideband in the measured lower (upper) sideband or vice

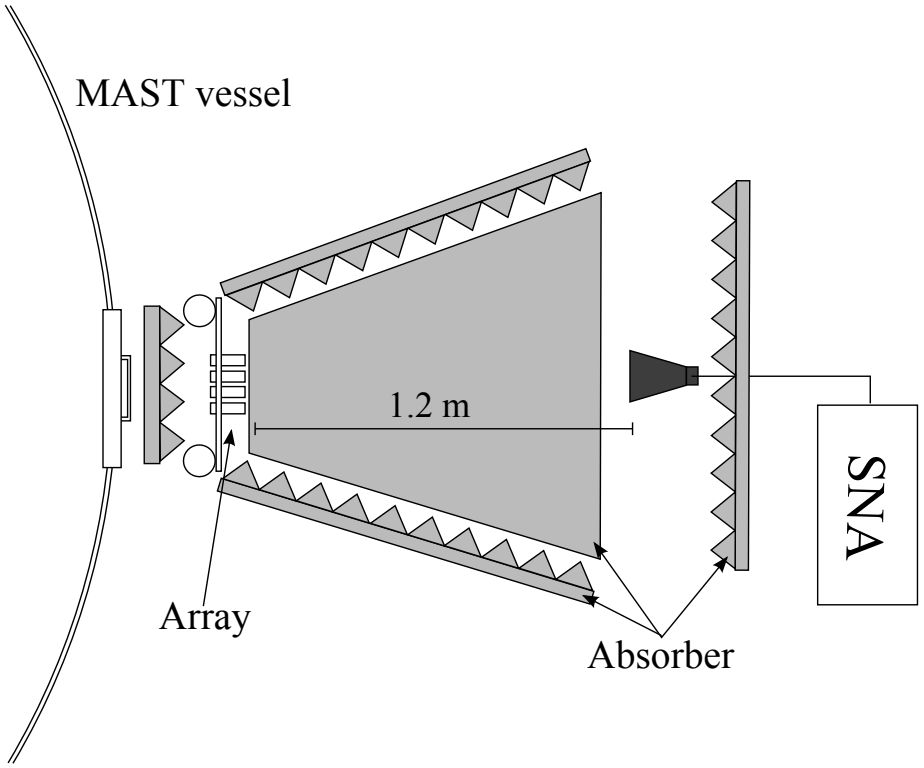

Figure 5.11: A schematic for the off-vessel calibration set up. The array was kept attached to the receiver and moved to point out from the vessel. The area around the array was covered in microwave absorbing material to minimise reflections. The dual polarised quad-ridged horn and Rohde and Schwartz SNA was used as the source.

versa. For imperfect I and Q channels we may define the measured I and Q components I' and Q', assuming we have normalised signals and allowing for the phase and amplitude difference, as:

$$\begin{aligned} I' &= A\cos\omega t \\ Q' &= \sin\left(\omega t + \phi\right) \end{aligned} \tag{5.1}$$

We can recalculate the original I and Q via

$$\begin{pmatrix} I \\ Q \end{pmatrix} = \begin{pmatrix} A^{-1} & 0 \\ A^{-1}\tan\phi & \sec\phi \end{pmatrix} \begin{pmatrix} I' \\ Q' \end{pmatrix}. \tag{5.2}$$

Then noting that:

$$\begin{aligned} \langle I'I' \rangle &= \frac{1}{2}A^2 \\ \langle I'Q' \rangle &= \frac{1}{2}A^2 \sin\phi \end{aligned} \tag{5.3}$$

we may correct the phase and amplitude errors at least to the degree that we can measure them. This procedure needs to be carried out separately for upper and lower sidebands since in the lower sideband $\phi \mapsto -\phi$ and the above procedure makes things worse unless that is taken into account.

Figure 5.12 shows the results of the upper sideband before and after suppression. The sideband suppression is the inverse ratio of signal power in the lower (upper) sideband, when only the upper (lower) sideband is stimulated, to the power in the upper (lower) sideband. After correction, this ratio is above 20dB in all channels and an be up to 38dB.

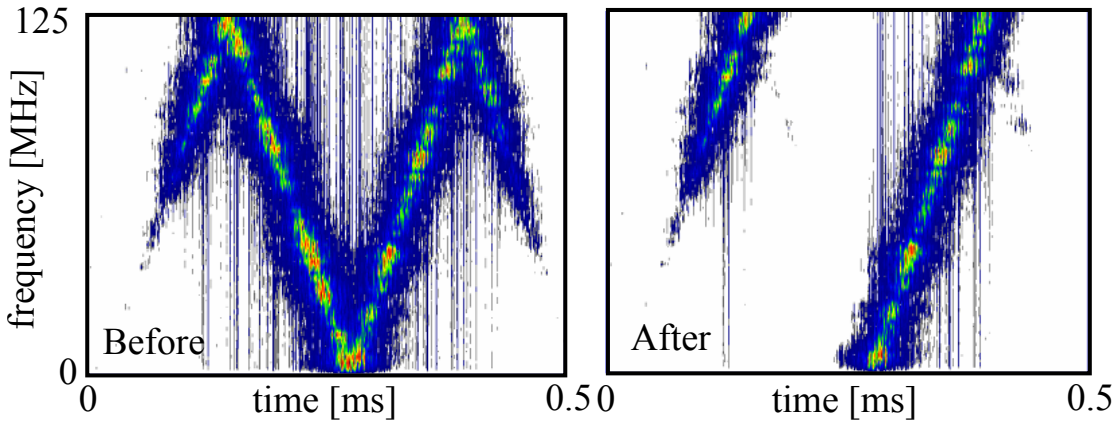

Figure 5.12: **Left**: A spectrogram of the period when the reflectometer signal passes one of our frequency bands, before sideband suppression. Notice the tails at either end of the trace. These result from aliasing due to the high frequency cut-off of our IF filters being above 125MHz. **Right**: The upper sideband after sideband suppression, the lower sideband is hardly visible on this scale. Notice too that the aliased part of the upper sideband has also been suppressed pointing to the fact that the aliasing is seen as a negative frequency and thus has a detrimental affect on the measurement of signal phase. The filters were adjusted after this result.

The left hand side of Figure 5.12, also show the presence of some aliasing due to the cut-

off frequency of our low-pass IF filters being above the Nyquist frequency for the digitiser. This is manifested in two "tails" either side of the characteristic "V" shape. We may also note that the sideband suppression has the effect of suppressing the opposite aliased part, i.e. lower sideband suppression suppresses the upper sideband aliased frequencies. This is because the aliasing has the effect of reversing the measured frequency. It is detrimental to the suppression ratio however, because a significant part of the opposite sideband remains in the suppressed signal; for this reason the cut off frequency of the filters was moved down to 110MHz.

Having successfully separated the sidebands, we are now able to measure the phase difference between antenna channels. There are many factors which can potentially affect the phase of a particular channel, including:

1. The difference in signal path from antenna to digitiser.
2. The difference in signal path of the local oscillator to the mixer.
3. Mismatches in polarisation of the antennas.
4. The ambient temperature.
5. The high frequency coaxial cable bend radius.
6. The impedance mismatch of all the high frequency connections.

Of these, points 1, 2 and 5 proved to be the most important. The fact that the phase of the transmitted signal would be sensitive to the cable bend was minimised by fixing all high frequency transmissions in semi-rigid/rigid coaxial where possible and having the transmission from the antennas to the LNAs made by phase stable cables, which also minimised the effect of the ambient temperature. The polarisation mismatch of the antennas was less than one degree, so this effect was negligible. The path differences were difficult to match and the only critical part of this was to ensure that the same local oscillator phase reached the I and Q channel mixers of any one antenna. Point 5 proved the most problematic, implying that if the antennas were disconnected at any point then the system would need to be re-calibrated, as the connections could not be made identical the next time.

With all this in mind, a calibration experiment needed to set up an environment where all path lengths for the radiation external to the diagnostic were known accurately. Then what remained was a function of the detector only, and could be subtracted. The easiest way to achieve this was to illuminate the array with an unresolved source. The path lengths would then be set by the distance from the source to each antenna and the cross-correlation phase by the antenna phases alone. This meant that reflections from other surfaces in the vicinity had to be suppressed as much as possible.

If we consider the expression in (3.9) and set I to be a δ-function at the origin of (η, ξ), we can see that the phase of all the cross correlations should be zero. This implies that all the antenna phases should be equal, and the most convenient selection is that they all equal zero. In this way we may see that any phase measured at an antenna, with reference to antenna 1, say, is instrumental and may be subtracted from all future measurements. Since the diagnostic is not absolutely calibrated, equalising the amplitudes is simply a case of multiplying the antenna signals by the correct real factor.

The first off-vessel calibration set the described source at the origin and completed a full calibration which was the working calibration through the majority of the campaign. The source was moved up by 10cm and again down by 8cm to check that the array was following the source correctly. This last point was explored more fully in the second off-vessel calibration.

The second off-vessel calibration experiment took place at the end of the experimental campaign and served three purposes. The first was to ascertain whether the calibration had drifted or been affected in any way over the course of the experiments. The second was to attempt to show that the array was able to track a source accurately over a wider range of angles. The third was to calibrate and demonstrate the capacity of an active Doppler backscattering component of the diagnostic which is not described in this thesis.

A very similar set up was used, with a greater range of source positions, moving the source from -15 cm from centre to +35 cm horizontally, and from -15 cm to +11.5 cm vertically at a distance of 1.2 m, which was the greatest range of movement possible. Figure 5.13

shows the results of image reconstruction for the majority of these positions for 10 GHz. From left to right in the figure the source moves vertically upwards and from top to bottom, the source moves to the right.

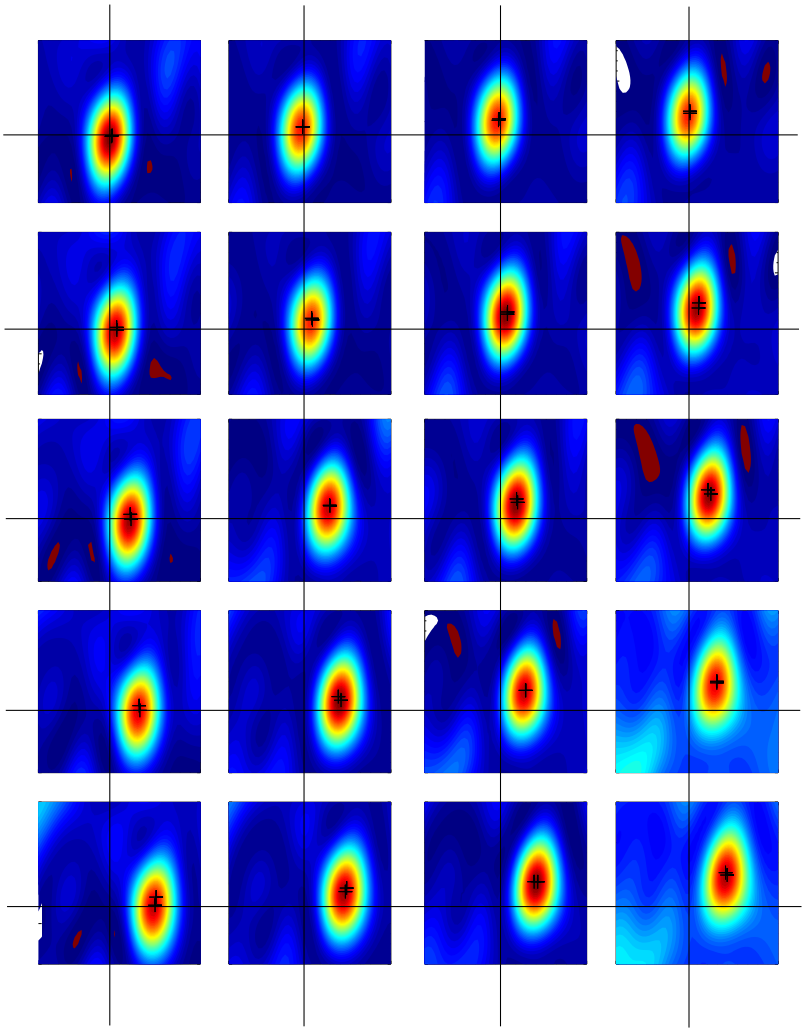

Figure 5.13: A grid of reconstructions of the Flann antenna source for 10 GHz. The angular range is $\pm 40°$ for each axis of each image. The images have been arranged so that the vertical position of the source increases left to right and the horizontal position increases down the page. The crosses plotted represent the maximum found by a spline method and the expected position of the maximum from the geometry of the experiment.

The first point that we can take from this is that the calibration has not drifted significantly over the course of the experimental campaign. The phases are still sufficiently close to

their original values to give well-formed point source reconstructions to within two degrees of the expected position. This is repeated in all frequency channels.

The second point we can make from this comes from examining the pictures in a little more detail. If we calculate the expected angular position from the geometry of the experiment and then use a spline interpolation to find the angular position of the maximum of the image, we can compare these values to look for discrepancies in angular position measurements. Figure 5.14 shows the horizontal difference in expected position and measured position vs the expected position for 15 GHz, this time.

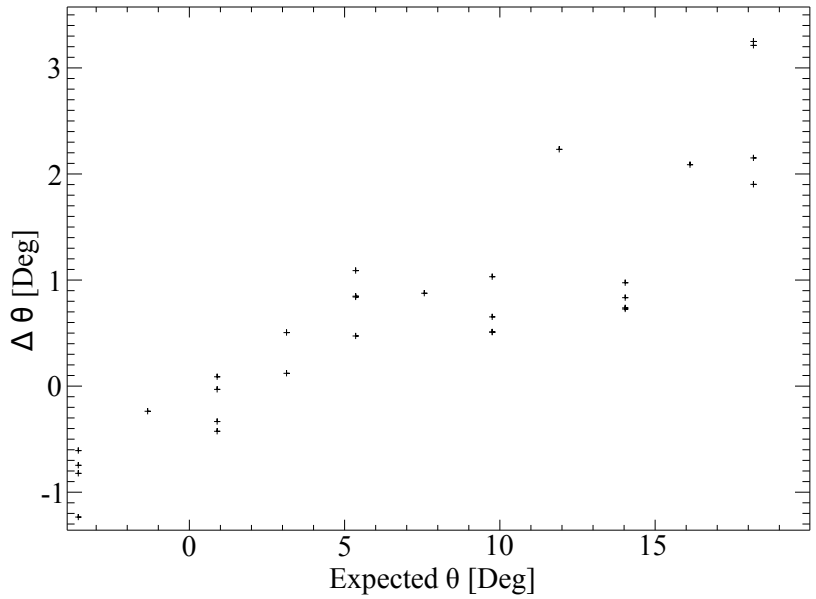

Figure 5.14: The horizontal displacement of the angular position as a function of expected angular position for 15 GHz. This is representative of all the frequency channels at both upper and lower sideband. Here $\Delta\phi = \phi_{\text{measured}} - \phi_{\text{expected}}$, The overestimate of the magnitude of the angular position is 10% and is the same within error on all frequency channels

There is a clear trend in the data here, which is to overestimate the magnitude of the angular position by 10%. The same gradient in this data is seen at all frequencies, pointing strongly to a geometrical effect, but the magnitude of the error is far outside the experimental uncertainties in the position of the source. The suspect is then with a near-field effect, that is to say the discrepancy in the phase difference estimated by assuming the source is

at infinity and the actual phase difference caused by the differences in path lengths. To test this, we calculated what the phase difference should be given the real geometry of the situation and compared this with the measured phases. They did indeed match within the random error, allowing us to conclude that this effect was behind the measured discrepancy in the measured angular positions.

5.3.2 on-vessel calibration

In moving the antenna array from the off-vessel calibration position to the on-vessel position, a few things change which could potentially affect the calibration values. The cable positions are different, with different bend radii, which may introduce small phase shifts. There is a fused silica window in front of the array which may produce reflections that enhance the cross talk and there is a metal flange which holds the window which may affect the antennas' response.

To ensure that the calibration was still valid looking into the vessel, we performed some experiments which directed a single side band noise-like source through various port windows opposite the array. Figure 5.15 shows the view in the vessel from the perspective of our array. The crosses inside the circular ports indicate the positions which we situated the test source.

There are many problems with directing signals through the vessel, the most serious being caused by the interference of multiple reflections when using a coherent source. For this reason, as a source we used a string of amplifiers together with two mixers and hybrid couplers to amplify and up convert thermal noise to the frequency range of our diagnostic. The coherence length is defined as one standard deviation in expression (3.24) for a Gaussian frequency distribution. The principal bandwidth was 50 MHz, creating a coherence length of 6 meters. Since the vessel is 4 meters in diameter, the interference effect should be strongly suppressed for any more than one reflection across the vessel. These reflections, however, will act to reduce the overall normalised correlations as they will contribute to the measured power, but not to the correlation coefficient. Those reflections

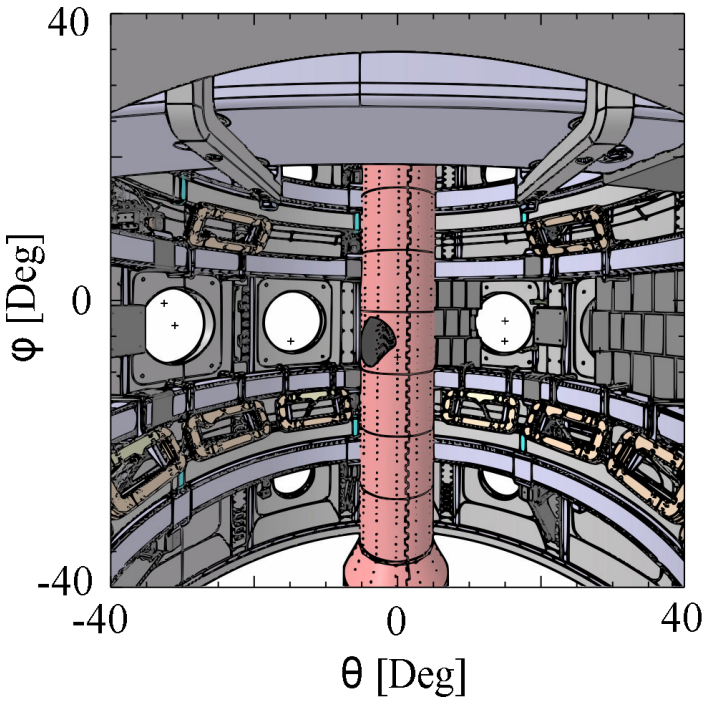

Figure 5.15: A drawing of the inside of the vessel as seen by our array. The crosses inside the circular ports mark the various source positions used in each successive calibration shot.

which are from the centre column can have some appreciable stable phase relationship with the source and can introduce a some interference effect. Figure 5.16 shows some examples of potential paths of the radiation from the source to the array. With no reflections the signal behaves exactly as predicted, however, paths 2 and 3 have different path lengths and therefore a different degree of coherence with the non-reflected signal.

Figure 5.17 shows the source injected from sector 2, with the MAST vessel outline overlaid for clarity. The reconstruction of the image lies almost directly at the expected position, with a deviation that is consistent with the off-vessel calibration experiments. This suggests that the reflections for this shot are not as important as for others.

Figure 5.18 shows a reconstruction of the source injected from sector 11. Again the MAST vessel is overlaid. We can see in this instance that the main power appears to come from the left hand side of the central column. Since the antenna was held normal to the window,

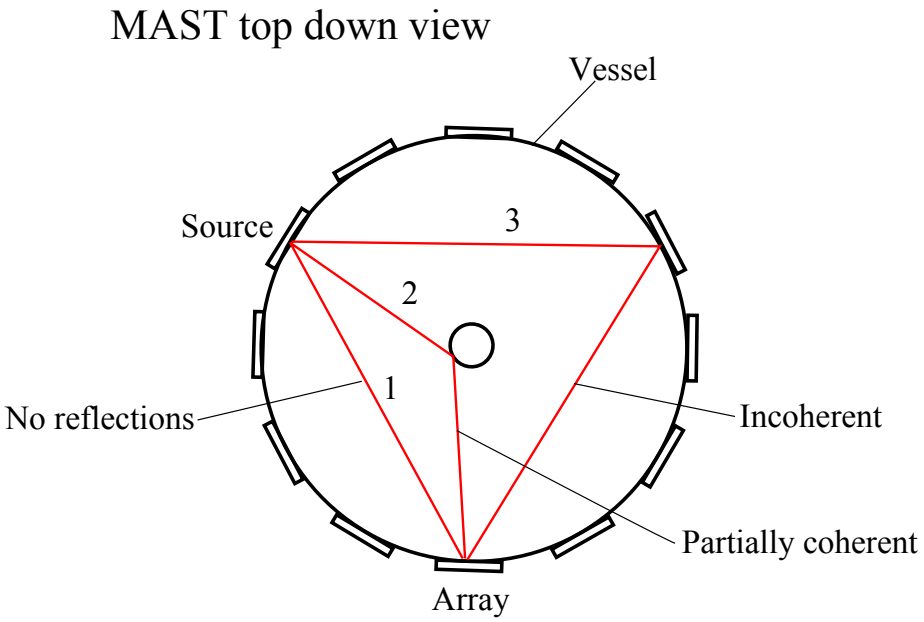

Figure 5.16: A diagram showing three possible routes for power to reach the array from the source. The first is straight with no reflections, the second is a reflection from the centre column and the third is a reflection from the opposite side of the vessel.

the majority of the power would be directed at the central column, so this is not surprising. However this picture is present on may frequency channels. This picture is not so clear on some other frequency channels and it believed that coherent effect are to blame for this.

Figure 5.19 shows the impact of the multiple reflections in the degradation of the correlation magnitude of the cross-correlation between the antennas. In order for these results to be used as a fine calibration more must be known about how the signal is reflecting inside the vessel. These results do however give us confidence that our off-vessel calibration is transferable.

5.3.3 Correlated noise

During the plasma experiments it became clear that, especially for the lower frequency channels where the signal power was least, there was some consistency between the correlation measurements in the noise and the correlation measurements during the plasma

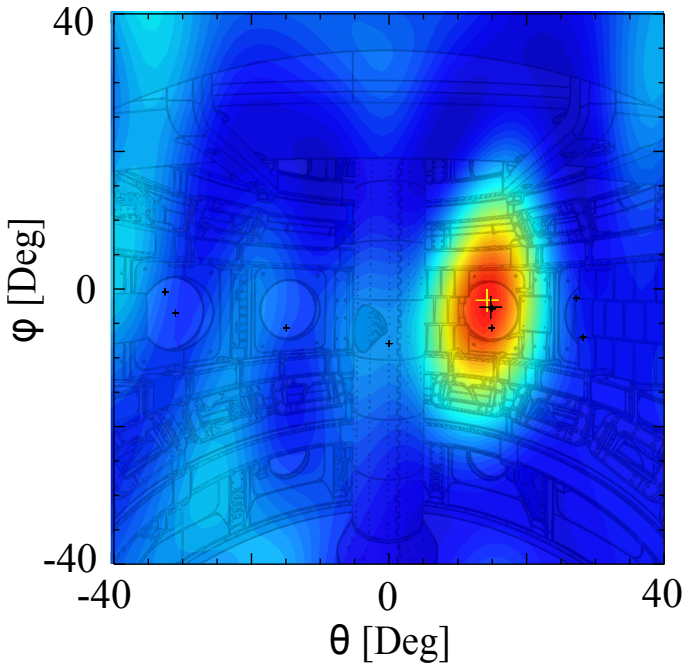

Figure 5.17: A reconstruction of the noise like source at 13 GHz with the MAST vessel overlaid. We can see that the phase calibration holds remarkably well. The yellow cross indicates the angular position of the maximum of the reconstruction, it lies only two degrees higher and one degree to the left of the expected position. This is entirely consistent with the small offsets found in the off-vessel calibration.

emission. Figure 5.20 shows the Pearson correlation coefficient for all possible pairs of the I component of each antenna as a function of frequency. The correlations are taken with no signal present at all and so any correlation represents correlations in the noise between antennas.

We can see that the correlation is of the order of 10% at the lower frequencies and decreases as the frequency increases. This is consistent with the hypothesis that this correlated noise is noise from the low noise amplifiers (LNAs), which is re-emitted by the antenna and consequently picked up by neighbouring antennas. This hypothesis is strengthened by the fact that some of the LNAs sustained damage during testing and consequently have a higher noise at the input end. Correlations involving these antennas are higher than those not involving these antennas.

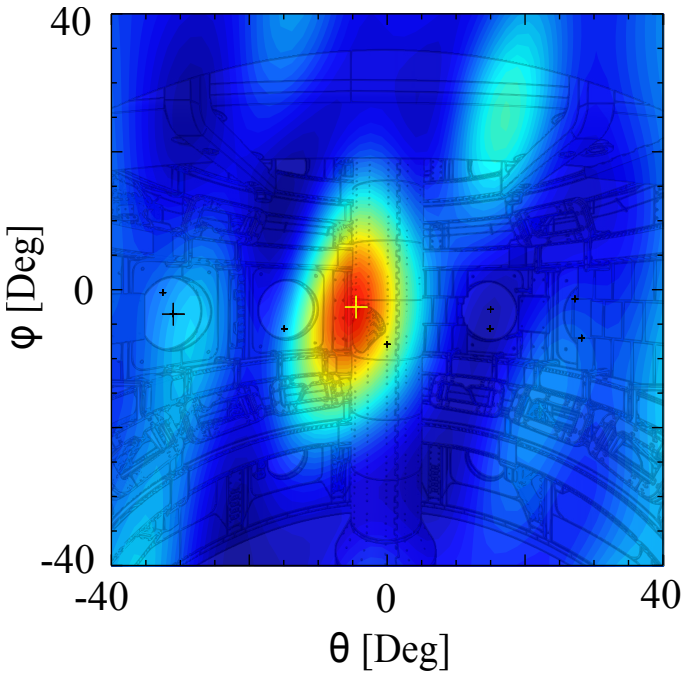

Figure 5.18: A reconstruction of the noise like source at 13 GHz with the MAST vessel overlaid. This reconstruction is of a source injected at sector 11 in the far left. The antenna is held perpendicular to the window and thus most of the power seen in the image comes from the reflection from the left hand side of the centre column

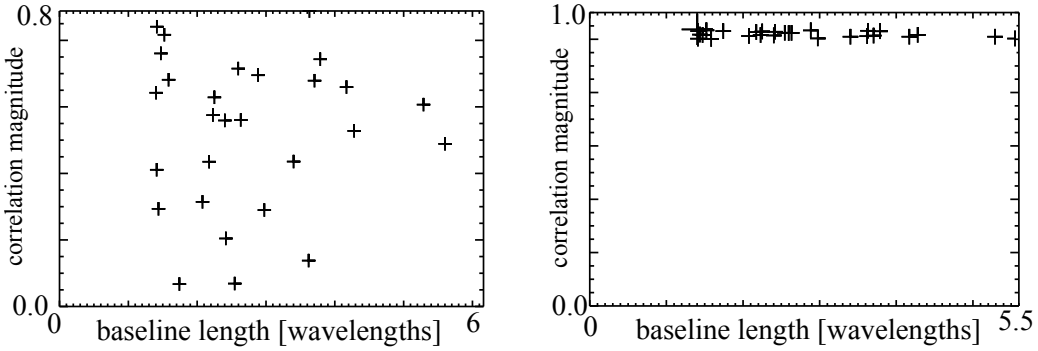

Figure 5.19: **Left**: The normalised correlation magnitude as a function of baseline length for the most point like reconstruction in the vessel for 20.5 GHz. **Right**: The same, but for the off-vessel experiments. There is a marked difference between the two, indicating that there is significant reflection inside the vessel.

Since this correlation is present at the same magnitude in all circumstances, this correlation may simply be subtracted from the correlations calculated when there is a signal in front

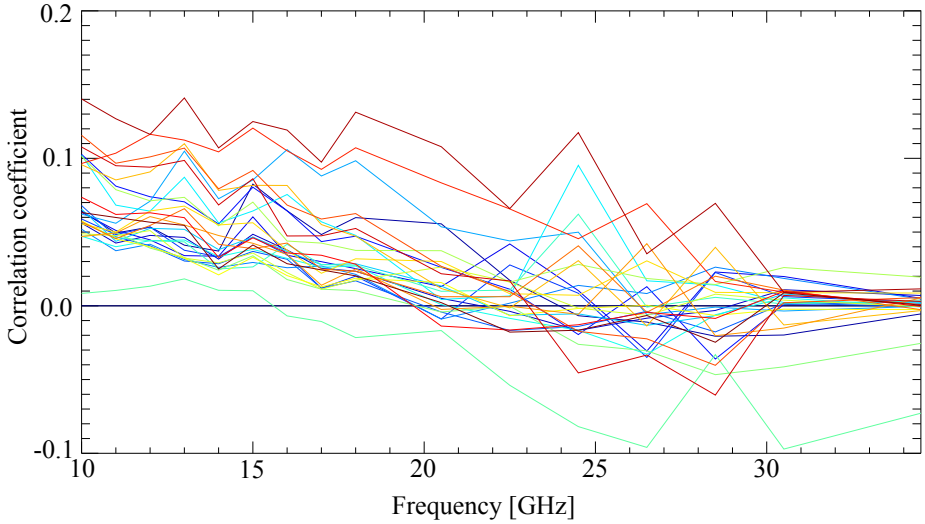

Figure 5.20: The correlation coefficient of the noise for each antenna pair. The points represent average correlations over 83 shots.

of the array, thus completely removing this effect. The theoretical justification for this is given in section 3.2.4. In practice this correlated noise is calculated for each plasma shot, ensuring that changing conditions do not affect this offset removal.

Chapter 6

MAST Plasma Results

6.1 Comparison of images with full wave predictions

In this section, I will present the first ever images of B - X - O mode conversion in a tokamak. Initial attempts at analysis of the images showed a disagreement with the coupling mode conversion transmissivity alone. As we shall see, in order to get a good qualitative agreement between theory and experiment it was necessary to include the effect of the Bernstein wave refraction in the plasma, which drastically alters the images we expect.

What is presented here is by no means a comprehensive analysis of the mode conversion process, but a simple comparison to the numerical code AMR, written by Urban and Prienhaelter [74]. AMR is a one dimensional full wave coupling, Bernstein wave ray-tracing simulation code. This code uses an adaptive mesh refinement method for solving the mode conversion problem in one dimension and a ray-tracing part for tracking the Bernstein waves through the plasma.

The experimental and simulated images come from MAST shot 27004, which is a shot with an extended H mode period, with no large ELM events. The left plot in Figure 6.1 shows the D_α light emission as a function of time, the green dashed lines indicating the time of the images presented.

AMR uses the experimental data for temperature and density measured by the MAST high

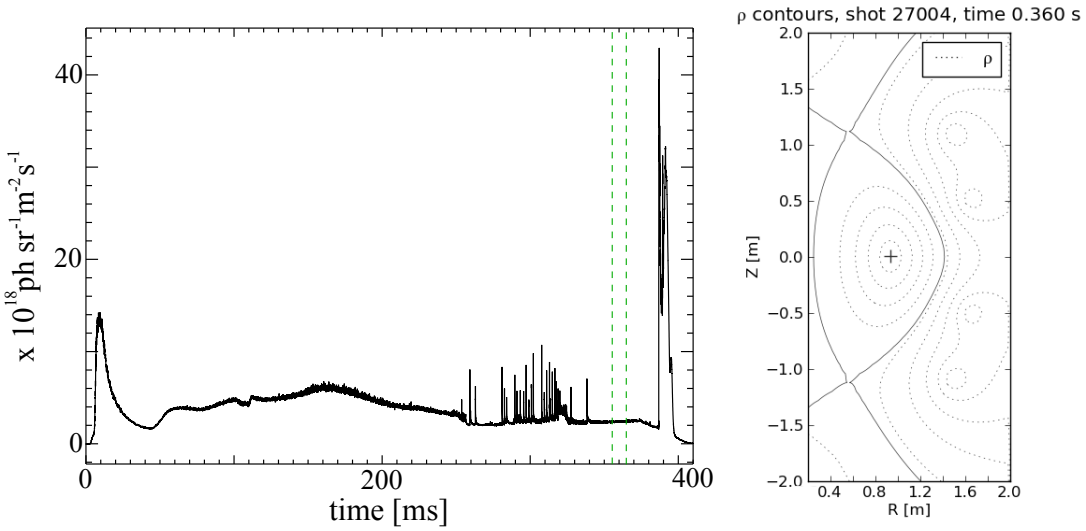

Figure 6.1: **Left**: The D_α emission for shot 27004. The green deashed lines indicate where the image reconstructions and AMR simulations were run. **Right**: Contours of poloidal flux reconstructed from the equilibrium fitting code EFIT

resolution laser scattering system, shown in Figure 6.2. It then maps this information away from the mid-plane by assuming these quantities are constant along a flux surface and using the equilibrium reconstruction from the equilibrium fitting code, EFIT. The solid lines in the graph on the left hand side of Figure 6.2 show the density and temperature using this mapping. We can see that they do not quite line up with the experimental measurements for small radii, but are a reasonable approximation in the absence of any other mapping criterion. The equilibrium used for this reconstruction is shown on the right hand side of Figure 6.1.

As we can see from the right hand graph of Figure 6.2 the range 10 - 34.5 GHz covers three harmonics of cyclotron emission, all of which lie below the plasma frequency, thus electromagnetic emission in this range must be dominated by the mode converted Bernstein wave thermal emission born at these cyclotron harmonics.

I ran AMR simulations for all the reconstructions with a good signal to noise ratio, calculated using equation 3.19, up to 18 GHz using the largest angular range possible without any part of the grid missing the plasma. Figures 6.3 to 6.7 show the AMR calculations

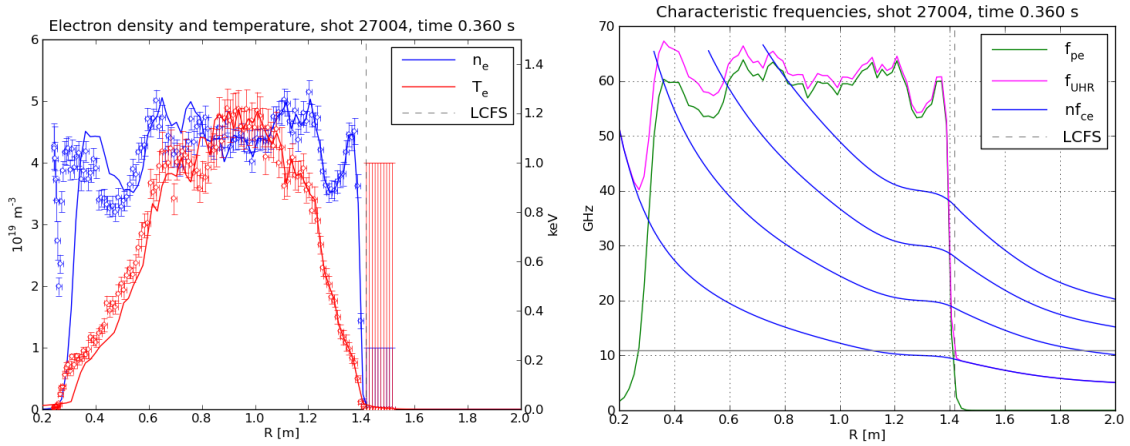

Figure 6.2: **Left**: The Thomson scattering profiles of density and temperature for shot 27004 at 360 ms. **Right**: The corresponding harmonic topology, showing 4 harmonics of the cyclotron frequency f_{ce}, the plasma frequency f_{pe} and the upper hybrid frequency f_{UHR}

of the mode conversion (MC) efficiency and the apparent radiation temperature profiles without the mode conversion efficiency; the emission brightness is the product of these two quantities. This anisotropy in the radiation temperature alone is caused mainly by the refraction of the Bernstein waves. This radiation temperature is peaked on the mid-plane, which is situated at -16° as seen from the antenna array. As we move further from the mid-plane, the Bernstein waves tend not to originate from the cyclotron harmonic as one might expect, but from closer to the plasma edge, where it is colder. When both the mode conversion and the origin of the Bernstein waves is taken into account, we may observe quite different emission from what we would expect considering mode conversion alone.

When we examine figures 6.3 to 6.7, we can see some trends with increasing frequency. Firstly, at 14 GHz, the lower mode conversion window is more efficient than the upper, but as we transition to higher frequencies the upper window becomes more efficient, while the lower window looses efficiency. At 14 GHz the lower window is 64% efficient at its peak, whereas the upper is only 40%. At 18 GHz however, the upper window is 64% and the lower around 40%. This trend is continued at even higher frequencies, with the upper window being 70% efficient at 28.5 GHz, where the lower is only a little over 30%.

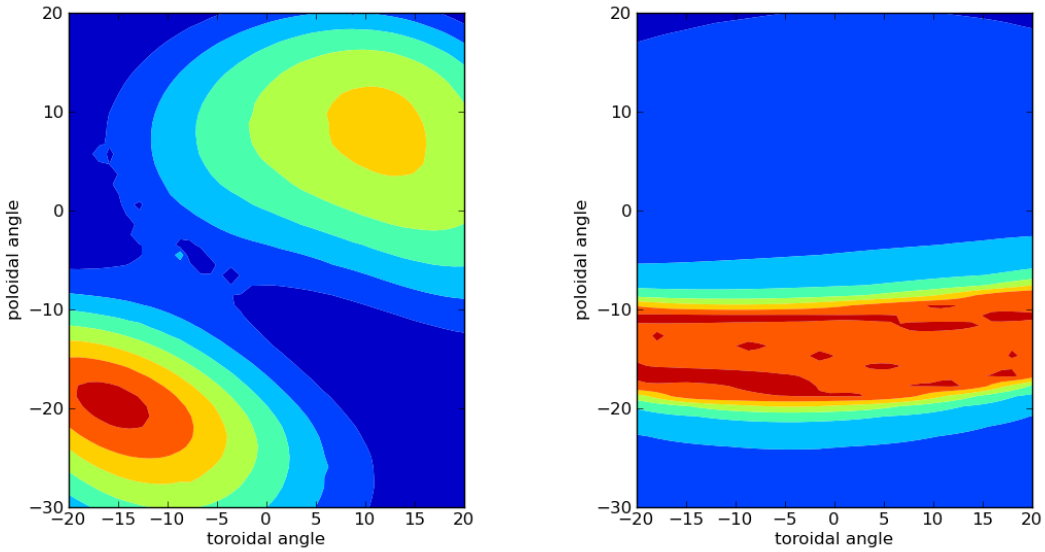

Figure 6.3: **Left**: The result of the AMR calculation for the mode conversion efficiency as a function of angle from our antenna array, for 14 GHz. Toroidal angle is equivalent to θ and poloidal angle is equivalent to ϕ. **Right**: The apparent temperature of the Bernstein waves as a function of angle; this is caused by the Bernstein waves originating from different places in the plasma and hence beginning at different temperatures.

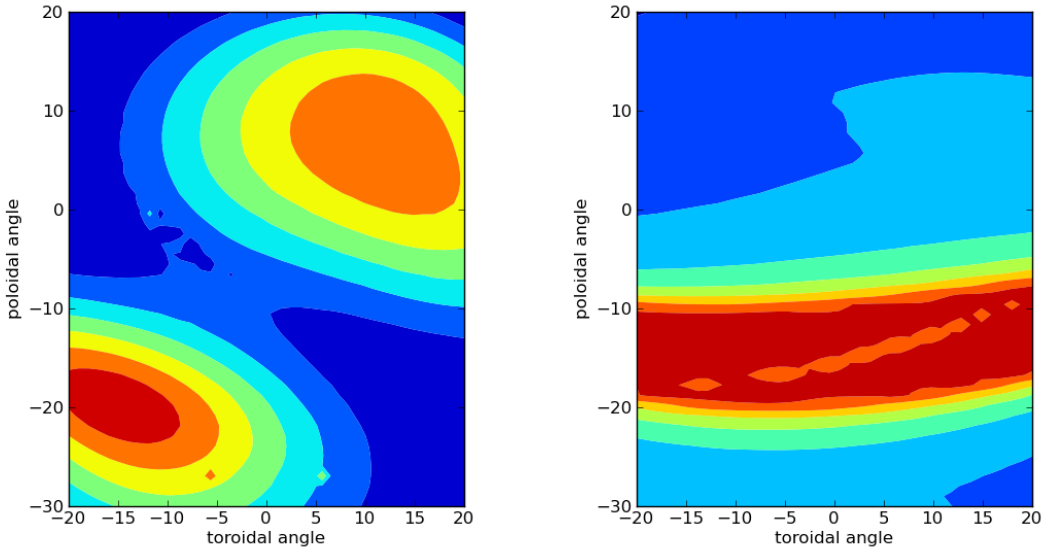

Figure 6.4: The same as 6.3, but for 15 GHz

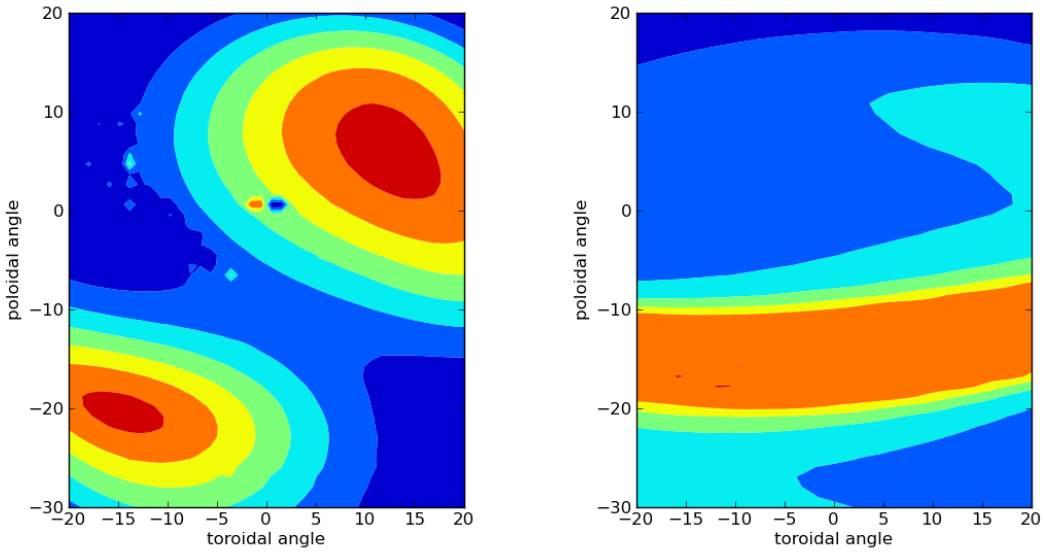

Figure 6.5: The same as 6.3, but for 16 GHz

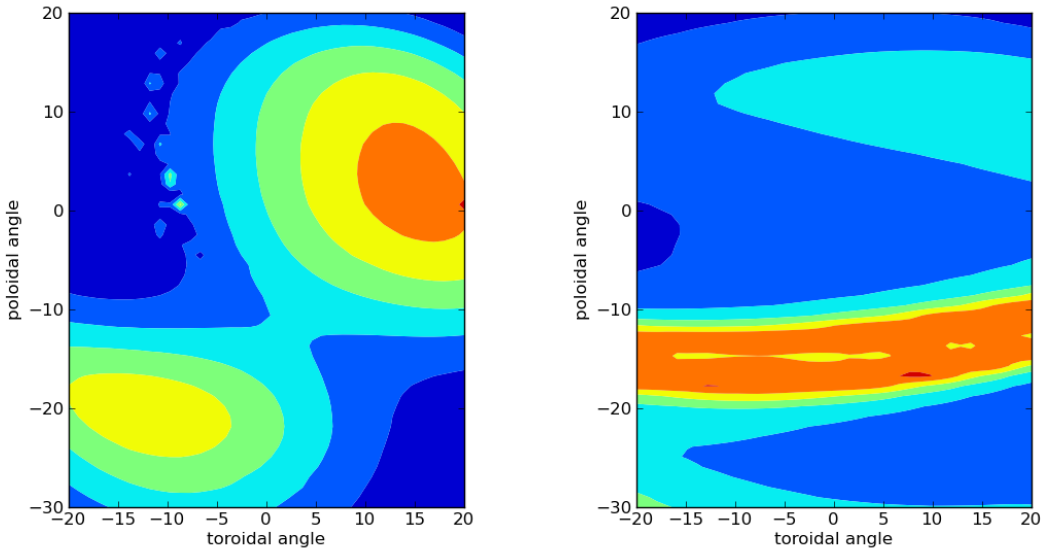

Figure 6.6: The same as 6.3, but for 17 GHz

The second trend we may notice is that the Bernstein wave radiative temperature becomes more peaked on the mid-plane with increasing frequency. This trend appears to continue at higher frequencies, but when we reach 28.5 GHz, the mid-plane emission has collapsed and the peak of the radiative temperature is off mid-plane.

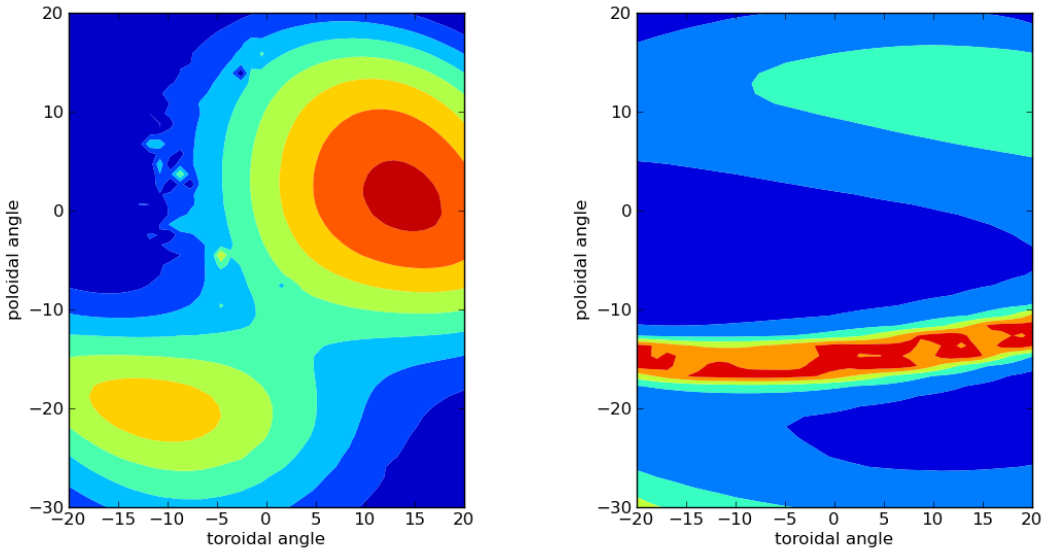

Figure 6.7: The same as 6.3, but for 18 GHz

The next sequence of figures, from 6.8 to 6.12 show experimental image reconstructions (left) compared to the AMR predictions of brightness *vs.* angle (right): note the differences in angular range. The reconstructions were formed using SAMI in full sweep mode, switching between all 16 frequencies sequentially. Each individual integration period is 5 μs and a complete sweep takes 160 μs, when we allow for the time it takes for the oscillators to settle in between switches. The individual 5 μs correlations are then averaged over a period of 10 ms and then used to form an image. The reasons for this relatively long integration time are not of signal to noise but of the dynamics of the mode conversion windows as described in section 6.3. The upper sideband images are shown as a convention, but we examine the difference in upper and lower sideband images in 6.2

Starting with Figure 6.8, which shows the experimental image and AMR reconstructions for 14 GHz, we can see that there exists here one well defined lower MC window in the experimental data. It appears almost exactly in the position predicted by the AMR simulation. The lower window is somewhat more circular in the experimental image and horizontally extended in the AMR simulation. The upper MC window in the experimental reconstruction is far more diffuse and less bright. This is reproduced in the AMR sim-

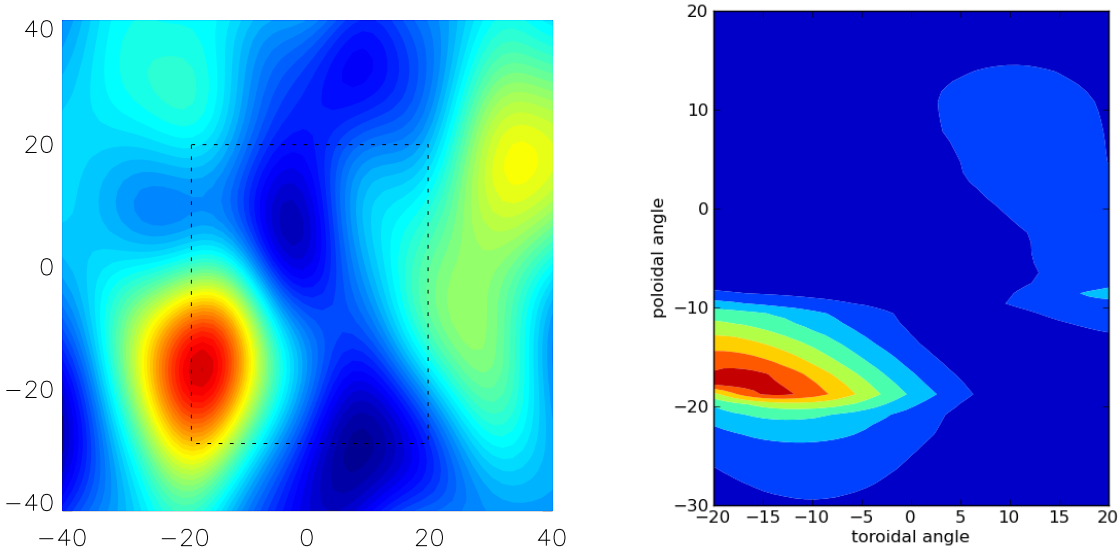

Figure 6.8: **Left**: A reconstruction of the image observed at 360 ms for shot 27004 over the range from -40° to 40° in horizontal and vertical directions. The boxed region denotes the angular range over which the AMR simulation was performed. **Right**: The AMR reconstruction of the image brightness which is the product of the two figures in 6.3. Notice that the lower MC window appears to within a few degrees of where it is expected, whereas the upper mode conversion window is somewhat more diffuse.

ulation, although the experimental upper window extends lower that the reconstruction. There also exists the presence of a brighter spot above and to the right of the upper mode conversion window. Since this location is obscured in reality by a poloidal field coil, it is likely that this is either an imaging artefact or a reflection from this surface.

If we move on to 15 GHz (Figure 6.9), we now see two very well defined mode conversion windows, again very close to their predicted positions. This image shows the importance of including the radiation brightness in the image analysis as the apparent position of both the upper and lower windows have been changed significantly by this effect, appearing to reduce the magnetic pitch angle. The relative brightness shown in the AMR simulation is not reproduced by the experimental data.

Figure 6.10 shows the comparison for 16 GHz. We now see some significant distortion in the upper MC window, appearing horizontally extended and to split in two windows. This

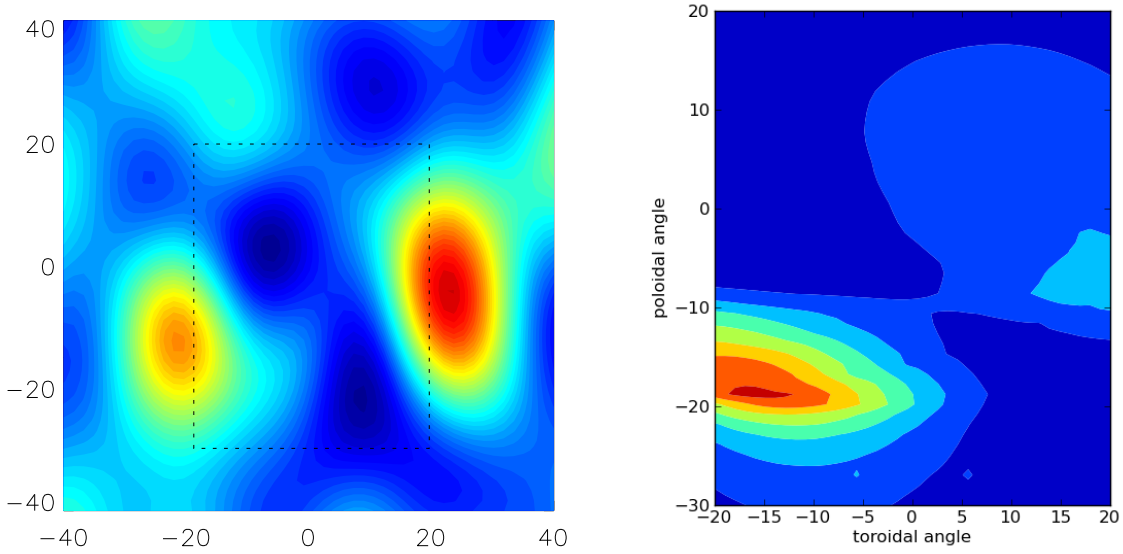

Figure 6.9: The same as 6.8, but for 15 GHz. Notice here that the lower MC window is again within a few degrees of where it is expected, but the upper window is somewhat lower than we would expect from considering mode conversion alone.

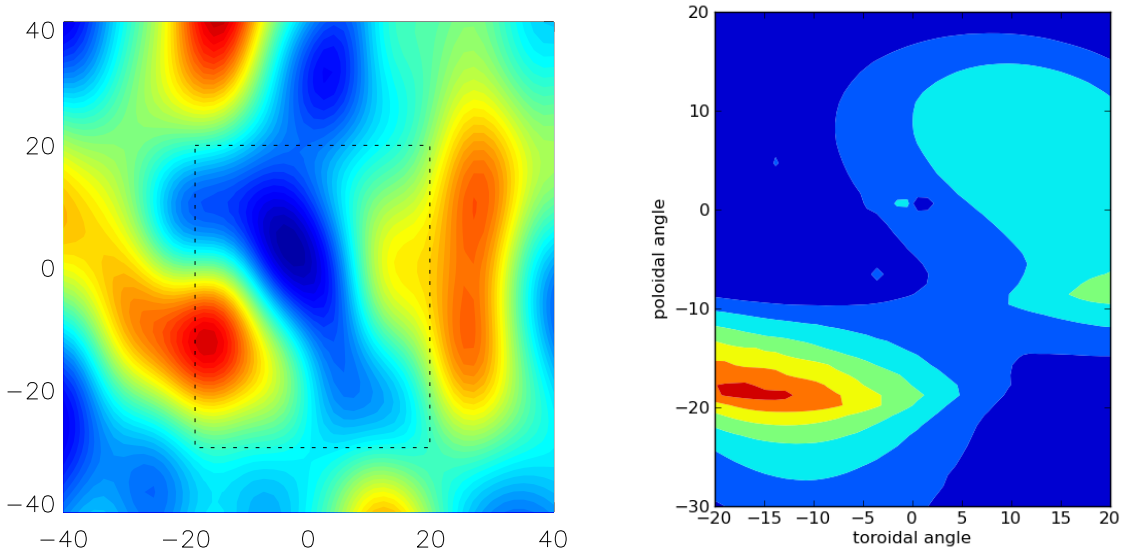

Figure 6.10: The same as 6.8, but for 16 GHz. Here the reconstruction on the left shows a window splitting into two.

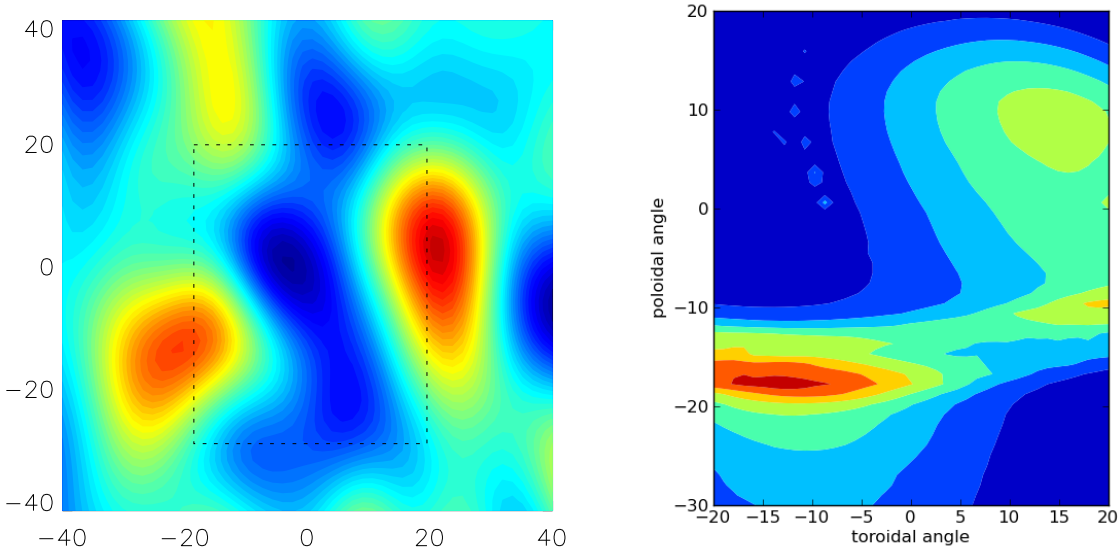

Figure 6.11: The same as 6.8, but for 17 GHz. Here the reconstruction on the left shows more well defined mode conversion windows with the lower being horizontally extended, and the upper being vertically extended. The AMR simulation shows the upper MC window splitting into at least two.

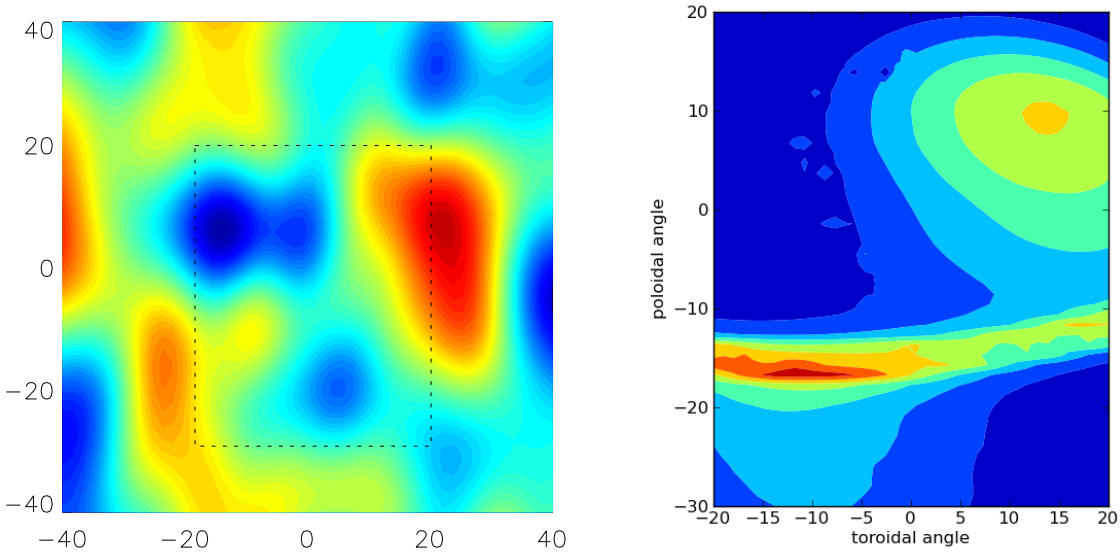

Figure 6.12: The same as 6.8, but for 18 GHz. Now the lower window in both experiment and simulation appear to have collapsed, but the upper window has moved higher and become broader.

splitting is not seen in the AMR simulation at this frequency, but if we look at Figure 6.11, we can see that the upper MC window can indeed appear to split into two. This effect again is one of including the radiation brightness temperature, as the mode conversion efficiency does not split into three windows. The fact that this splitting is seen in the experimental images at a lower frequency than in the AMR simulations seems to point out a more general trend in these images, of the upper window becoming more efficient at frequencies lower than predicted. The trend is consistent, but the magnitude of the MC efficiency appears to be out slightly. Again, notice the bright spot at the top of the experimental reconstruction. This appears in a position which is completely covered by a poloidal field coil and so is not plasma emission. This is not likely to be a sidelobe since it does not seem to be correlated with the brightness of either window, this can be seen in Figure 6.19, which is a sequence of images showing the dynamic behaviour. The most likely cause is then a reflection of emission from a different part of the plasma.

Now looking at 17 GHz in Figure 6.11, we see that the upper MC window appears to be breaking away from its place just above the midplane and heading closer to the prediction form MC alone. The breaking away of the upper window again happens at a lower frequency than predicted staying consistent with the hypothesis that the upper window is relatively more efficient than predicted. The lower window is now beginning to show signs of extending downwards as predicted.

Finally, the 18 GHz experimental reconstruction shows the lower window extending more downwards and beginning to collapse as the upper window dominates. The upper window is now broader and more defined.

In general there is a reasonable qualitative agreement between modelled and experimental images. Most of the qualitative features are reproduced: the diminishing strength of the lower window, the upper window splitting in two due to the radiative temperature of the Bernstein waves and the eventual increase in the poloidal position of the upper window. There are also unknowns in the model which may have a measurable effect on the predictions. For example the spinning mirror experiment revealed a significant variation in the magnetic field [14] which would not be resolved by the EFIT code and so would not

be present in the AMR model. This could affect the way the Bernstein waves refract and therefore affect the radiative temperature. AMR solves the coupling efficiency using a one dimensional method, neglecting magnetic curvature, shear and misalignments of the field and density surfaces. Also, as we shall see in section 6.3, the images display a high level of dynamics which may not average out to the expected value in a long exposure. Although it is outside the scope of this thesis, it would be prudent to perform a study of the relative importance of these effects.

6.2 Differences in upper and lower sideband images

The upper and lower sideband central frequencies are separated by 100 MHz. At 14 GHz, this amounts to a difference of just 0.71%, and at 18 GHz this difference is just 0.56%. Thus any changes in the behaviour of the array between these two must be negligible. The only thing which may be different between the sidebands are small phase calibration errors from the calibration process described in section 5.3.1. Significant differences between images separated by 1 GHz steps have already been observed. Since the frequency separation is 10% of this frequency step, we may expect there to be small but measurable differences in the emission between frequencies separated by 100 MHz. Figures 6.13 to 6.17 show a comparison of the upper and lower sideband images for the same shot as before (# 27004, 360 ms).

Starting with 14 GHz (Figure 6.13), we can see firstly that the images are very similar, the position of the lower MC window is the same within $\pm 1°$ and the shapes are very similar. In the lower sideband, the diffuse upper window is at a slightly higher angle and the spurious feature, which we presume to be an artifact due to the positioning of the poloidal field coil, appears nearly 10 degrees higher.

At 15 GHz (Figure 6.14) the shapes and positions of the MC windows are reproduced very well between the two. However there is a difference in the relative brightness of the two windows, with the lower sideband upper MC window being dimmer than the same in the upper sideband.

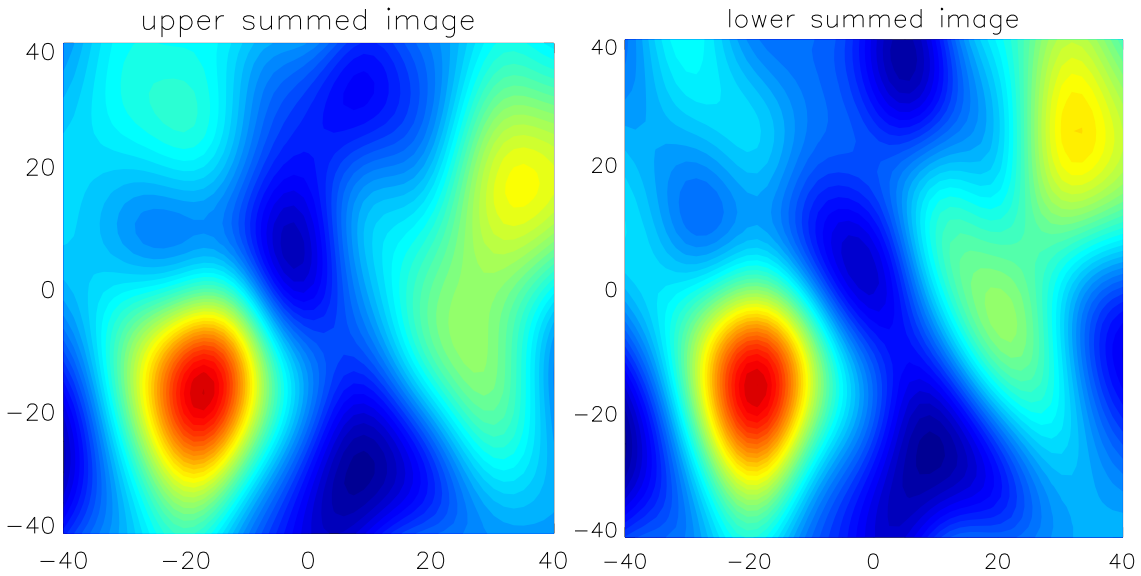

Figure 6.13: The upper and lower sideband images for correlations averaged over 10 ms around 360 ms of shot 27400. We can see small differences in these images even though they are separated by just 0.7% in frequency terms.

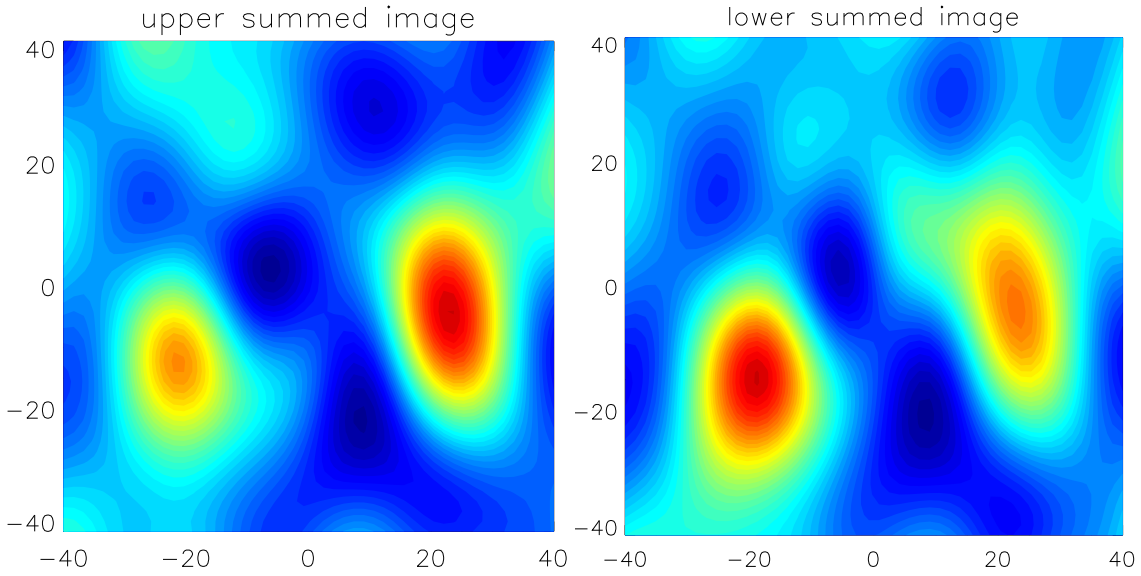

Figure 6.14: The same as Figure 6.13 but for 15 GHz. The positions and definition of the windows is preserved, but the relative brightness is not.

The images at 16 GHz (Figure 6.15) give the largest deviation from each other. Again the lower window is closer to its companion than the upper window, but there is a small

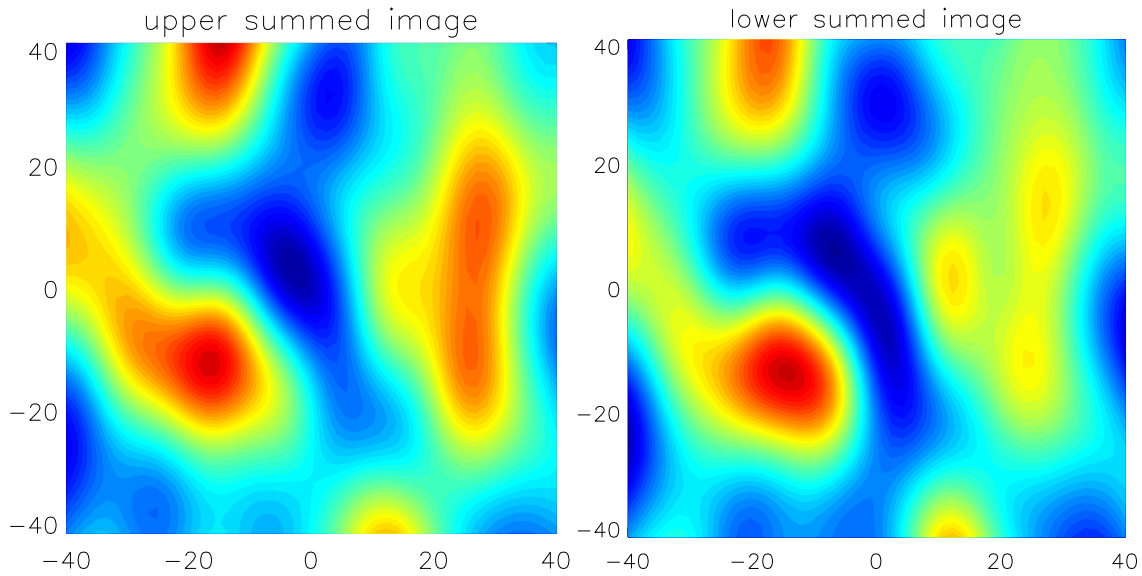

Figure 6.15: The same as Figure 6.13 but for 16 GHz. This shows the most marked difference, the lower window is very similar, but the upper window here appears to have split into three. There is some trace of a third window in the upper image, but it is swamped by the other two.

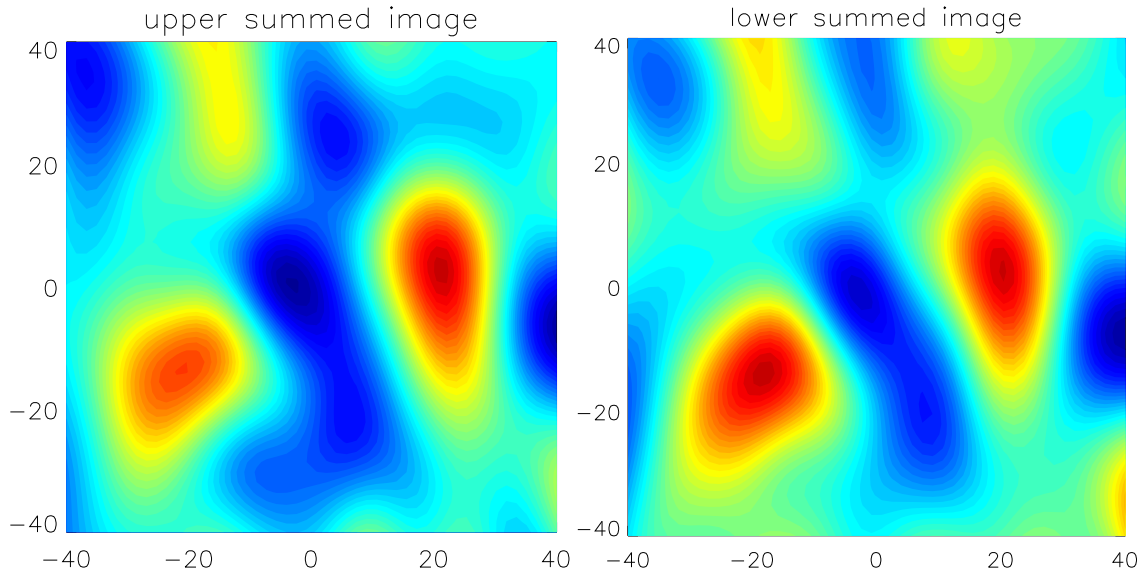

Figure 6.16: The same as Figure 6.13 but for 17 GHz. These two are very similar, the relative brightness is not quite the same, but the shape and position are.

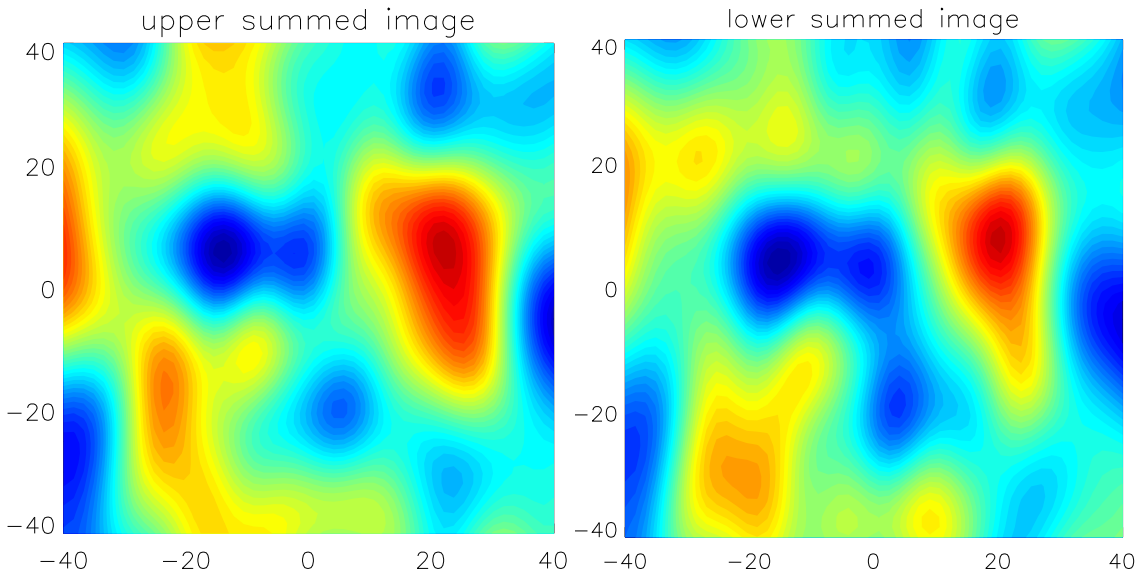

Figure 6.17: he same as Figure 6.13 but for 18 GHz. Again, some small differences in shape with the overall positions being preserved.

distortion of shape even for the lower window. The upper window, where it appears in two in the upper sideband image, appears in three in the lower sideband image. There is a hint of the third window (to the left of the extended feature in the right hand side of the upper sideband image) appearing in the upper sideband, which is dimmer than the other two.

The upper and lower sidebands produce very similar images again for 17 GHz. There is some discrepancy of the relative brightness. A bigger difference is found at 18 GHz (Figure 6.17). Here, the upper window is smaller in the lower sideband, although still vertically extended. The lower window is both lower and more horizontally extended than its companion in the upper sideband.

6.3 Dynamics

The reconstructions in the previous two sections were all formed with correlations averaged over 10 ms, when an integration period of 5 μs is easily enough to satisfy the signal to noise requirements for these frequency channels. The reason is that the images are

highly dynamic and only become stable when correlations are averaged over a period of at least 2 ms. Figure 6.18 shows fifteen successive 5 μs frames of data for 15 GHz in the middle of the integration period used in section 6.1. We can see that the upper and lower MC windows vary in position and brightness throughout this period in a way that doesn't seem connected between frames. This implies that there is some process which is acting to distort the windows, or change the apparent radiation temperate on a timescale smaller than the 0.16 ms frequency sweep.

Figure 6.19 shows significantly more dynamic behaviour with the upper MC window changing its vertical extension and sometimes appearing to split into two and subsequently rejoin. The lower window in this instance behaves more like the windows in Figure 6.18, changing its position by less, but undergoing significant changes in brightness, almost disappearing in the 4th frame. There are many potential candidates for the image fluctuations, for example the mode conversion efficiency depends sensitively on the density gradient as it is effectively a tunnelling process. Edge density fluctuations may cause quite dramatic fluctuations in the observed power at any one angle. Work investigating this has been done by correlating the density fluctuations observed at a langmuir probe [75] and a density reflectometer [76]. Also an analysis including the effect of the density fluctuations' distortion of the plasma density surface was done by Laqua *et al* [77]. Other candidates include fluctuations in the magnetic field, causing refraction of the Bernstein waves and core temperature fluctuations

SAMI brings a great deal of new information to this problem, providing two dimensional information on the fluctuations in mode conversion brightness. A faster time resolution is certainly necessary for further investigations however, and could be achieved by observing fewer frequencies to bring down the sweep time. SAMI is very capable of doing this owing to its FPGA controlled local oscillator switching system. In the more extreme case we can observe a single frequency, cutting the dead time while we wait for the local oscillators to settle and potentially decreasing the integration time for the frequencies with the highest signal.

Analysis of this data on this timescale requires a completely different method as to the one

in section 6.1. The code must be able to deal with non monotonic densities and complex 3 dimensional structures. Such full wave codes are in development, but I have access to none at the time of writing.

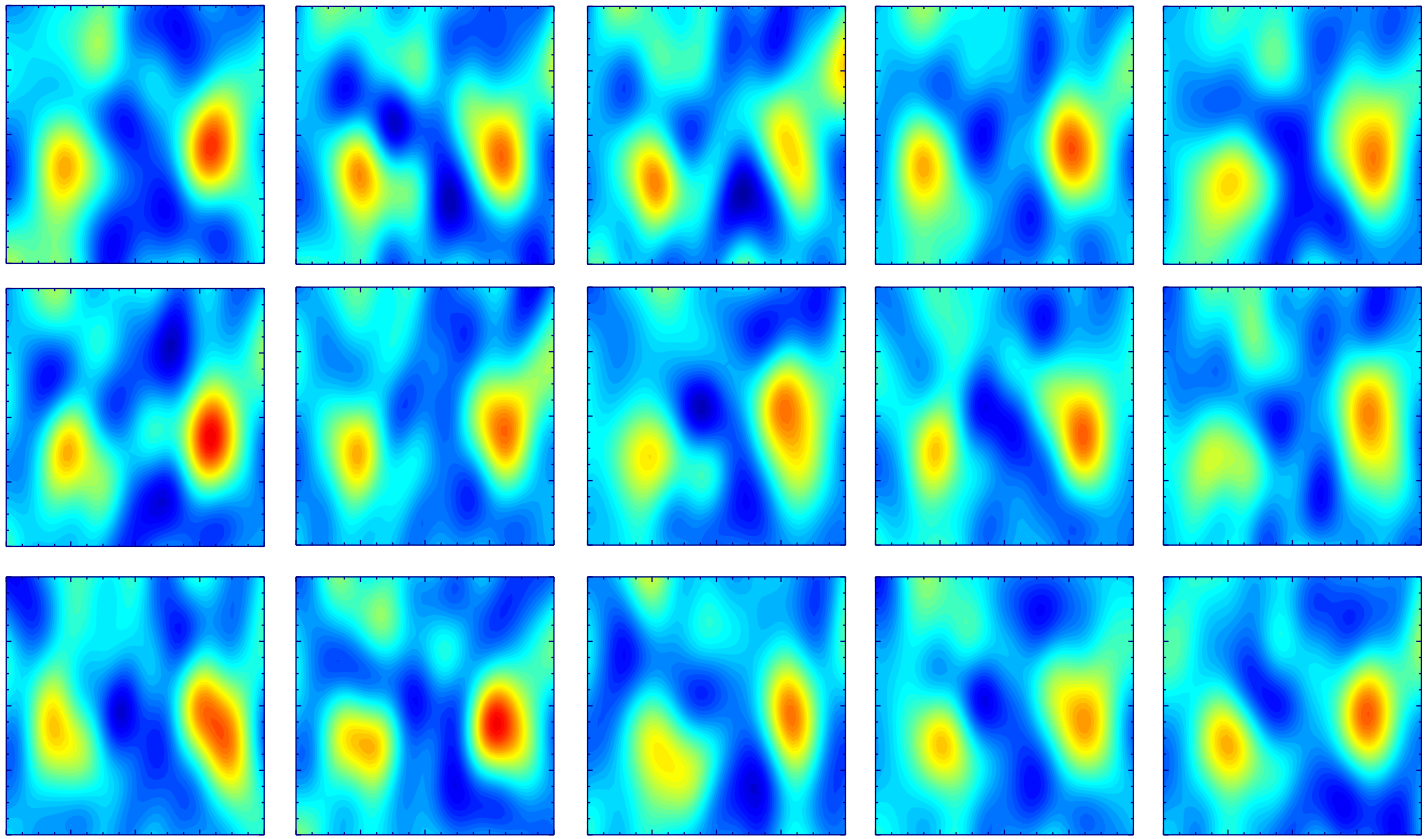

Figure 6.18: A sequence of fifteen 5 μs exposures, each separated by a sweep time of 160 μs. There is some significant dynamics in the mode conversion windows on a timescale smaller than the 0.16 ms frequency sweep.

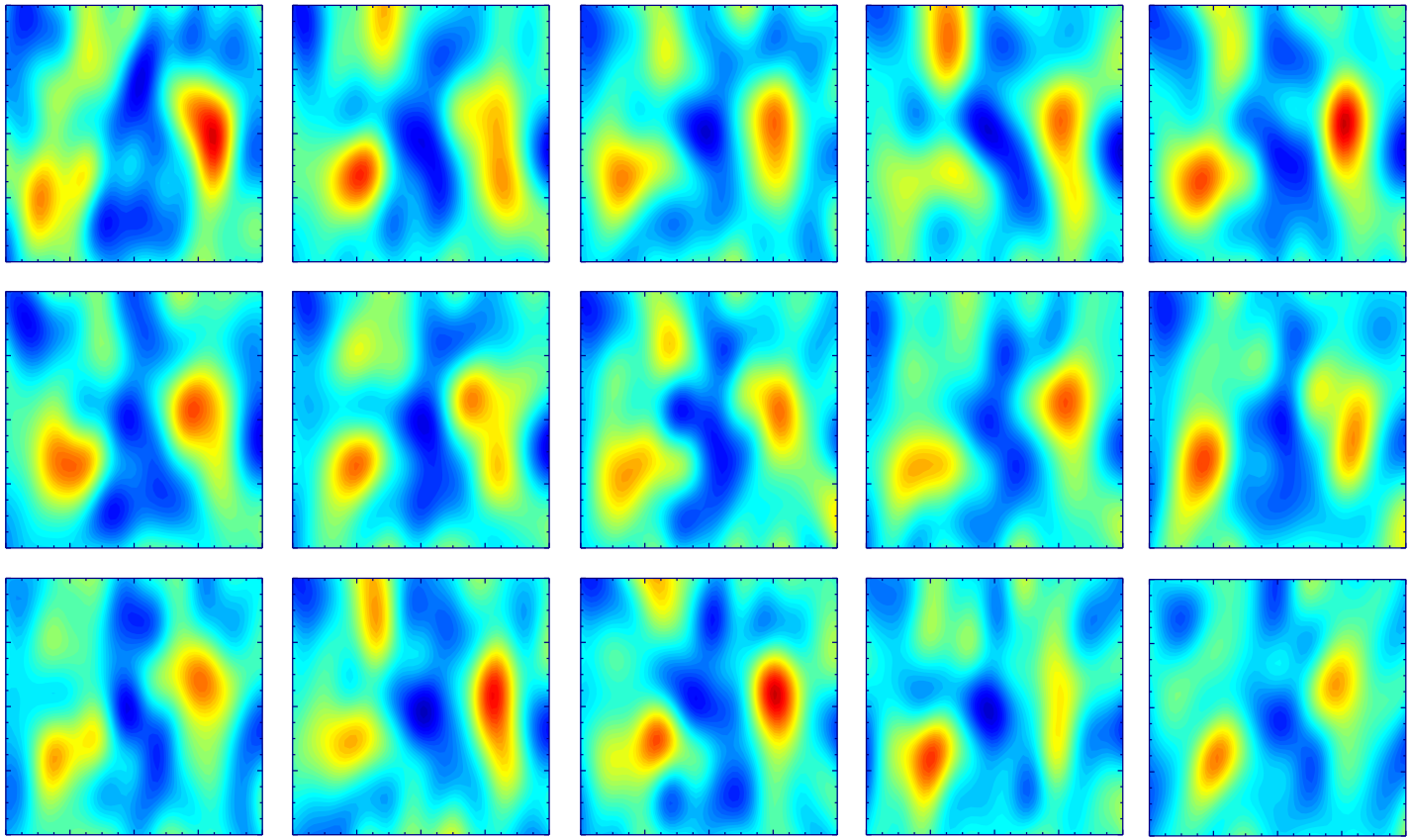

Figure 6.19: The same as Figure 6.18, but for 17 GHz. We see markedly more dynamic behaviour with the upper window often splitting and rejoining.

6.4 Discussion of sources of error

There are many potential sources for error in the measurements made by SAMI. Of these errors, every effort has been made to correct for them or to design the receiver in such a way as to minimise the presence of the error in the image reconstructions. The possible sources of error are as follows and I shall consider each one of these in turn below:

1. Imperfect sideband separation.
2. The presence of spurious sidelobes in the image resulting from the fact that a limited number of spatial frequencies have been measured.
3. The phase stability of the diagnostic over time
4. Correlated noise due to the amplifier noise being emitted by each antenna
5. Noise in the cross correlation of the antenna signals due to receiver noise generated by the local oscillator and amplifier components.
6. The mutual coupling, or cross-talk of each antenna element with every other.
7. Unknown small movements in the flexible antennas
8. Secondary reflection of plasma emission.
9. The effect of the far-field approximation.

1. The sidebands have a detrimental effect on the ability of SAMI to measure the antenna or cross-correlation phase. This is shown mathematically in section 4.1.1 and experimentally demonstrated in section 5, where the effect of the sidebands was to randomly alter the phase between real and imaginary components. It is possible to separate the sidebands by using a Hilbert transform and an addition as described in section 4.1.1. Further, this process was enhanced by a process where the real and imaginary amplitude and phase errors were measured and subsequently these components were reconstructed. Further the presence of aliasing was removed by the appropriate choice of low pass filter and a level of at least 20dB suppression was achieved in all channels at all frequencies. This makes

the influence of the incorrect sideband less than a percent of the final signal.

2. This is perhaps the most significant source of error in the image reconstructions, as it pertains to a genuine lack of information. There are 2500 pixels in each image reconstruction presented in this thesis, and only 56 measured constraints on these pixels. This lack of information, however, is known and enters the image in a known way. The influence of the unmeasured spatial frequencies may be neatly described in the form of a convolution of the real image with the point spread function given in angular coordinates in Figure 6.20. This convolution smears the image by the main beam and introduces spurious sidelobe patterns. The smearing effect is worse at lower frequencies, but reduces as the frequency, and thus angular resolution, increases. However as the frequency increases the effect of the sidelobes becomes more severe as they become more numerous and closer together. This is a kind of uncertainty principle between beam quality and angular resolution as pointed out by J. Bará *et al* [51]. The effect of this point spread function may be minimised in two ways. The first was the subject of section 4.3 and that is to optimise the placement of antennas such that the sidelobe oscillations are minimal for the given beam size and antenna number. The second is to use some deconvolution technique to attempt to remove the effect of the known point spread function. There are many deconvolution techniques available, of which the most promising are CLEAN and the Maximum Entropy Method (MEM) [78, 79, 80, 81]. These techniques are very successful, finding ways to self consistently adjust the unmeasured spatial frequencies such that their influence in the final image is minimal. It is beyond the scope of this thesis to implement these schemes however. Another rather more obvious way to reduce this effect is the addition of more antennas. SAMI has the as yet unimplemented, capacity to switch between groups of antennas to boost its Fourier space coverage. These switches double the number of baselines measured, but we must assume that either the image doesn't change faster than the switch, or that the long timescale observed behaviour isn't sensitive to the sampling point. Alternatively adding more antenna channels avoids this complication and produces many more baselines as the number of pairs goes as the square of the number of antennas.

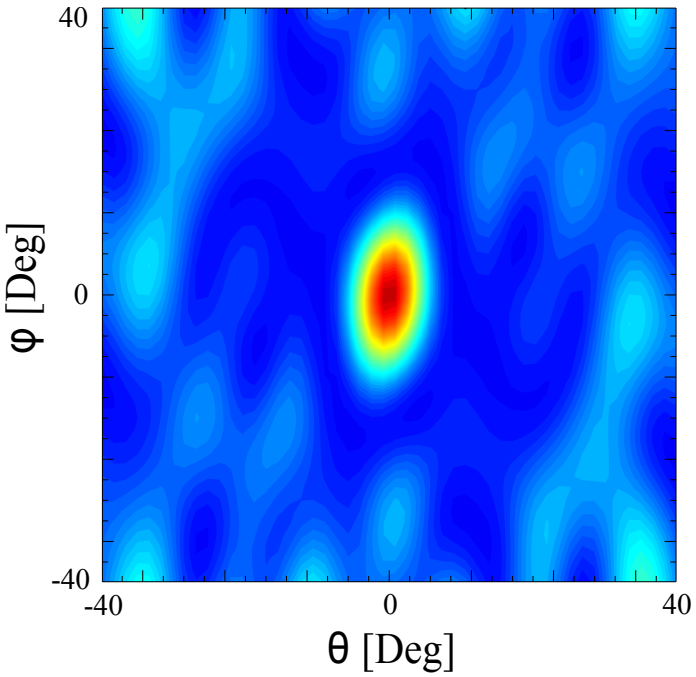

Figure 6.20: The point spread function of the optimised array used in the SAMI experiments. This plot is in angular coordinates for easy comparison with the presented images, however, the convolution is in the linear coordinates η and ξ in expression 3.9.

3. Because of the importance of the accurate measurement of phase to the imaging technique, the phase stability was a primary concern in the design of the hardware and steps were taken to minimise any phase drifts with temperature, cable position, or over time. The diagnostic was built with mostly rigid coaxial or phase stable cables, in particular those cables which carry the signal from the antenna to the LNA have a phase change of less than 0.036° in the expected temperature range and only 12° at the highest frequency when wrapped around a 10 cm diameter cylinder. The consistency of the phase was measured by calibrating the diagnostic both before and after the experimental campaign and no difference was found within the experimental error.

4. The principle of measuring the antenna cross-correlations is very resilient to uncorrelated noise. It cannot, however, remove the effect of correlated noise. It is the case that the SAMI amplifiers emit some noise from the antennas which is consequently picked up by the neighbouring antennas. Importantly, this same noise also passes through the receiver

from this same antenna. The result is the presence of a small amount of the same noise on any two antenna channels. The cross-correlations, as highlighted in section 3.2.4, then pick out the noise components that are common to both channels and this will not be averaged out. This effect tends only to affect those channels which have the lowest signal, and will affect lower frequencies more than higher frequencies due to the reduction in the mutual coupling with frequency. The correlated noise is constant throughout a shot and thus as a countermeasure, SAMI is triggered 10 ms before the plasma so it may measure its own noise and noise correlations before the plasma signal comes. This correlated noise is then simply subtracted from the cross-correlations in analysis.

5. This is the base limitation in the correlation sensitivity and, as shown in section 3.2.3, depends on the antenna signal power, the receiver noise power, the integration time and the receiving bandwidth. During analysis this quantity is calculated for each correlation and an effort is made to ensure that the ratio of this correlation noise to the magnitude of the correlations is well above one. Typically for frequencies in the range 15 - 18 GHz, this ratio is above 15. Further work may go on to automatically exclude correlations which do not satisfy that this ratio is greater than one. This may increase the reliability of SAMI if it were to become a routine diagnostic.

6. Again as discussed in section 3.2.4 the mutual coupling of antenna elements may cause some of the received signal by one element also to be reflected and received by all other elements in the array to varying degrees. The cross talk serves to blur the image introducing spurious phases which depend on the magnitude of the normalised correlations. At first it may seem that this is a very complicated issue to resolve, but with a few minor approximations I have shown that this cross-talk effect enters the cross-correlations in a predictable way and once measured it is easily subtracted from the measurements. this was also shown by J. Dong et al [53]. However, the measurement of the cross-talk is not such a straightforward task. It requires either very accurate knowledge of the image presented to the array in order to accurately predict the correlations, or a very uniform and broad source so the normalised correlations due to the source approach zero.

We may attempt to put a limit on the level to which cross-talk affects the images, although the precise extent depends on the image itself. The measurements obtained at the University of Strathclyde, discussed in section 5.2, put the worst case of mutual coupling between antennas everywhere below -20dB. Then, if this is unchanged by the presence of the vacuum window, the cross-talk affect should only be significant if a large number of the baselines measure below 1% normalised correlation. This may sometimes be the case and should be measured in future, however it may suffice in the interim to simply neglect those correlations which are below this value and treat the measurement of the mutual coupling as a way to increase the dynamic range of SAMI.

7. Although the SAMI antennas are well protected, they are small and flexible. During the campaign it is possible that small movements of the antennas could have taken place. We know of one particular incident where a member of the MAST team was blowing helium around the antennas looking for vacuum leaks. A basic study was done, although not presented here, where the antenna position was perturbed by 1 mm in a random direction in simulation. No observable effect was seen.

8. This effect is hard to quantify. Each part of the plasma is emitting the mode converted Bernstein waves, which will be reflected by the walls of the vessel. Since the emission is thermal in nature, there will not be any coherent effects, also the radiation is likely to have undergone many reflections before it is picked up by the array, if it does not come from the observed mode conversion windows. It is then taken to be a constant background upon which the imaging may occur. Indeed the images obtained seem to suggest that the reflection level is low, as they match simulation reasonably well, but a more detailed analysis of this area may be required.

9. The effect of the far-field approximation has already been seen in section 5.3.1, where it produced a 10% error in the estimation of the angular position of a point source. This issue can be in the first order resolved by operating the diagnostic as a phased array. That is adjusting the antennas phases and add the signals such that there is constructive interference from signals in the direction that is of interest. This is a very similar procedure as the inverse Fourier transform performed in this thesis, only it allows the flexibility of fo-

cussing the array on a particular point in space. i.e. we relax the condition of plane waves at the antennas and allow for some wave-front curvature. There is still an open question as to where the best place to focus such a scheme, as the Bernstein waves originate from very different positions within the plasma. We may focus the array to the density cut-off layer, but is it correct to treat this as the origin of the emission? After all, you do not focus on the lens in an optical system. It is beyond the scope of this thesis to treat this particular problem more fully, but it is an interesting question.

Chapter 7

Conclusions

The aim of this project was two fold. First was to prove the principle of interferometric imaging on a tokamak. The second was to obtain the first images of mode converted electron Bernstein waves. Both of these objectives have been achieved.

The first objective involved the design, construction and calibration of a synthetic aperture imaging radiometer which measures the spatial coherence of the incident radiation field on an array of antenna elements, in order to reconstruct the brightness distribution as a function of angle. The image analysis was done off-line as this allowed maximum flexibility in the image reconstruction process. For this purpose we designed a full vector heterodyne receiver with a demonstrably stable phase response. The receiver has 16 frequency channels which could be switched between in any order within 10 μs. It is extremely broadband covering the range from 10 to 40 GHz and this was achieved by using coaxial technology in the RF part, avoiding the bands which are synonymous with waveguided transmission, at the expense of increased attenuation at the higher end of the frequency range. Second harmonic mixers were used to reduce the requirements for the transmission of the local oscillator power, and these mixers were operated in an optimal regime to maximise the sensitivity of the receiver.

Antipodal Vivaldi antennas were used because of their small size and their very broadband characteristics. The wide gain patterns were a great advantage for the imaging array, given

the quasi near-field nature of the emission and the relatively wide structures expected to be reconstructed. The antennas were tested at the University of Strathclyde using their scalar and vector network analysers. The beam patterns were found to be twice as wide in the H plane as the E plane. The antenna reflection coefficient was satisfactory, measured to be below -10 dB for all of SAMI's frequency channels. The cross talk was measured to be below -20 dB for all frequency channels, which for small printed circuit board antennas was also satisfactory.

It was necessary to arrange the antennas in a configuration which minimised the sidelobe oscillations in the reconstructed image. This configuration was obtained via a numerical optimisation, using a simulated annealing algorithm which optimised a modified beam efficiency function. This optimisation was also carried out for two groups of eight antennas simultaneously to accommodate SAMI's ability to switch between groups of antennas to enhance its coverage of Fourier space.

A three antenna pilot system was installed on the MAST vessel in order to inform digitisation requirements and to learn as much about the details of how the hardware performs on the machine as possible. We learned that in order to cover the full signal range with sufficient bit depth we required 14 bits of data at 250 MHz. We also learned how imperfect sideband separation could affect the phase measurements of the cross correlations. The decision was taken to design a digitiser system ourselves so we could tightly control the synchronicity of the channels and ensure that they met our exact requirements, whilst also significantly reducing the cost of digitisation.

The digitisation of the received signals was achieved by an FPGA controlled digitiser. The firmware for controlling the digitiser was developed by the SAMI team. The system had to acquire data continuously for 0.5 seconds from 16 analogue channels at 14 bits at 250 MHz and record data throughputs were achieved of 8 GBs^{-1}. This FPGA solution was also responsible for the frequency switching of the local oscillator and generating the IF frequency for an active scattering component to SAMI which is not described in this thesis.

The full eight antenna SAMI system was calibrated in two ways. Two off-vessel calibrations and an on-vessel calibration. The first off-vessel calibration revealed the array's ability to track a point source although this was explored more fully in the second off-vessel calibration. It also set the phase, amplitude and sideband suppression calibration values for the experimental campaign. The second off-vessel calibration showed the calibration had not drifted during the course of the experiment and demonstrated the array's ability to track a point source through a wide range of angles, such that the limit was the near-field approximation, introducing a 10% systematic error in the estimation of the angular position of the source. The on-vessel calibration served to demonstrate that the phase calibration was transferable from the off-vessel position to the on-vessel operating position. We were able to reconstruct the point source pointing directly through the vessel, but some of the on-vessel calibration shots were left uncertain due to significant in-vessel reflections.

The second objective was to obtain the first ever images of B-sX-O mode conversion. These images have now been accumulated over one experimental campaign and constitute nearly 10 TB of data. The analysed images from shot # 27004 come from a quiet H-mode period at 360 ms. These images were compared with a 1D full-wave coupling, Bernstein wave ray-tracing code called AMR. The experimental images are in qualitative agreement with the AMR predictions. The lower MC window becomes less efficient and the upper becomes more efficient as the frequency increases. However, the upper window appears to be relatively more efficient than predicted as it is often well formed and not dominated by the lower window. At first, there was a concern that the upper window was occurring at a lower vertical angle than predicted and displaying odd splitting behaviour which is not explained by mode coupling alone. This was explained by the radiative temperature of the Bernstein waves being strongly peaked on the midplane due to their refraction in the magnetic field. Both the reduction in vertical angle and the splitting are predicted by AMR.

A high degree of fluctuations in the mode conversion windows was observed, but the background cause is still to be determined. The fluctuations operate on a timescale that

appears to be faster than the total switching period of the SAMI receiver (160 μs) and manifest in changes in window brightness and angular position. Further work should focus on a single frequency in order to push the temporal resolution as high as possible to further investigate this effect.

In all the project has met its initial objectives. We have shown new and interesting behaviour in the mode conversion process which has been unobserved until now. We have opened the door for many interesting effects to be studied and a chance for the first time to observe two and three dimensional effects of mode conversion. We may now also closer study the relationship between the observed mode conversion brightness and the plasma pedestal parameters, using this knowledge to shed light on the important physical processes which are behind the ELM instability.

Definitions

ECE ..... Electron Cyclotron Emission
EBE ..... Electron Bernstein wave Emission
ECRH ..... Electron Cyclotron Resonance Heating
ECCD ..... Electron Cyclotron Current Drive
X mode ..... refers to the cold plasma eXtraordinary mode
O mode ..... refers to the cold plasma Ordinary mode
EBW ..... Electron Bernstein wave
MSE ..... Motional Stark Effect
ELM ..... Edge Localised Mode
FPGA ..... Field Programmable Gate Array
WKB ..... Wentzel, Kramers, Brillouin approximation
MBE ..... Main Beam Efficiency
SA ..... Simulated Annealing
SAMI ..... Synthetic Aperture Microwave Imaging
MC ..... Mode Conversion
$\boldsymbol{B}$ ..... magnetic field vector
$\boldsymbol{E}$ ..... electric field vector
ω_{p} ..... plasma frequency
ω_{c} ..... cyclotron frequency
ω_{UH} ..... upper hybrid frequency
ω ..... radiation frequency
X ..... ratio of plasma frequency to radiation frequency

Y ..... ratio of cyclotron frequency to radiation frequency

j ..... current density

e ..... electron charge

n_e ..... electron density

m_e ..... electron mass

$\boldsymbol{\sigma}$ ..... conductivity tensor

$\boldsymbol{\epsilon}$ ..... dielectric tensor

$\boldsymbol{k}$ ..... wave vector

$\boldsymbol{N}$ ..... refractive index

ρ ..... Larmor radius

v_{th} ..... electron thermal velocity

$\mathscr{T}$ ..... transmissivity

L_n ..... density scale length

L_θ ..... shear scale length

r ..... ratio of density to shear scale lengths

n_a ..... number of antennas

ϕ ..... generic phase

g ..... antenna voltage pattern

G ..... antenna gain pattern

$\boldsymbol{a}$ ..... antenna vector position

$\boldsymbol{b}$ ..... antenna pair baseline vector

I ..... radiation intensity distribution

$\Gamma_{i,j}$ ..... cross-correlation

Γ ..... autocorrelation

$\hat{\boldsymbol{\alpha}}$ ..... unit array directional vector

η, ξ ..... real space coordinates for image reconstruction

u, v ..... Fourier space coordinates of antenna pairs

Q, Q_v ..... linear component of stokes vector and visibility

U, U_v ..... linear component of stokes vector and visibility

V, V_v ..... circular component of stokes vector and visibility

ψ, χ ..... polarisation ellipse angles

σ ..... standard correlation error

B ..... bandwidth

T ..... integration time period

AF_{eq} ..... array factor

ϵ ..... beam efficiency

P ..... probability

$\boldsymbol{H}$ ..... entropy

$\boldsymbol{\alpha}, \boldsymbol{\beta}$ ..... Lagrange multipliers

Bibliography

[1] V Barabash et al. Armour materials for the iter plasma facing components. *Physica Scripta*, T81, 1999.

[2] J Paméla et al. An ITER like wall for JET. *Journal of nuclear materials*, 363.

[3] A Y Ying et al. Exploratory studies of flowing liquid metal divertor options for fusion-relevant magnetic fields in the MTOR facility. *Fusion engineering and design*, 72, 2004.

[4] P M Valanju, M Kotschenreuther, and S M Mahajan. Super X divertors for solving heat and neutron flux problems of fusion devices. *Fusion engineering and design*, 85, 2010.

[5] A Y Ying et al. Taming the plasmamaterial interface with the 'snowflake' divertor in NSTX. *Nuclear Fusion*, 51, 2011.

[6] W Suttrop et al. In-vessel saddle coils for MHD control in ASDEX upgrade. *Fusion engineering and design*, 84, 2009.

[7] P T Lang et al. Frequency control of type-i elms by magnetic triggering in asdex upgrade. *plasma physics and controlled fusion*, 46, 2004.

[8] J Wesson and A Sykes. Tokamak beta limit. *Nuclear Fusion*, 25(1), 1985.

[9] F Wagner et al. Regime of improved confinement and high beta in neutral-beam-heated divertor discharges of the ASDEX tokamak. *Physical Review Letters*, 49(19), 1982.

[10] A Herrmann. Overview on stationary and transient divertor heat loads. *Plasma physics and controlled fusion*, 44, 2002.

[11] A Herrmann et al. Stationary and transient divertor heat flux profiles and extrapolation to ITER. *Journal of nuclear materials*, 313, 2003.

[12] D N Hill. A review of elms in divertor tokamaks. *Journal of Nuclear Materials*, 241, 1997.

[13] D M Thomas and A W Leonard et al. Measurement of pressure-gradient-driven currents in tokamak edge plasmas. *Physical Review Letters*, 93(6), 2004.

[14] V F Shevchenko et al. Two dimensional studies of electron Bernstein wave emission in MAST. *Fusion Science and technology*, 59(4), 2011.

[15] V Shevchenko. ECE measurements via B-X-O mode conversion: A proposal to diagnose the q profile in spherical tokamaks. *Plasma Physics Reports*, 26(12), 2000.

[16] T H Stix. *Waves in Plasmas*. AIP Press, 1992.

[17] F Chen. *Introduction to Plasma Physics and Controlled Fusion*. World Scientific Publishing Co, 1987.

[18] P C Clemmow and J P Dougherty. *Electrodynamics of Particles and Plasmas*. Adison-Wesley, 1969.

[19] V L Ginzburg. *The propagation of electromagnetic waves in plasmas*. Pergamon press, 1970.

[20] F Volpe. *Electron Bernstein emission diagnostic of electron temperature profile at W7-As Stellarator*. PhD thesis, Max-Planck-Institut fuer Plasmaphysik, 2003.

[21] A D Pilya and A Yu Popov. On application of the reciprocity theorem to calculation of a microwave radiation signal in inhomogeneous hot magnetised plasma. *Plasma Phys. Control. Fusion*, 44, 2002.

[22] A Kohn et al. Full wave calculation of the O-X-B mode conversion of gaussian beams in a cylindrical plasma. *Plasma Phys. Control. Fusion*, 50, 2008.

[23] A Kohn, E Holzhauer, and U Stroth. Visualisation of the O-X-B mode conversion process with a full wave code. *IEEE transactions on plasma science*, 36(4), 2008.

[24] J Prienhaelter and V Kopecký. Penatration of high-frequency waves into a weakly inhomogeneous magnetized plasma at oblique incidence and their transformation to Bernstein modes. *J. Plasma Physics*, 10(1), 1973.

[25] E Mjølhus. Coupling to Z mode near critical angle. *J. Plasma Physics*, 31(1), 1984.

[26] R Weitzner and D B Batchelor. Conversion between cold plasma modes in an inhomogeneous plasma. *Phys. Fluids*, 22(7), 1979.

[27] F R Hansen et al. Full-wave calculations of the O-X mode conversion process. *J. Plasma Physics*, 39(2), 1988.

[28] R A Cairns and C N Lashmore-Davies. The prospect for electron Bernstein wave heating of spherical tokamaks. *Physics of Plasmas*, 7(10), 2000.

[29] E D Gospodchikov, A G Shalashov, and E V Suvorov. On the influence of 2D inhomogeneity on electromagnetic mode conversion near the cut-off surfaces in magnetised plasma. *Plasma Phys. Control. Fusion*, 48, 2006.

[30] A Yu Popov. On O-X mode conversion in spherical tokamaks. *Plasma Phys. Control. Fusion*, 49, 2007.

[31] M A Irzak and A Yu Popov. 2D modelling of the O-X conversion in toroidal plasmas. *Plasma Phys. Control. Fusion*, 50, 2008.

[32] E D Gospodchikov and A G Shalashov. On perfect O-X mode conversion near the cut-off surfaces in magnetised plasmas. *Plasma Phys. Control. Fusion*, 50, 2008.

[33] A G Shalashov and E D Gospodchikov. On O-X mode conversion near the cut-off surfaces in 3D sheared magnetic field. *Plasma Phys. Control. Fusion*, 52, 2010.

[34] A Popov. On O-X mode conversion in a 3D inhomogeneous plasma. *Plasma Phys. Control. Fusion*, 53, 2011.

[35] H P Laqua. Electron bernstien wave heating and diagnostic. *Plasma Phys. Control. Fusion*, 49(4), 2007.

[36] S Pesiˇc. Propagation and damping of linearly converted electron cyclotron quasi longitudinal waves. *Physica*, 125, 1984.

[37] B H Deng et al. Electron cyclotron emission diagnostic on TEXTOR. *Rev. Sci. Instrum.*, 72(1), 2001.

[38] H Park et al. Recent advancements in microwave imaging plasma diagnostics. *Rev. Sci. Instrum.*, 74(10), 2003.

[39] L. Azar et al. Beam focusing behavior of linear phased arrays. *NDT and E International*, 33(3), 2000.

[40] H M Aumann and F G Willwerth. Synthesis of phased array far-field patterns by focusing in the near-field. *1989 IEEE national radar conference*, 1989.

[41] J D Monnier. Optical interferometry in astronomy. *Rep. Prog. Phys*, 66, 2003.

[42] R J Mailloux. *phased array antennas*. Wiley, 2005.

[43] R C Hansen. *phased array antenna handbook*. Artech House, 2009.

[44] D L Liu and R G Waag. About the application of the van Cittert - Zernike theorem in ultrasonic imaging. *Transactions on ultrasonics, ferroelectrics and frequency control*, 42(4), 1995.

[45] J W Goodman. *statistical optics*. wiley - interscience, 1985.

[46] P H van Cittert. Die wahrscheinliche schwingungsverteilung in einer von einer lichtquelle direkt oder mittels einer linse beleuchteten ebene. *Physica*, 1(1).

[47] F. Zernike. The concept of degree of coherence and its application to optical problems. *Physica*, 5(8), 1938.

[48] C W McCutchen. Genralized source and the van Cittert - Zernike theorem: A study of the spatial coherence required for interferometry. *Journal of the optical society of America*, 56(6), 1966.

[49] A R Thompson, J M Moran, and G W Swenson Jr. *Interferometry and synthesis in radio astronomy*. Wiley - VCH, 2004.

[50] A. Camps et al. Radiometric sensitivity computation in aperture synthesis interferometric radiometry. *IEEE Transactions on geoscience and remote sensing*, 36(2), 1998.

[51] J. Bará et al. The correlation of visibility noise and its impact on the radiometric resolution of an aperture synthesis radiometer. *IEEE Transactions on geoscience and remote sensing*, 38(5), 2000.

[52] C. S. Ruf. Error analysis of image reconstruction by a synthetic aperture interferometric radiometer. *radio science*, 26(6), 1991.

[53] J. Dong et al. An external calibration method for compensating for the mutual coupling effect in large interferometric aperture synthesis radiometers. *International journal of antennas and propagation*, 2011, 2011.

[54] P. Darwood et al. Mutual coupling compensation in small planar array antennas. *IEE Proceedings - microwaves antennas and propagation*, 145(1), 1998.

[55] A. B. Tanner and C. T. Swift. Calibration of a synthetic aperture radiometer. *Radio science*, 26(6), 1993.

[56] A Camps et al. Impact of antenna errors on the radiometric accuracy of large aperture synthesis radiometers. *Radio science*, 32(2), 1997.

[57] A Camps et al. Mutual coupling effect on antenna radiation pattern: an experimental study applied to interferometric radiometers. *Radio science*, 33(6), 1998.

[58] N Wiener. Generalized harmonic analysis. *Act. Math*, 55(117), 1930.

[59] A Khinchine. Korrelationstheorie der stationaren stochastischen prozesse. *Math. Ann*, 109(604), 1934.

[60] I Corbella et al. The visibility function in interferometric aperture synthesis radiometry. *IEEE Transactions on geoscience and remote sensing*, 42(8), 2004.

[61] R Butora et al. Fringe-washing function calibration in aperture synthesis microwave radiometry. *radio science*, 38(2), 2003.

[62] N J Conway et al. The MAST motional stark effect diagnostic. *Rev. Sci. Instrum.*, 81, 2010.

[63] B Huang et al. standardisation of FPGA systems incorporating embedded linux: The MAST EBW digitiser example. *IAEA fus. eng. design (submitted)*, 2011.

[64] B Huang et al. Bottling a star using ARM's AXI bus in an FPGA. *Xcell journal*, 76, 2011.

[65] S G Kim. *wideband two dimensional and multiple beam phased arrays and microwave applications using piezoelectric transducers*. PhD thesis, Texas A and M University, 2005.

[66] X Qing, Z N Chen, and M W Chia. Parametric study of ultra wideband dual elliptically tapered antipodal slot antennas. *International journal of antennas and propagation*, 2008.

[67] A Camps *et al*. Radiometric sensitivity computation in aperture synthesis interferometric radiometry. *IEEE transactions on geoscience and remote sensing*, 36(2), 1998.

[68] T J Cornwell. A novel principle for optimisation of instantaneous fourier plane coverage of correlation arrays. *IEEE transactions on antennas and propagation*, 36(8), 1988.

[69] A Janos et al. Bursts of electron cyclotron emission during ELMs and high beta disruptions in TFTR. *Plasma Phys. Control. Fusion*, 38, 1996.

[70] A Janos et al. Bursts of electron cyclotron emission during disruptions of high beta discharges in the Tokamak Fusion Test Reactor tokamak. *Rev. Sci. Instrum.*, 68(1), 1997.

[71] Ch Fuchs and M E Austin. Measurements of edge-localized-mode induced electron cyclotron emission bursts in DIII-D. *Phys. Plasmas*, 8(5), 2001.

[72] R J Groebner et al. Limits to the h-mode pedestal pressure gradient in DIII-D. *Nuclear Fusion*, 50, 2010.

[73] D Dickenson et al. Towards the construction of a model to describe the inter-elm evolution of the pedestal on MAST. *Plasma physics and controlled fusion*, 53, 2011.

[74] J Urban and J Prienhaelter. Adaptive finite elements for a set of second-order odes. *J. Plasma Physics*, 72(6), 2006.

[75] Ryoukai et al. The correlation analysis between electron density fluctuation and RF stray power in the CPD electron cyclotron plasma. *J. Plasma Fusion Res.*, 9, 2010.

[76] S Diem at al. Electron Bernstein wave emission based diagnostic on National Spherical Torus Experiment (invited). *Rev. Sci. Instrum..*, 79, 2008.

[77] H P Laqua et al. Resonant and nonresonant electron cyclotron heating at densities above the plasma cutoff by O-X-B mode converion at the W7- As stellarator. *Physical review letters*, 78(18), 1997.

[78] R Narayan and R Nityanada. Maximum entropy image restoration in astronomy. *ann. rev. Atsron. Astrophys.*, 24, 1986.

[79] J A Hogbom. Aperture synthesis with a non-regular distribution of interferometric baselines. *Astron. Astrophys. Supp.*, 15, 1974.

[80] T J Cornwell and K F Evans. A simple maximum entropy deconvolution algorithm. *Astron. Astrophys.*, 143, 1985.

[81] J. Skilling and R. K. Bryan. Maximum entropy image reconstruction: a general algorithm. *Mon. not. R. astr. Soc.*, 211, 1984.